Cellular Evolution in PEI:
Mapping Bubble Dynamics through Solid-State CO_2 Foaming Processes

Jichen Yao

A thesis
submitted in partial fulfillment of the
requirements for the degree of

Master of Science

University of Washington
2025

Reading Committee:

Marco Salviato
Charles Dorn

Program Authorized to Offer Degree:
Aeronautics and Astronautics

University of Washington

Abstract

Cellular Evolution in PEI:

Mapping Bubble Dynamics through Solid-State
CO_2 Foaming Processes

Jichen Yao

Chair of the Supervisory Committee:

Marco Salviato
Department of Aeronautics and Astronautics

Future applications of polyetherimide (PEI) extend beyond structural panels and insulation to include vibration-damping layers, impact-resistant aerospace skins, thermal-acoustic insulation, and multifunctional components in satellites and aircraft cabins. By using dynamic mechanical analysis (DMA), a constitutive model for bubble growth under CO_2 saturation is developed, capturing glass transition effects and growth of nanofoam cells. Key properties such as cell growth rate, CO_2 concentration, porosity, and stress are extracted, supporting simulation-driven design of next-generation aerospace structures with enhanced durability, thermal stability, and energy absorption.

Cellular Evolution in PEI: Mapping Bubble Dynamics through Solid-State CO_2 Foaming Processes.

Jichen Yao (Sam)

I. Introduction

A. Introduction to Polymer

1. Polymer in Nature

Polymer refers to a large molecule composed of repeating structural units linked by covalent bonds, known as monomers. While polymers seem be to produced by physical or chemical method, there is a wide range of polymer existing in the nature for billions of years. Polymer is considered as a key player in creating the fundamental of structures and functions of most organisms.

Cellulose is considered as one of the most prevalent natural polymer materials, making up to 33% of plant matter, 50% of wood, and 90% of cotton. [1] It is the most inexhaustible natural polymer, which is biodegradable, sustainable, and eco-friendly. Cellulose serves as the critical component for plants' cell walls which provides structural support to leaves and trunks. Another form of cellulose exists as starch which can store energy and can been seen abundant in corns, potatoes or rice. In animals, proteins are natural polymer consists of long chain of amino acids linked by peptide bonds. [2] It forms the majority of muscle structures, enzymes, hemoglobin which represents a large proportion of dry mass in animals. Another major presence of polymer in nature lies on DNA and RNA. They are natural polymers which can be seen from their repeating nucleotide units and covalent backbone. It is one of the most representing polymer conformation in biology, which carries information storage with biological complexity. [2]

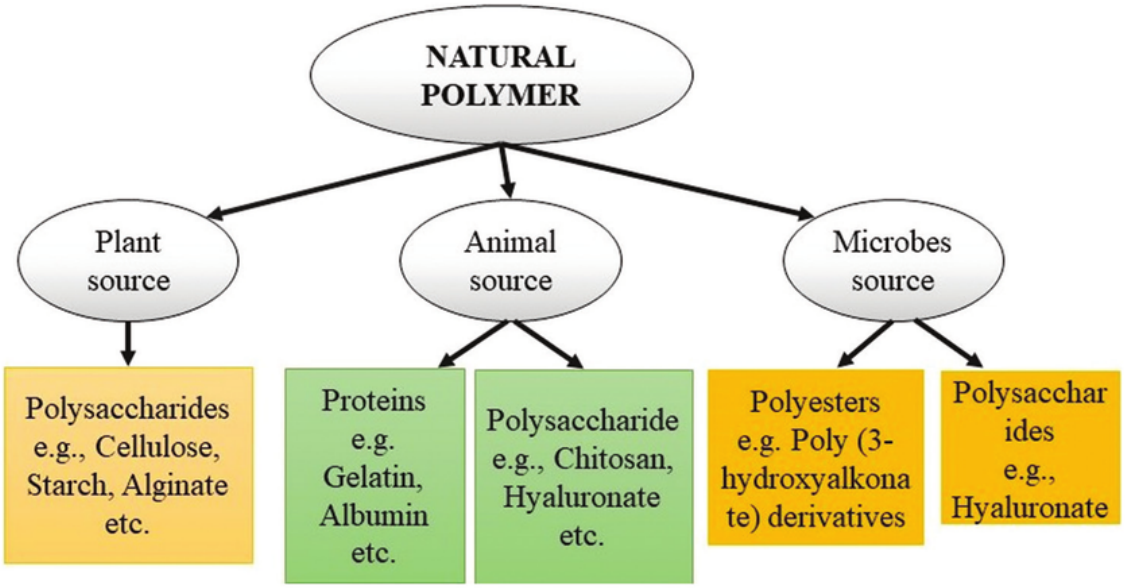

Fig. 1 Types of Natural Polymer [3]

2. History of Polymer Application

It has been seen widely in the nature ranging from cellulose, proteins to silk and wool. Human have recognized its lightweight and versatility since 1600 BC and has applied polymer in various aspects of life. Ranging from silk and

cotton to recent application in packaging and spacecraft structures, polymer has been playing a crucial role in modern life and human history. [4]

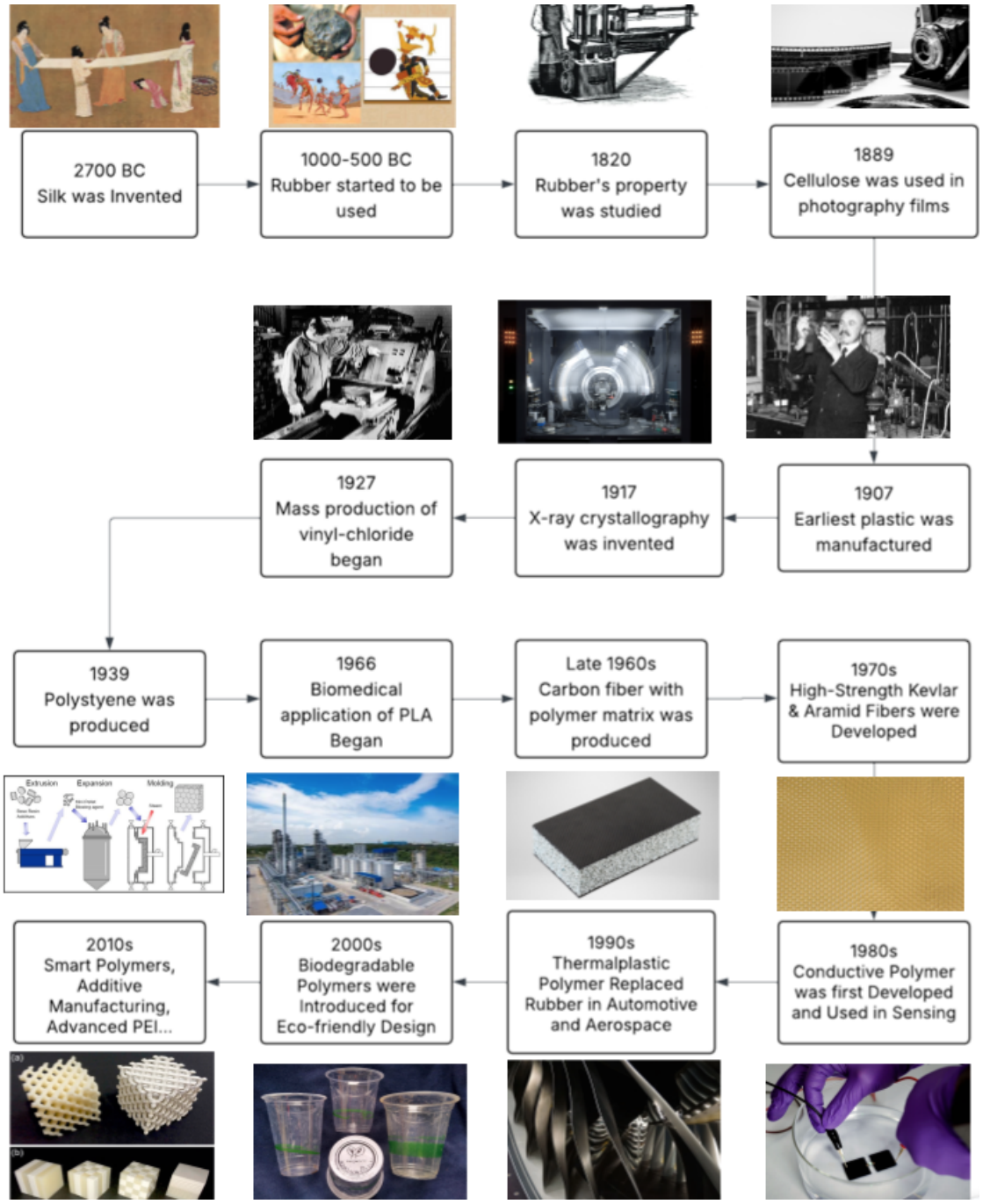

Fig. 2 History of Application of polymers [5] [4]

B. Introduction of Polymer Nanofoam

Foam refers to material formed by trapping gas bubbles in a matrix made of solid or liquid. This combination provides material with low density and high surface area while having a cellular structures. It has good surface area structures provides considerably good insulation properties. It has witnessed considerable presentation in both the

nature and industry.

1. Foam in Nature

Natural foams can be found in various biological systems and have inspired the development of sustainable, bio-based synthetic foams. For instance, sea foam, which is created by the agitation of seawater when organic matter is agitated by winds and waves. It contains persistent bubbles and can be seen commonly along coastlins. It normally indicates a high concentration of organic matter and provides essential nutritious support to ocean food web. [6] In the animal world, some frogs and fishes produce foam for the protection of their eggs. Thanks to its bubble structures, foams can provide a controlled environment free fro desiccation and temperature fluctuations to embryos. [7]. Such stability and compatibility have been studied and applied in the modern delivery capsules. Another example lies in growing fungal mycelium on organic substrates. As the mycelium grows, it releases substrate to form a foam-like structure. When desired shape is constructed, the material is dried preventing further growth, making it possible to produce packaging which can be easily broken down by nature.

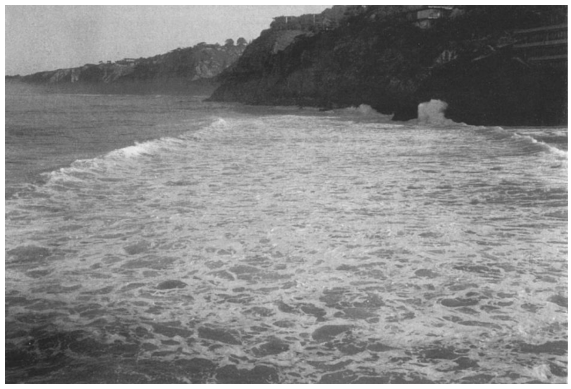

(a) Sea Foam on Coastline

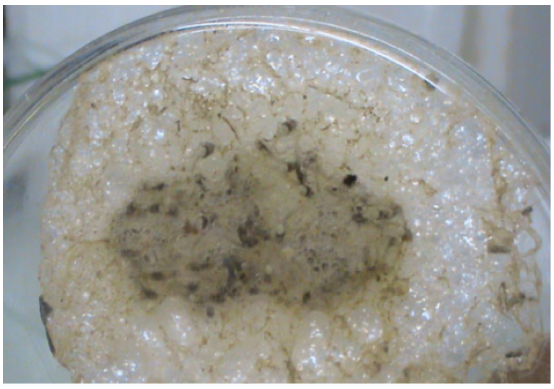

(b) Protection Foam Created by Frogs

(c) Mycelium Foams

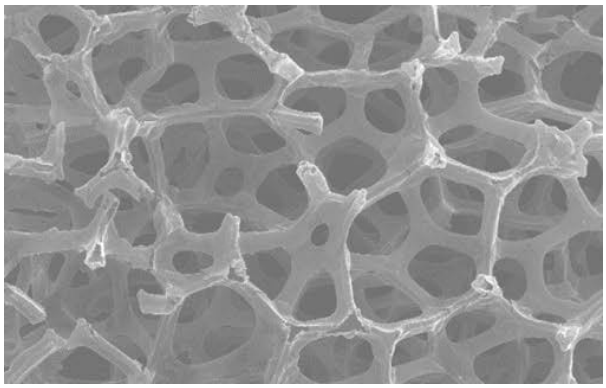

(d) SEM of Natural Foam from Organic Waste

Fig. 3 Natural Presense of Foams [8] [9] [10]

Structural foams has been considered as an important part of modern engineering. They are described as rigid plastic materials with expanded cores, offering strength and toughness for various applications. [11] Commonly made from thermoplastic, structural foam has seen a wide applications in automotive parts, aircraft coating and piping, electronic housing, etc. thanks to its cost efficiency, mechanical performance and reduced weight. Structural foams can be produced using low pressure injection molding or reaction injection molding, both of which prove its cost-effectiveness in modern engineering. [12] Thanks to modern engineering analysis techniques like X-ray and micro scoping, engineers can analyze the mechanism of structural foams more closely from marco scale to nano scale to reveal insights to the

orientation, fracture process and failure modes. [13] With these modern analysis tools and machine learning for design iteration, the use of structural foams in engineering has a promising future thanks to its flexibility in design and cost effectiveness.

2. *History of Foam Application*

Foam has played a critical role in human technology development in recent 200 years in the field of advanced structures and substances. In the 1920s, foamed rubber was produced marking the start of spongy material for cushioning. At similar time, the use of foam in firefighting was discovered and has been developed into firefighting foam and film-forming foam for extinguishing fire on aircraft carriers in 1960s. After the 1960s, memory foams start to draw the attention of people. Memory foam refers to viscoelastic polyurethane foam which has the ability to conform the body's shape and provides support. With its first application in NASA in 1969 to improve crash protection, [14] memory foam has become an important material for both safety protection gear and daily consumes. Its pressure-relieving characteristics make it ideal for pain relieving by its motion isolation properties. Today, its application ranges from mattresses, pillows to cushioning, offering enhanced comfort and support compared to cotton or other traditional cushioning materials.

(a) Foam Manufacturing in 1930s

(b)(c) Modern Application of Foams, including Firefighting

(d)(e) Foams used in Comforter

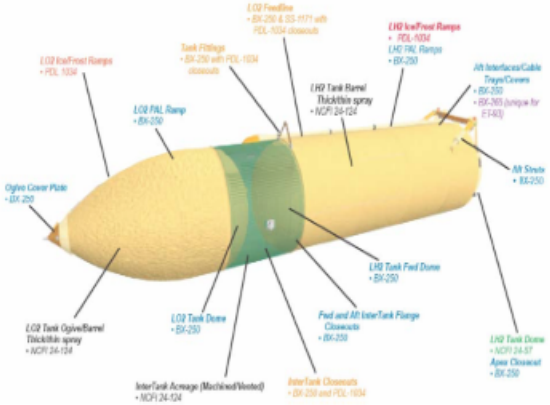

(f) Foam used in Rocket Tank

Fig. 4 Example of Application of Foams[15] [16]

3. *Nanofoam*

Nanocellular foams, or nanofoams, refer to a recent extension of microcellular technology where foamed polymers have pore sizes in the range of nanometers.[17] With ultra low density, high surface area, and tunable structures, nanofoam has seen an increase in application including engineering, medicine and energy storage. Compared to metals,

nanofoam tends to display considerably lower density while maintaining a relatively high yield strength and elastic modulus. Compared to wood, nanofoam can display greater stability and maintain similar desnity and viscoelastic performance. Below Ashby plot shows the relationship between density and mechanical performance of nanofoams compared to other materials.

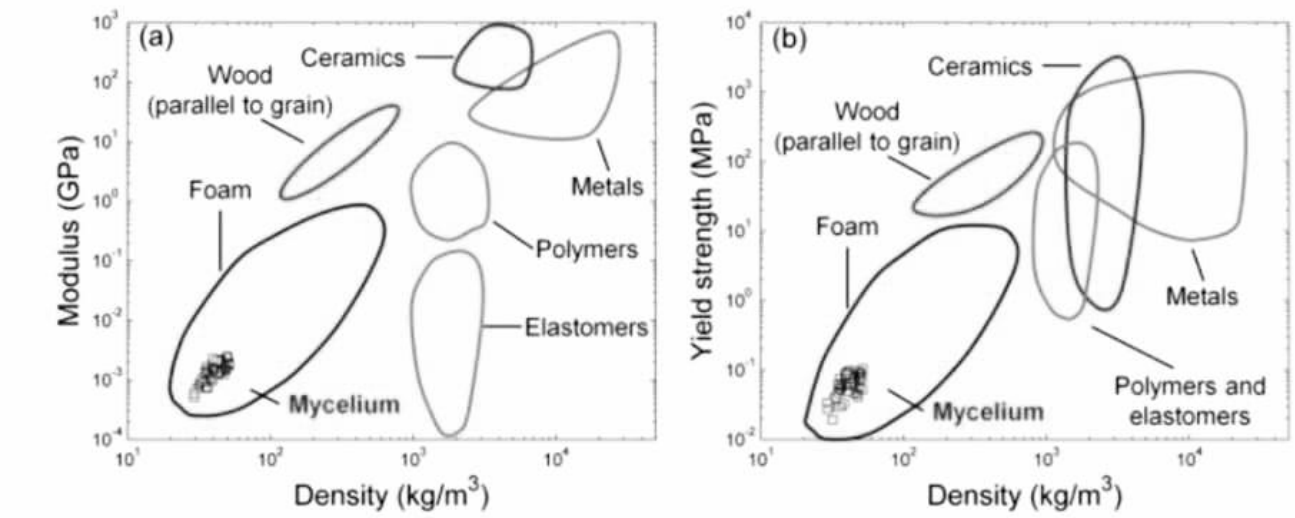

Fig. 5 Ashby Plot of Mechanical Performance among Materials

Besides engineering, nanofoam has also witnessed an increase in use in medical applications. One of the key advantages of bio-inspired nanomaterials is their potential for improved biocompatibility, multifunctionality, and environmental friendliness. In biomedical engineering, they have demonstrated significant promise in applications including targeted drug delivery, biosensing, and tissue regeneration, owing to their ability to interface effectively with biological environments. [18]. In sustainable energy, nanostructures have been utilized in the development of efficient light-harvesting systems, bio-templated electrodes, and green synthetic routes for energy storage materials. Bio-inspired nanomaterials offer a new framework in medicine, energy, and materials science by leveraging the efficiency and functionality of natural systems.

There are two widely used methods in the fabrication of polymer foams including in solid-state foaming and liquid-state foaming. In solid-state foaming, gas is blown into the polymer under high pressure. Then, the polymer is heated to allow nucleation and pore growth in a solid matrix. Liquid-state foaming, on the contrary, uses chemical blowing agents to blow gas into molten polymer. Then gas or physical agents are evaporated or expanded under heat to form bubble in liquid polymers. [19]. Solid-state foaming is chosen in this case due to some of the considerable advantages. First, it avoids the use of harmful chemical compared to liquid-state foaming which is more environmentally-friendly. It also offers more precise control over foam cell size and stability, which leads to better fit in complex polymer geometry. Additionally, solid state foaming can be done at relatively low temperatures, preserving the polymer's structure and widening the rage of types of polymers to be processed. [20]. It's applicable to thermoplastics, thermosets and even composites, which can benefit design freedom of both material and structures.

C. Introduction of PEI in Aerospace Structures

Polyetherimide (PEI) nanofoam is an amorphous thermoplastic with cell sizes below 100 nanometers. In recent years, there's an increase in the application of polymer based composite in aerospace thanks to its high mechanical strength and lightweight which brings up fuel efficiency [21]. Polymer components have the benefit of evading radar detection in military aircraft because of its high thermal resistance rating. Compared to PMMA or PEEK, PEI has relatively higher glass transition temperature which can prevent softening and deforming under thermal cycling conditions experienced in flight conditions. At the same time, PEI also displays relatively higher ultimate strength compared to PMMA and

PEEK. However, the measurement of behaviour under uniaxial tension around glass transition temperature is limited. This proposes limitations on the study of new generation composite structures in aerospace due to lack of knowledge in load transfer, structural integrity, and control quality during flight, especially during critical flight phases where thermal and mechanical loads are highest.

PEI also displays widespread application in the aircraft piping. PEI has displayed its weight-saving and high performance in the fresh water piping in an aircraft. The use of 0.6mm thick PEI pipes saves 45% to 70% of overall weight compared to titanium pipes (0.3 mm thickness) and steel pipers per meter, respectively. An A320 aircraft, for example, the overall length of freshwater piping can be as much as 100 meters. [22]The use of PEI in piping is considered as significant weight and cost reduction method.

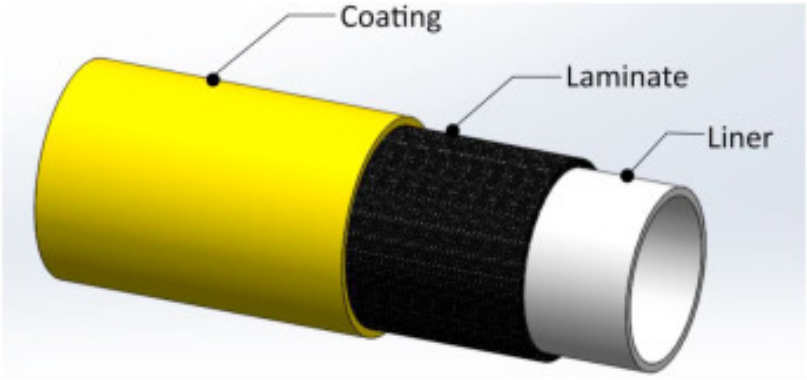

Fig. 6 Aircraft Piping Coating Made of Polymer Composite [23]

Besides direct applications, PEI has also seen wide application in additive manufacturing (AM) which can be further applied in aerospace industry. Fused Filament Fabrication (FFF) is used which involves extruding thermoplastic filament through a heated nozzle. Multi material strategy is used combining PEI ULTEM and carbon-fiber-infused ULTEM. By applying different layout strategy, mechanical performance of PEI composite can be customized including tensile strength, interlayer adhesion or thermal conductivity. Optimized multi-material layering in PEI-based composites can be tailored for specific mechanical needs in aerospace structures, such as load-bearing fuselage panels or custom aerodynamic skins. Also, the parametric study can make it easier for future application to produce PEI samples with desired properties in the controlled conditions, making it possible to tailor make material based on the design needs.[24]

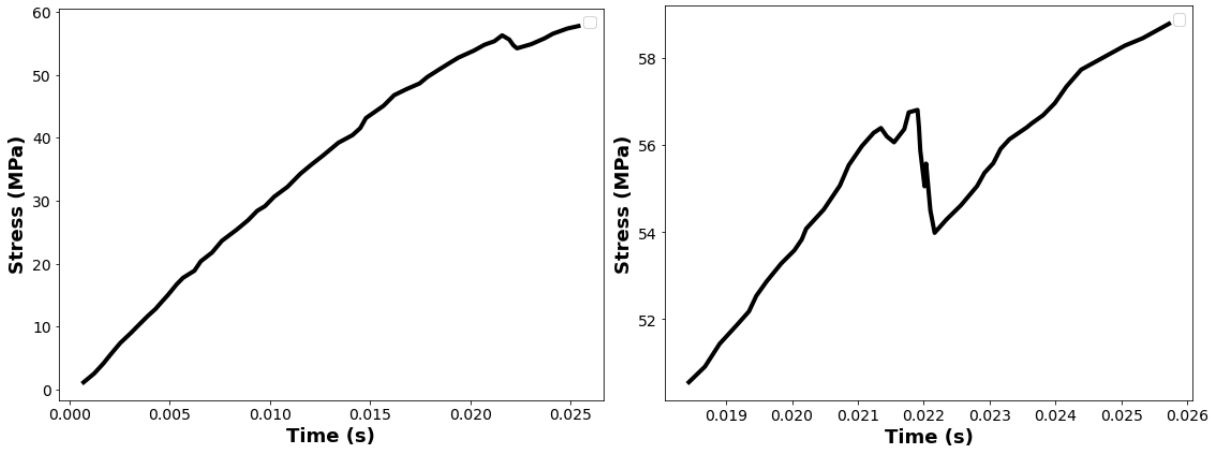

(a) Overall Tensile Response **(b) Behavior around Yielding**

Fig. 7 Tensile Testing data for PEI Composites

To manufacture high quality PEI for the applications, CO_2 saturation is considered critical to let the bubble growth, allowing foaming to begin in a temperature interval. It usually includes 3 key processing steps. (1). PEI sheets are exposed to CO_2 under a pressure between 1 and 10 MPa and temperature to allow gas to enter bubbles. The saturation takes between 1 and 24 hours. Higher pressure is needed to produce bulk PEI compared to thin films. (2). After saturation, PEI sheets are quenched to prevent premature foaming (3). Samples are heated to a temperature between 150 and 217 ° where the absorbed CO_2 can act as a blowing agent which creates foam morphology. [25] After this process, transition from microcellular to noncellular is achieved by changing the concentration of CO_2. PEI can be foamed in this way while retaining high thermal stability, allowing the creation of lightweight, thermally resistant and porous PEI sheets for various industry applications [26, 27, 28].

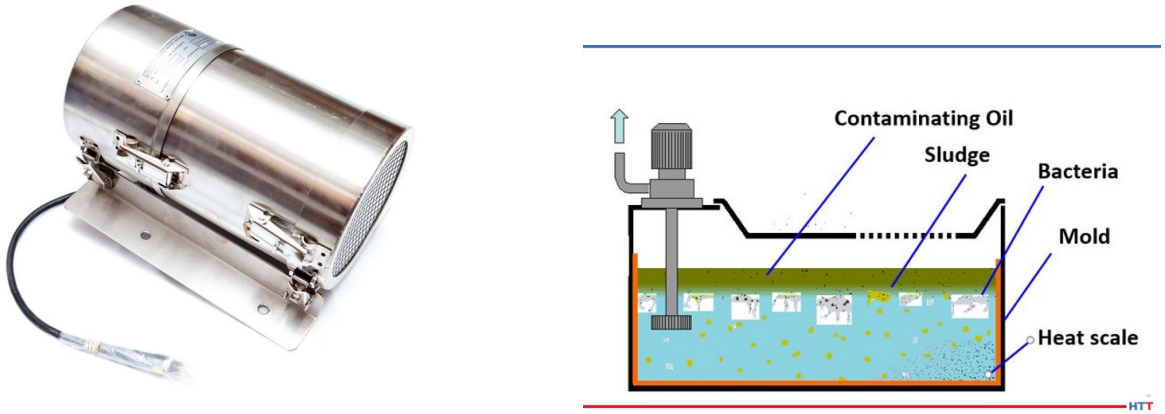

(a) CO_2 Saturation Machine **(b) Quenching**

Fig. 8 Manufacture Process of PEI Foams [25]

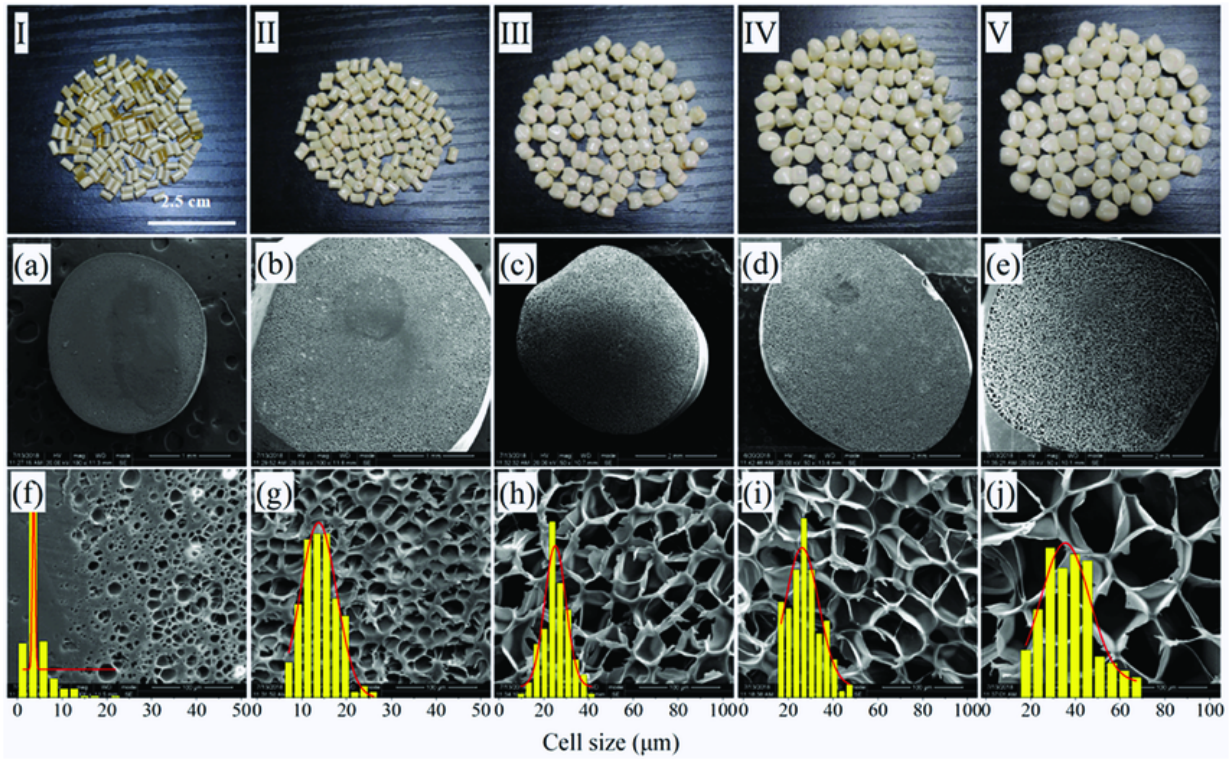

Fig. 9 Macrographs (I–V) and SEM micrographs (a–j) of PEI foamed beads at 190 °C and 12 MPa using CO_2/EtOH as blowing agent. EtOH concentration: (a, f) 0%; (b, g) 15%; (c, h) 30%; (d, i) 45%; (e, j) 60% mol ratio. [25]

Despite the relatively promising future application of polymer nanofoams, there has been a lack of study in the bubble growth model of PEI foaming in nanoscale. With more understanding of the bubble foaming mechanism in nanoscale, the effect on pressure, temperature and viscosity driven by bubble growth can be quantified and enables the prediction of the average of cell size and variances of nanofoams. The linking between cell geometry model to microstructures enables the forecast of Elastic Modulus and yield in polymers. With this, tailoring material in the sandwich carbon composites is possible to develop composite material meeting design criteria without overdesigning or overweighing.

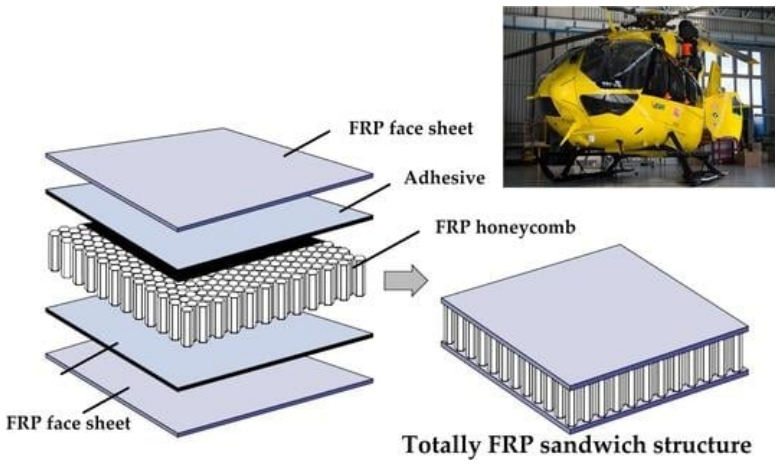

Fig. 10 Demonstration of Sandwich Composites with Polymer as Matrix [29]

Besides the application in aerospace, the bubble growth model can see potential application in medical engineering

through coupling the cell model with mass-transport or cell-adhesion criteria. New-generation treatment may optimize this for pore networks for tissue growth and nutrient diffusion. [30]

Table of Symbols

Symbol	Description
L_0	Original length of the sample
L	Measured length of the sample during testing
w_0	Original width of the sample
t_0	Original thickness of the sample
ε_{LY}	Exported strain from GoM
σ	Stress exerted on the sample
R	Initial outer radius / Temperature sensitivity constant
a_0	Initial inner radius
v_r	Radial velocity of a material element at r
K_H	Constant used to calculate the concentration of CO_2
K_{H2}	Constant used to calculate the concentration of CO_2
M_w	Molecular weight of CO_2
ρ	Density of CO_2
q	Activation energy
k	Boltzmann constant
v	Activation volume
e	Strain in the rubbery regime
n	Strain rate sensitivity constant
τ	Time constant associated with heat conduction into the polymer sample
P_{amb}	Ambient pressure
$\int$	Integral results
s	True hoop strain
f_0	Original porosity
LCFS	Measured displacement in the y direction from the DMA machine

II. Overview of Papers

A. Nano/Micro/Macro Foams

Polymer modeling scale can affect the behavior of foams through different focuses and molecular interactions. In polymer modeling, nanoscale refers to the cell-level cases with unit length counted in nm. Microscale refers to the chain level of polymer with more focus on chain entanglement using a simplified molecular model. Normally microscale analysis is conducted with the unit length in μm. Macroscale refers to the structures composed of billions of molecules and chains. By breaking macroscale structures, microscale and nanoscale properties can be studied, as shown in the picture. [31]

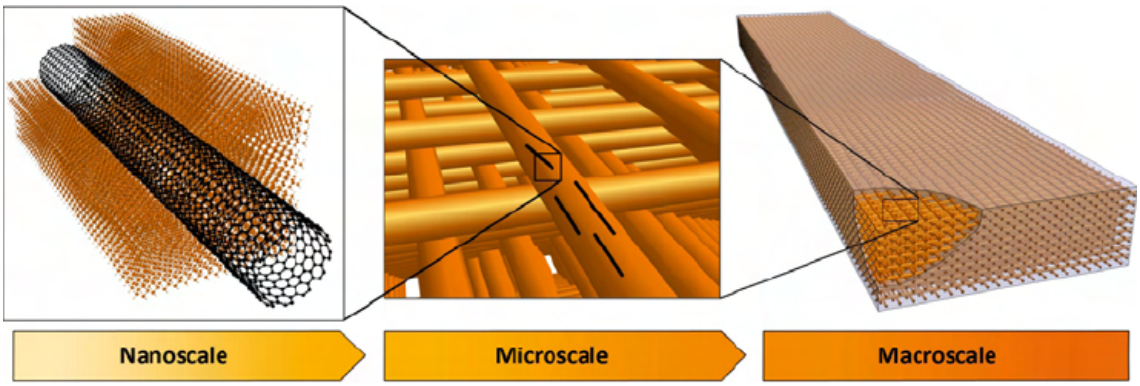

Fig. 11 Demonstration of Scales in Polymer [32]

At nanoscale, atomistic interaction may be captured better and molecular dynamics may be used more frequently. It captures the connection between mechanical response of cells and the whole macro structures with relatively high accuracy but comes with higher computational cost. At microscale, coarse-grained models capture effects like chain entanglement and phase separation by simplifying atomic details, though care must be taken to preserve key thermodynamic and mechanical properties. At macroscale, continuum model requires accurate smaller scale input to predict the viscoelastic behavior and the flow of materials. [33] For the modeling of cell growth model, constitutive equations at nanoscale are needed for accurately capture the behavior of the cell growth and stress responses.

The scale used can also contributes to the differences in mechanical properties of the foams. In nanoscale, nanoparticle composites has more spherical particles and homogeneous distribution. As a result, nanoscale composites significantly improve the mechanical uniformity and wear resistance of polymer composites compared to traditional microparticles. For microscale composites, the irregular, sharp-edges particles leads to non-uniform dispersion which may harm the mechanical performance. [34]

When analyzing the foaming behavior, nanoscale and microscale share some similarities but come with different focus. At nanoscale, foaming tends to begin through nucleation on the surface or the polymer particle itself. Foam is accomplished by the balance between Laplace pressure and environmental conditions which lead to bubble growth or dissolution.[35] At the same time, the diffusion process can be divided into two parallel processes. (1) Along the contact line between the bubble and their surfaces. (2) Through the bubble-gas interface. The high curvature of the bubbles lead to high local pressure and the difference in the rate of diffusion. At microscale, nucleation can be considered as homogeneous and surface area is moderate compared to nanoscale. It allows more consistent cell size distributions and allow more control during the foaming on cooling rate, use of nucleation additives and viscosity. Microfoams display more predictable stiffness and impact resistance based on classical cellular solid mechanics. The high surface area nanofoams can be applied in the areas including biomedical and aerospace engineering with high demand in insulation and mechanical performances. Microscale foams have seen wider application in packaging and structures thanks to matured low cost manufacturing process and predictable properties.

In nanoscale, as foams is consisted of numerous cells with voids inside, the size of the cells can paly a critical role in determining the mechanical and thermal performance of the foam structure. Study has shown that polymer foams with smaller cell sizes contributes to higher tensile and impact strength due to reduced stress concentrations. Conversely, larger cells decrease these properties but it can increase energy absorptions. [36]. On the thermodynamic side, different cells size on various polymer materials exhibit differences in the performance on gas solubility, diffusivity and wall stiffness. Polymer with high stiffness can accommodate more small cells effectively. [37]. At the same time, foams with smaller cells exhibit lower thermal conductivity due to the increased number of cell walls, which act as barriers to heat flow. This structure effectively traps air, making such foams suitable for insulation purposes. Larger cells, while reducing material density, may compromise thermal insulation efficiency. The cell size influences the foam's ability to absorb sound. Smaller cells can dissipate sound energy more effectively, leading to better acoustic damping properties. This makes microcellular foams advantageous in applications requiring noise reduction. [38]

B. Response of PEI under Dynamic Uniaxial Loading

The stress-strain response of PEI under uniaxial tension can be characterized into four distinct stages: elastic, yielding, softening and strain hardening. In the elastic regime, the behavior of PEI is reversible similar to metal, governed by Van der Waals force and the stretch in bonds is minor. As tensile stress continues to increase, PEI tends to reach yielding stage where it undergoes irreversible structural changes due to chain segment mobility and chain rotations. At this stage, PEI structures starts to rearrange through rotation and chain sliding. Once the yield point has passed, strain softening begins accompanied by an increase in fee volume and reconstruction of stress pathways. As a result, there's a temporary drop in stress when strain is still increasing. As deformation continues, the PEI enters strain hardening phase. In this phase, the stress increases with the strain showing increase in the stiffness. Unlike metals, this process of PEI arises from chain alignment and stretching of PEI backbones. As chains align with the load direction, the more resistance to deformation there is, leading to increase in hardening. [39]. The overall stress-strain curve of PEI under uniaxial tension and room temperature can be seen from the plot below [27].

When temperature increases (below glass transition temperature), molecular mobility increases even when PEI chains are still in a relatively rigid configuration. This results in a decrease in elastic modulus. At the same time, as polymer chains have more thermal energy, it can overcome local energy barriers more easily bringing down the yield stress. As temperature increases towards glass transition temperature, PEI undergoes more plastic deformation before failure which results in less significant softening and hardening phase. As the temperature approaches glass transition temperature, strain-induced structural changes such as chain orientation or localized relaxation may begin, softening the response.

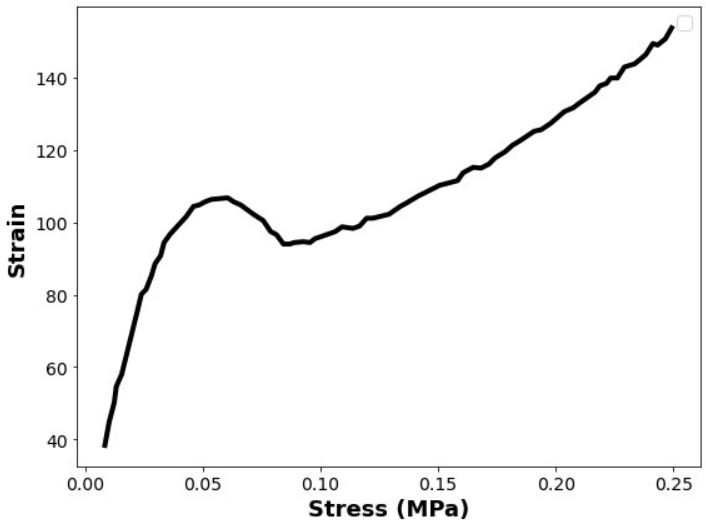

Fig. 12 Stress-Strain Curve of PEI under Room Temperature

C. Existing Foaming Model of Similar Material

Despite the lack of study in the nanoscale foaming mechanism in PEI, numerous studies have been conducted on polymer foams with similar mechanical and thermal characteristics, poly-methyl methacrylate (PMMA) in particular. Van Loock et al. has conducted relevant study on the cell growth modeling of PMMA where PEI growth follows similar physical behavior. [40]

1. Foaming Mechanism

The solid state nanofoaming of PMMA is consisted of three stages including CO_2 saturation, rapid nucleation and cell growth. In the saturation stage, CO_2 diffuses into the PMMA matrix until reaching equilibrium under high pressure of 31 MPa. Such treatment for PMMA usually takes under 20 ms. After that, cell nucleation starts after releasing the pressure to the atmospheric conditions at 100 MPa/s. Such quick pressure drops leads to a supersaturated state for PMMA leading to nucleation of spherical gas-filled cavities. Once nucleated, voids start to

grow as CO_2 diffuses from the molecules into the cavity between the cells. At varying foaming temperatures, void growth typically starts around glass transition temperature when matrix is softened to allow cavity expansion. As the voids grow until approaching neighboring cavities, cell walls reaches equilibrium value. At this point, rather than expanding, transition period starts to transform the structure of PMMA from closed-cell to open-cell, capping porosity. [40]

2. Computational Model of PMMA Bubble Growth

To predict the cell radius as a function of foaming time and temperature of PMMA, a 1D single void model is developed with below stages.

a. Force Equilibrium.
In spherical coordinates, the radical stress and hoop stress are also equal, yields to:

$$\frac{\partial \sigma_{rr}}{\partial r} = \frac{2(\sigma_{\theta\theta} - \sigma_{rr})}{r} = \frac{2\sigma_e}{r}, \tag{1}$$

where $\sigma_e = \sigma_{\theta\theta} - \sigma_{rr}$ is the von Mises effective stress. Integrating from $r = a$ (internal cavity surface) to $r = b$ (outer radius of the finite shell) gives the implicit relation. Pressure equation can be calculated using:

$$p - p_a = \int_{R=a_0}^{R=b_0} \frac{2\sigma_e}{R} \left(\frac{R}{r}\right)^3 dR. \tag{2}$$

where with p the cavity gas pressure and p_a the ambient pressure outside the shell (similar equations were proposed to model plastic void growth from debonded nanoparticles in nanocomposites see e.g. [41, 42, 43, 44, 45]).

b. Conservation of Voids Assume all the cells are sphere and the radius is shown in the figure below. The void size conserved throughout the foaming process, yields,

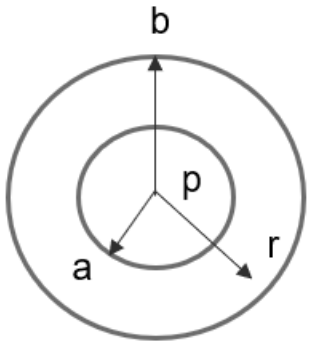

Fig. 13 Conservation of Void Size

$$r^3 - a^3 = R^3 - a_0^3 \tag{3}$$

$$\left(\frac{r}{R}\right)^3 = 1 + \left(\frac{a_0}{R}\right)^3 \left[(a/a_0)^3 - 1\right]. \tag{4}$$

From this relation, the von Mises effective (hoop) strain is show below and can be plugged into stress function above.

$$\varepsilon_e = \frac{2}{3} \ln\left(\frac{r}{R}\right) \quad \Longrightarrow \quad \varepsilon_e = \frac{2}{3} \ln\left[1 + \left(\frac{a_0}{R}\right)^3 \left[(a/a_0)^3 - 1\right]\right]. \tag{5}$$

The corresponding strain rate at r is

$$\dot{\varepsilon}_e = |\partial v_r/\partial r| = 2a^2 R^{-3} \left(\frac{r}{R}\right)^{-3} \dot{a}, \tag{6}$$

where $v_r = (a/r)^2\,\dot{a}$ is the radial velocity of a point at r.

c. Gas Mass Conservation CO_2 is treated as ideal gas in PMMA foaming and the total mass of it is the sum of CO_2 in void and solid shall, which is conserved.

$$C\rho_p(b^3 - a^3) + \rho_g a^3 = C_0\rho_p(b_0^3 - a_0^3) + \rho_{g0}a_0^3 \tag{7}$$

where ρ_p is the density of PMMA.

d. Temperature Profile Dissolved CO_2 lowers the local glass transition Tg of PMMA which is represented using below formula.

$$\theta = \frac{M_{pw}, z, M_{gw}}{(1-C)} \cdot \frac{C}{M_{pw}} = \frac{z, M_{gw}, C}{1-C} \tag{8}$$

where M_{pw} and M_{gw} are repeat-unit and gas molecular weights (100.12 g/mol and 44.01 g/mol, respectively), $z = 2$ (lattice coordination), C' is CO_2 concentration, and

$$\beta = \frac{zR}{M_{pw}\,\Delta C_p}, \tag{9}$$

with $\Delta C_p \approx 355\ \mathrm{J \cdot kg^{-1} \cdot K^{-1}}$ for PMMA–CO_2. This fit captures measured T_g/T_g^0 vs. C data from various studies.

e. Ree-Eyring Relationship The Ree-Eyring model is used to model PMMA when local temperature is normalized by shifted glass transition temperature including both glassy and rubbery scheme. In glassy regime,

$$\frac{\dot{\varepsilon}_e}{\dot{\varepsilon}_0} = \sinh\left(\frac{\sigma_e v}{kT}\right) \exp\left(-\frac{q}{kT}\right) \tag{10}$$

In rubbery scheme:

$$\sigma_e = C_1 \cdot \dot{\varepsilon}_e^{C_2(T/T_g)} \tag{11}$$

D. Modeling Theory

Polymer modeling is a computational approach to describe the dynamics and properties of polymeric materials including PEI. It has a variety of methods including mechanical testing, thermodynamics study, semi-empirical correlation based methods and coarse-grained approaches [46]. It has significant use in engineering, design and theory study. It helps predict the mechanical, thermal and chemical behavior of polymers under different structural designs through CAE and topology study. It also enables designing new materials which optimize polymers with specific properties like strength, thermal stability or density. Traditional polymer modeling methods have been essential in understanding polymer behavior, structure, and properties. These methods primarily involve Molecular Dynamics (MD) and Monte Carlo (MC) simulations, along with continuum mechanics-based models [47, 48]. Molecular dynamics (MD) simulation is used when modeling PEI, which uses Newton's equations of motion to simulate the PEI's movement and interaction of the chains based on time scale. It can also contribute to the study of glass transition during the foaming process. With these advantages, MD is considered as an optimal way of modeling the constitutive relationships of PEI near glass transition temperatures.

F. Van Loock et.al [49] has identified four regimes for a linear, amorphous polymer under uniaxial tension including (1) glassy, (2) glass transition, (3) rubbery and (4) viscous flow regime in the sequence of increasing temperature as shown in the figure 1. In glassy regime, PEI displays brittle and rigid state due to limited mobility of polymer chains. As temperature increases, foaming is introduced and modifies the density and mechanical properties of PEI, which generates gas bubbles within the polymer matrix. The controlled foaming neat Tg allows polymers to expand while maintaining enough strength. Once cooled, foamed PEI can solidify into a semi-glassy state allowing lightweight yet strong material for applications. As temperature approaches glass transition temperature (Tg), molecular motion within

the polymer begins to increase allowing the material to soften leading to a reduction in stiffness and increase in impact resistance. For the majority of cases in aerospace structures applications, polymers need to stay in the glassy regime to ensure structural integrity, stability and resistance to environmental stresses. If the polymer were to transition into rubbery scheme, it may lose its rigidity and could experience excessive deformation or even potential failure under operational conditions. The modeling of PEI is structured as follows. First, the constitutive model of PEI may be derived from kinematics from DMA. Assume the void remains spherical during the whole process and the volume of the bubble remains the same, the constitutive model of PEI can be constructed for as linear, amorphous PEI under molecular deformation processes. Then, DMA on Ultem 1000 PEI is conducted constructing the stress strain response under temperature between 125 C to 205 C before glass transition starts. Lastly, the constitutive equations are calibrated and failure maps can be constructed.

E. Cell Growth Mechanism

Nanofoams are materials with nanometer-scale pores, resulting in high surface area, low density, and exceptional mechanical and thermal properties. They have been seen wide applications in automotive, aerospace, packaging and medical industry thanks to its advantage in weight reduction, enhanced thermal and acoustic insulation and improved dimensional stability. Nanofoams can withstand high-temperature applications due to static surface area interplay with other substances for catalysis and adsorption processes, as well as provide structural integrity during extreme temperatures. In addition to low density, nanofoams possess extensive internal surfaces, making them isotropic for most structural applications. Desired properties on pore structure and porosity require tight control of processing parameters when using chemical gas blowing agents for embedding nanofoams. A blowing agent, polymer matrix, and both temperature and pressure need to work symbiotically. More advancing nanofoams production technologies are most useful for constant and scalable production, making them more widely applicable. It uses a chemical blowing agent into the polymer which decomposes under heat and gases. The gas forms cells within nanofoam matrix leading to cell growth. The chemical gas blowing method can create a more uniform cell structure which is critical in the applications requiring high insulation properties.

In solid state foaming process using CO_2 as blowing agent, the formation of microcellular polycarbonate involves diffusion of gas, plasticization of PEI and glass transition. Under both 1 and 5 MPa foaming pressure and room temperature, CO_2 diffuses into PEI matrix plasticizing the material. This process will lower the glass transition temperature of the PEI which allows cell nucleation and growth during heating. After saturation, when heated between 125 °C and 205 °C, dissolved CO_2 starts to expand inside the bubbles which exerts pressure on the cells and influences their growth. As the cells continue to expand, CO_2 starts to diffuse out of the PEI matrix and into the growing cells. This out-diffusion will bring the glass transition temperature back to equilibrium which is slightly greater than original value as plasticizing effect diminishes. At the same time, the viscosity of PEI matrix increases bringing higher porosity and preventing further cell growth because PEI can no longer allow flow for further expansion. This self-regulating mechanism allows PEI cell size to reach consistant sizes without external control and enables the production of uniform microcellular cells. [50] The flowchart of PEI foaming under CO_2 saturation is shown in the figure below.

PEI foam can occur under varying pressure, temperature, and CO_2 conditions, resulting in a wide range of cell sizes—from the nanocellular scale (approximately 10 nm) to the microcellular scale (approximately 100 μm). This also contributes to a wide range of cell densities, which can reach as high as 10^{20} cells/m^3. It has also been observed that sometimes nanocells may form inside microcells, which is referred as hierarchical cellular morphology. [26] Multiple factors can directly affect the cell structures during foaming process, as shown below.

1. CO_2 Saturation Prior to Foaming

CO_2 concentration prior to foaming plays a fundamental role in polymer cell foaming process. With lower CO_2 concentration, fewer nucleation sites form which reduces the number of larger bubbles due to lack of CO_2 bubbles. Higher gas concentration increases free volume of polymer and lower local viscosity, allowing increase in nucleation events at the same time. Besides concentration, saturation time and pressure also play a role in the effectiveness of saturation. Higher pressure can increase the solubility of CO_2 in PEI thus allow transition from microcells to nanocells

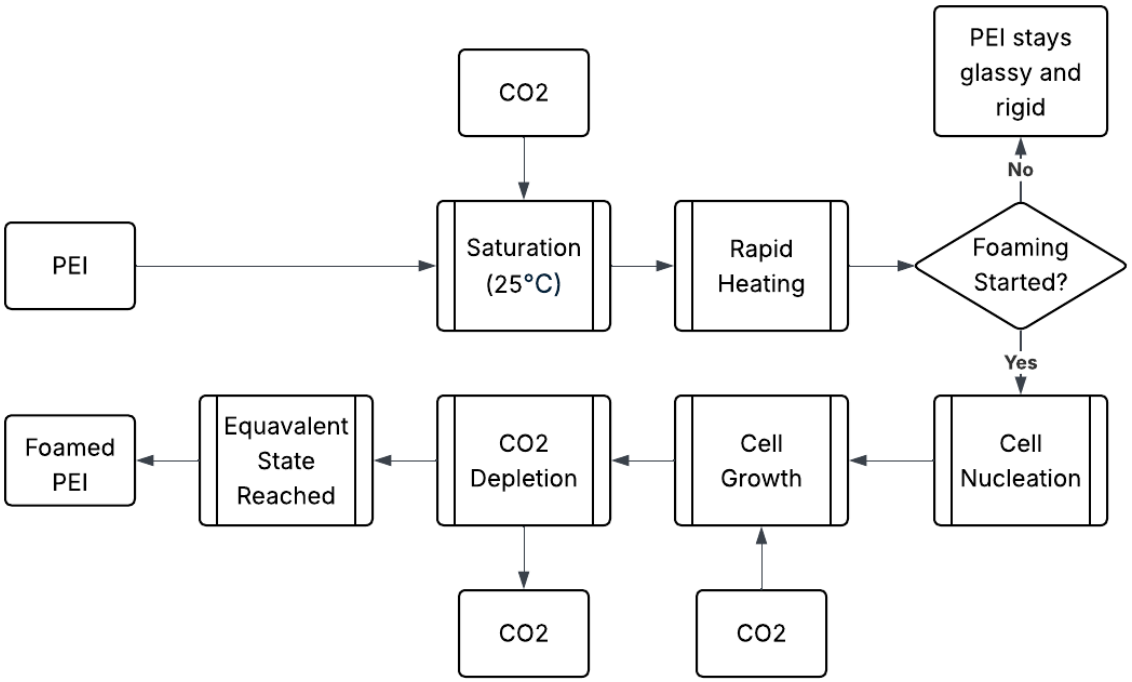

Fig. 14 Flow Chart of PEI Foaming.

by increasing gas content. Following similar mechanism, longer saturation time allows CO_2 to enter thicker samples leading to more uniform cell size after foaming.

2. Foaming Temperature

Foaming temperature can directly affect the glass transition temperature of PEI which leads to direct affect on the foaming. under higher foaming temperature, PEI sample gets closer to glass transition temperatures leading to lower viscosity allowing easier growth of cell bubbles. It also leads to faster depletion and the time takes to reach equivalent state can be reduced. Conversely, lower temperature may limit the mobility of chains which restricts the cell growth. If the temperature is even lower, foaming may not be initiated effectively and cells cannot be produced with uniform shape and PEI will stay glassy and rigid after heating.

F. Factors Affecting the Constitutive Model

Factors including nucleation, activation energy, activation volume, strain rate, etc. may contribute to the change of constitutive model in cell growth and mechanical performances. Some affecting factors and their effects are listed below.

1. Nucleation

Nucleation number refers to the number of nucleation sites form in a polymer system form a metl to a solid crystalline phase which is often expressed as:

$$N_0 = \frac{\text{Number of Nuclei}}{\text{Volume/Mass of Polymer}} \tag{12}$$

It plays a critical role in determining cell size and density during the foaming process. Higher nucleation number may results in smaller cells with more uniformity. It leads to improved mechanical integrity which can distribute stress more evenly and resist deformation or failure under plane stress cases. [51] Nucleation number can be affected by a number of factors during PEI manufacturing and foaming during testing. First, during CO_2 saturation process, higher pressure allows CO_2 to have greater solubility in PEI which increases the number of gas molecules available for phase separation. This contributes to greater nucleation number due to enhanced gas-polymer interaction. During saturation, longer time allows CO_2 to dissolve more, increasing nucleation rates as well. Besides, temperature during foaming can also affect nucleation when cell growth dominates over nucleation. Temperature affects the mobility of polymer chains. When temperature grows higher, the increase in cell size overshadows the effect of the nucleation change. The composition of the polymer blend may also contributes to various nucleation number even under same manufacturing conditions. One example is the combination of PEI and PEEK where PEI adds ductility but PEEK adds stiffness. The different composition of the composites may contribute to difference in nucleation, as shown in the SEM below. Even under same saturation conditions, the difference in PEI/PEEK compositions displays relatively considerable difference in the nucleation. [51]

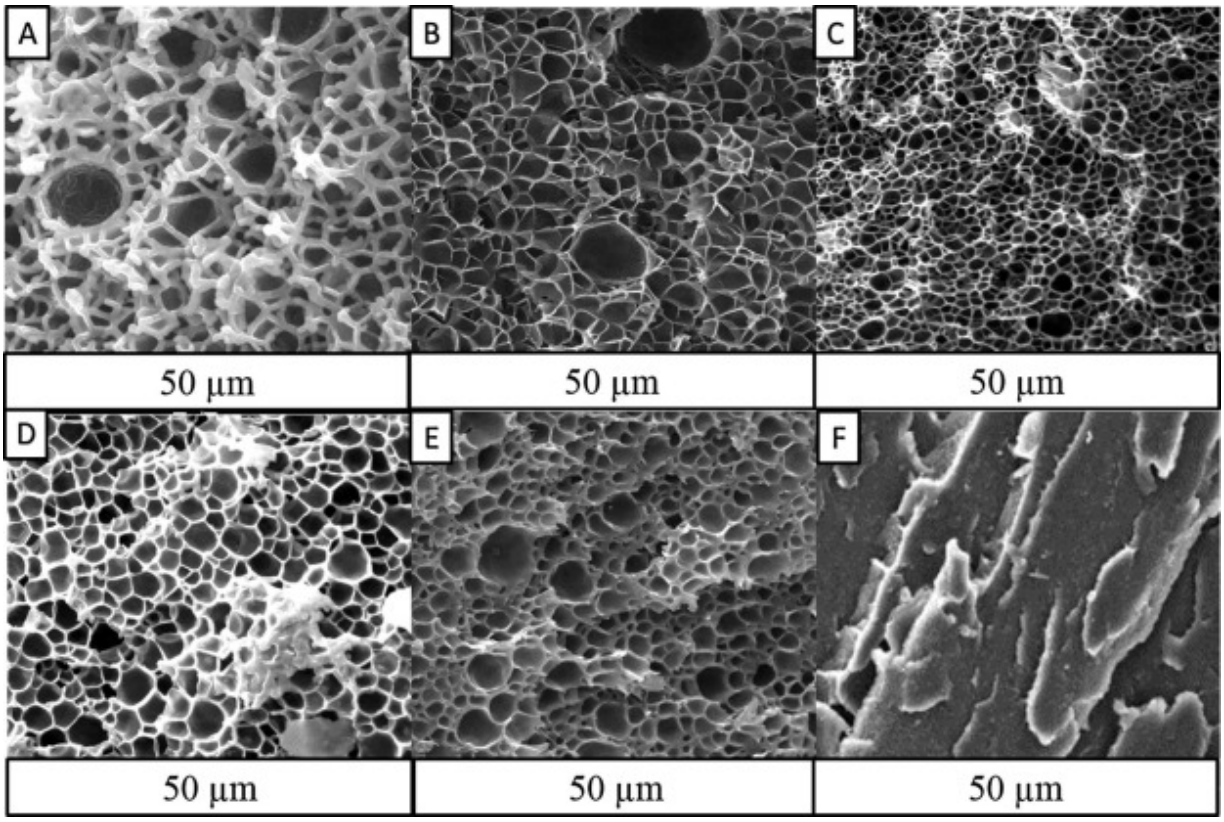

Fig. 15 Difference in nucleation when composition of PEI/PEEK differs: (A) Neat PEI, (B) PEEK 30/PEI 70, (C) PEEK 50/PEI 50, (D) PEEK 70/PEI 30, (E) PEEK 80/PEI 20, (F) Neat PEEK. [52]

2. Activation Energy and Activation Volume

Activation energy refers to the minimum energy required to initiate a reaction. In PEI foaming, it affects the temperatures at which CO_2 decomposes therefore controlling the release and absorption of gas molecules. Activation volume refers to change in volume during the reaction. In CO_2 saturation and foaming, activation can affect the bubble formation by influencing the nucleation and gas bubble entering polymer matrix [53]. When is foamed below glass transition temperature, relaxation of the PEI follows Ree-Eyring equation as shown below, which is defined based on transition state theory and describes the rate of thermally activated process.

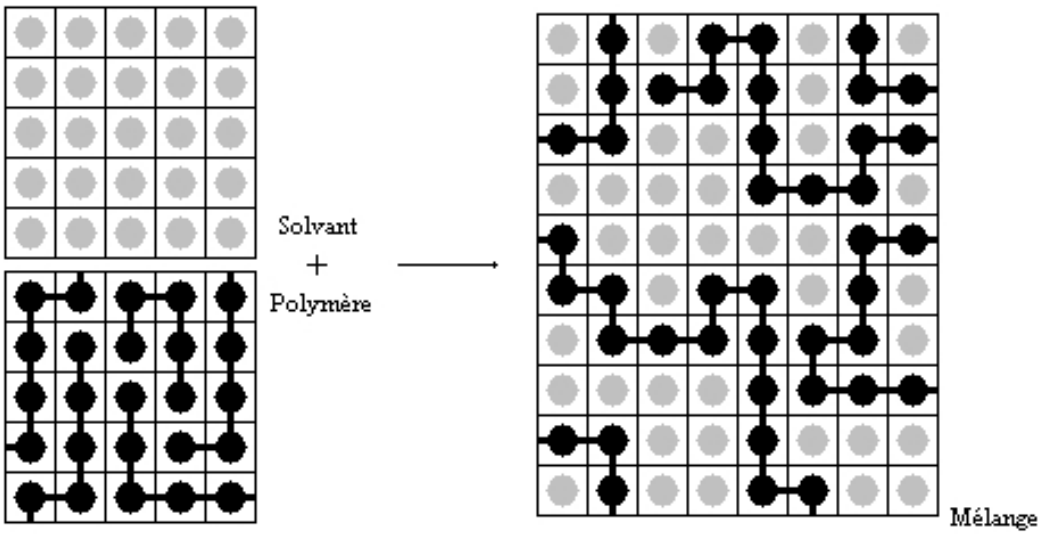

Fig. 16 A simple demonstration of lattice coordination number in PEI.

$$k = \frac{k_B T}{h} \exp\left(-\frac{\Delta G^{\ddagger}}{RT}\right) \tag{13}$$

Where:
- k is the rate constant,
- k_B is the Boltzmann constant,
- T is the absolute temperature,
- h is Planck's constant,
- $\Delta G^{\ddagger}$ is the Gibbs free energy of activation,
- R is the universal gas constant.

Expanding $\Delta G^{\ddagger}$ as:

$$\Delta G^{\ddagger} = \Delta H^{\ddagger} - T\Delta S^{\ddagger} \tag{14}$$

In PEI foaming process, activation volume indicates the relaxation process about segmental motion. It can show correlation with the thermal expansion coefficient over compressibility, where that softer (more compressible) polymers facilitate easier molecular rearrangements. [54] Activation volume tends to be affected by the temperature and pressure during the foaming process. Higher temperature increases free volume thus reducing activation volume. At the same time, higher pressure hinders relaxations with large activation volumes.

3. Lattice Coordination Number

In lattices, coordination number refers to the number of the nearest neighboring atoms or units surrounding a atom in the lattice. When polymer is mixed with CO_2, lattice coordination number can be visualized as ideal case below, where the open circles represent CO_2. The filled circles connected by bonds represent the PEI. Each filled circle is a chain segment whose size is about the same as that of CO_2.

In polymer, The lattice model imagines the polymer solution as a 3D grid (lattice). Each site on the lattice is occupied by either: solvent molecule, or a polymer segment.Flory-Huggins theory is widely used to describe the thermodynamics of polymer solutions, mixtures in particular. In the model, Gibbs energy change can be expressed as:

$$\Delta G_{\text{mix}} = \Delta H_{\text{mix}} - T\Delta S_{\text{mix}} \tag{15}$$

$$\Delta G_{\text{mix}} = RT\left[n_1 \ln \phi_1 + n_2 \ln \phi_2 + n_1 \phi_2 \chi_{12}\right] \tag{16}$$

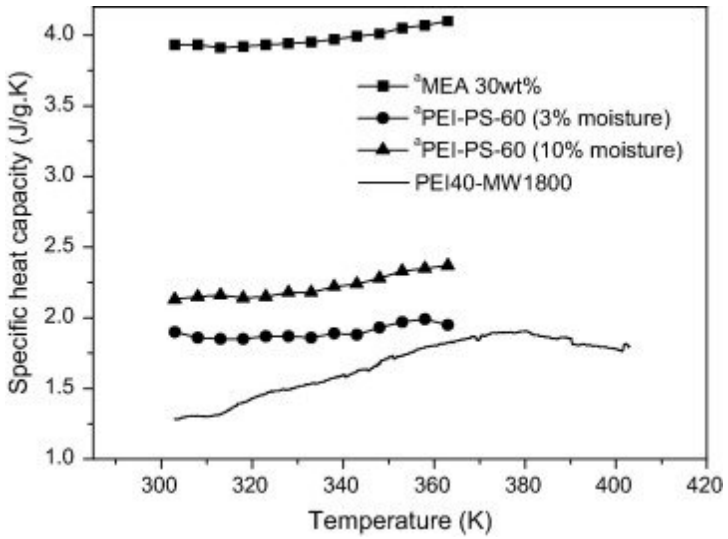

Fig. 17 Specific Heat Values for PEI under Various Manufacturing Conditions [57]

Where:

- n_1 is the number of moles of solvent (component 1),
- n_2 is the number of moles of polymer (component 2),
- ϕ_1 is the volume fraction of solvent,
- ϕ_2 is the volume fraction of polymer,
- χ is the Flory–Huggins interaction parameter, accounting for the energy of mixing,
- R is the universal gas constant,
- T is the absolute temperature.

With the model, free energy of mixing using statistical mechanics can be derived combining both entropic and enthalpic contributions, which helps the prediction of phase behavior on repulsive and attractive interactions. [55]

4. Specific Heat

Specific heat capacity refers to the amount of energy needed to increase the temperature of the polymer by 1 K. It determines the speed samples get heated up or cooled down during the foaming or processing. For thermoplastic material like PEI, specific heat influences how much material can absorb heat without a sharp temperature rise, allowing more stable bubble formation. A lower C_p may result in faster local heating causing uneven foaming or cell collapse. It will also affect the nucleation and lattice coordination. [56] Specific heat affects polymer foaming by influencing how heat is absorbed, transferred, and stored during both processing and in-service conditions. It governs reaction rates, foam structure uniformity, and the foam's resistance to thermal damage. Also, moisture may also contributes to the variation of C_p, as shown in the figure below [57].

5. Heating Rate

In DMA, heating rate needs to be set properly to allow optimal foaming process and avoid stress concentration. Heating rate has a linear relationship with the activation energy required for glass transitions. It considerably affects the molecular mobility thus contributing to change in viscoelastic transitions. [58] At the same time, glass transition temperature may also be affected by the heating rate, where lower heating rate will take longer for polymer to heat uo uniformly which shifting up glass transition temperatures. An Arrhenius Equation is introduced to account for the effect of heating rate.[58]

$$\log a_T = \frac{b_T E_a \log e}{R}\left(\frac{1}{T} - \frac{1}{T_r(b_T)}\right) \tag{17}$$

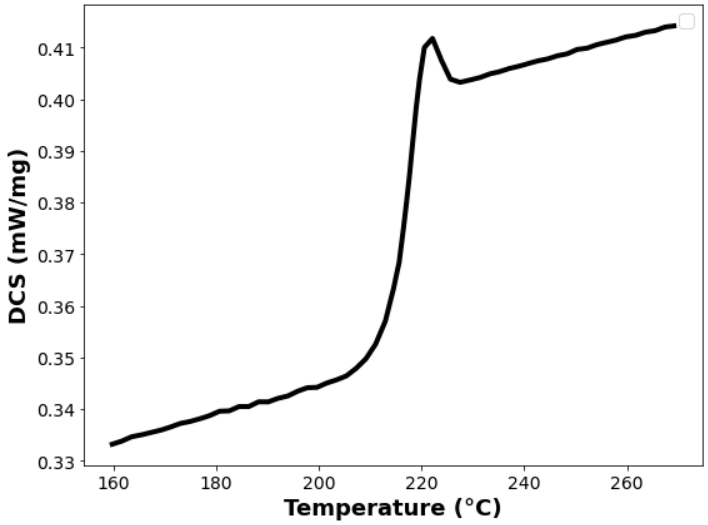

Fig. 18 PEI's Thermal Conductivity with Subject to Temperature.

where

Symbol	Meaning
a_T	Shift factor (dimensionless), relates frequency shift at temperature T to reference T_r
$\log a_T$	Base-10 logarithm of the shift factor
b_T	Heating rate factor (dimensionless), normalized such that $b_T = 1$ at a reference rate
E_a	Activation energy (J/mol), energy required for viscoelastic transition
$\log e$	Conversion factor from natural logarithm to base-10 (approximately 0.434)
R	Universal gas constant (≈ 8.314 J/mol·K)
T	Current temperature in Kelvin
$T_r(b_T)$	Reference temperature in Kelvin, dependent on the heating rate

Also, thermal shock during heating due to high heating rate can also affect the effectiveness of DMA. Thermal shock occurs when polymer is subjected to rapid temperature changes leading to uneven expansion due to internal stresses. As shown in the figure [59], PEI has a thermal conductivity of $0.22W/(m * K)$ and thermal expansion coefficient of $50 \times 10^{-6}\,\mathrm{K}^{-1}$, which is considered inefficient when conducting heat but has higher tendency to expand when temperature changes. For PEI samples in DMA, the non-uniform heating may lead to temperature gradient within the material. If the internal stresses exceeds PEI's mechanical strength, they can result in cracking or failure which will harm DMA's efficiency and the validity of the results. Because of it, heating rate of PEI during DMA needs to be controlled. Gradual heating and cooling allow the material to adjust uniformly, reducing internal stresses.

6. Strain Rate

In DMA, an oscillatory stress is applied resulting strain, so strain rate can influence the mechanical behavior during DMA. At a lower strain rate, PEI chains have longer time to rearrange in response of stress which makes the results dominated by viscous flow. In this case, samples may display greater deformation and energy dissipation. Conversely, higher strain rate leads to more elastic behavior due to short time for polymer chains to rearrange, resulting in a stiffer response. Because of that, failure mode can also be differed under different strain rate. PEI shows ductile failure under quasi-static loading (low strain rates), where plastic deformation occurs before failure. Under dynamic loading (high strain rates), the same material exhibits brittle failure, fracturing with little to no plastic deformation. This transition is

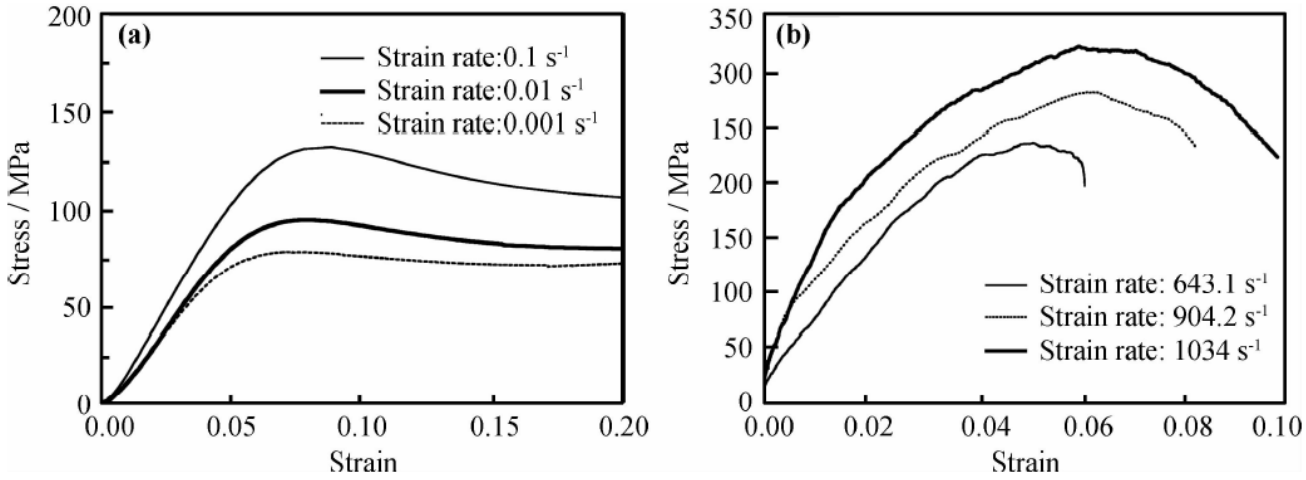

Fig. 19 Stress-strain Curves of PMMA from Different Strain Rates

attributed to the inability of polymer chains to respond quickly to rapid deformation, limiting energy dissipation and promoting crack propagation. PEI and PMMA share similar mechanical responses under uniaxial tension and below figure shows the response of PMMA under DMA with different strain rate. [60] Also, when strain rate is high, there's more like hood of excess heat generated from plastic work leading to thermal softening, especially during foaming process where PEI itself is experience softening at temperature grater than $0.75T_g$. This will lower the material's strength post-yield. [61].

III. Method

A. DMA

The Dynamic Mechanical Analysis (DMA) method has been widely applied in studies of behavior of polymer materials subjected to a dynamic or steady deformation. The stress controlled dynamic mode consists of measuring the strain in the sample, while applying a controlled sinusoidal or waveform stress. It is also possible to work with strain control. When uniaxial stress is causing deformation on the polymer specimen, DMA can measure energy stored or dissipated within the process. [62] DMA can also be considered as a thermal analysis technique when temperature is controlled during the test. When constructing a constitutive equation of PEI under uniaxial tension, DMA can be applied as an optimal testing method to analyze its viscoelastic behavior under various temperature settings under given strain rate.

For polymeric materials, they do not deform easily in the glassy regime but will deform easier as the temperature increases to rubbery regime. The transition temperature is referred as glass transition temperature (T_g). In the glassy regime, the loss modulus is small and storage modulus is large. At higher temperatures, loss modulus increases to the maximum around glass transition and decreases after entering rubbery regime. Storage modulus will also decrease after reaching T_g, which is shown in the figure below. [63]

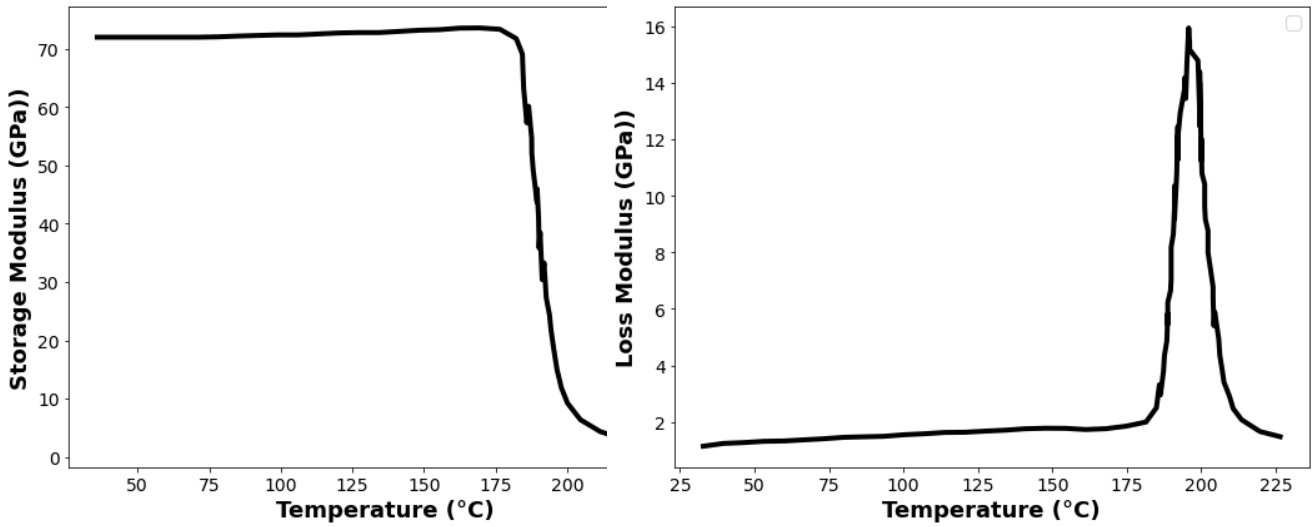

(a) Storage Modulus **(b) Loss Modulus**

Fig. 20 Relationship between Storage and Loss Modulus of PEI and Temperature below T_g

Because of PEI's change in viscoelastic behavior, compared to tradition uniaxial tension and compression testing, DMA can better capture the behavoir using simplified string-mass model. [64]. The motion for the damped driven oscillator is

$$M\frac{d^2x}{dt^2} + B\frac{dx}{dt} + Kx = F_0 \sin(\omega t) \tag{18}$$

At resonance, the displacement is:

$$x = x_0 \cos(\omega t) \tag{19}$$

Substituting into the differential equation and comparing coefficients yields:

$$K = M\omega^2 \tag{20}$$

$$\omega B = -\frac{F_0}{x_0} \tag{21}$$

Where:
- M: mass of the oscillating body
- B: damping coefficient (friction)
- K: spring constant
- x: displacement from equilibrium
- F_0: amplitude of the applied sinusoidal force
- ω: angular frequency of oscillation
- x_0: maximum displacement

With the oscillation, DMA can measure the response of polymer in both elastic and viscous behaviors. It allows rapid and sensitive detection of the glass transitions from changes in mechanical property like modulus, damping and compliance function of temperature and frequency. It provides a accurate tool for understanding the molecular and structural response of PEI under mechanical stress. [65] In the modeling of PEI cell growth model, DMA is used on determine the stress-strain response of the PEI dog-bone samples. The flow of the process is shown in the flow diagram below.

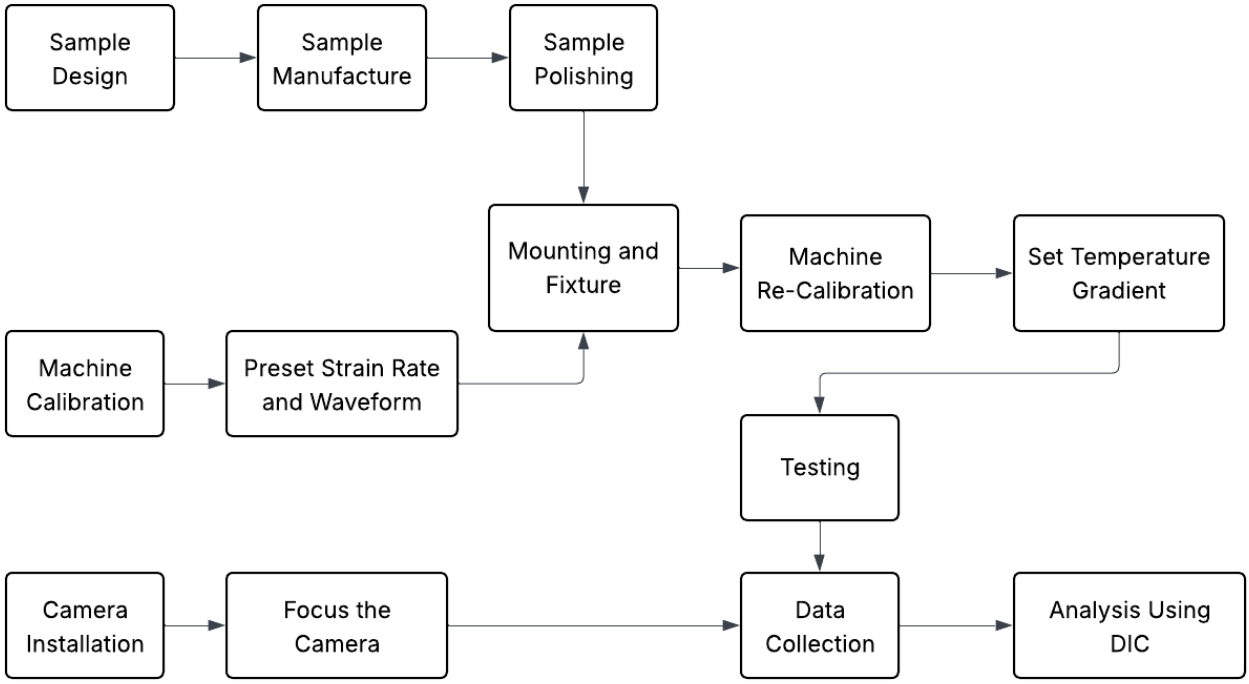

Fig. 21 Flow Chart of DMA on PEI Samples.

Van Loock et al.[49] proposed the testing for failure mechanism of a linear, amorphous polymer like PMMA in terms of molecular processes by tensile test. Constitutive laws can be derived from the measured stress-strain curves as well as failure maps. In the testing, 3mm dog-bone-shaped PMMA sheets were used which were attached by aluminum alloy tabs using temperature-resistant epoxy. Tensile tests are performed ranging from 80°C to 185°C with a heating rate of 10°C/min until the specimen fails or maximum displacement is reached. Strain can be measured by the change of slope in dots at mid-section. To avoid scattering, through-thickness strain can be assumed to be equal to transverse strain as well as average measurement. Then the true tensile strain can be derived by the formula below

$$\epsilon = ln\frac{L}{L_0} \tag{22}$$

Fig. 22 Tensile Test with Temperature Gradient.

Van Look et al. studies the foaming model of PMMA under the saturation of CO2. Solid-state experiments are done by heating up PMMA plates and the compressing. Foaming was performed in a pressure vessel by saturating CO2 under pressure of 31MPa for 24 hours. Then, pressure was released at a rapid rate for nucleation. Finally, samples were foamed in a foaming bath under various temperature and time for void growth. [40]

B. Mechanical Response of PEI under DMA

In Dynamic Mechanical Analysis (DMA) of PEI, true strain is used in stress-strain curves because it provides a more accurate representation of material deformation for large or non-linear strains similar to the testing performed. Unlike engineering strain, which only considers the initial length, true strain accounts for the continuous changes in length and cross-sectional area as PEI sample deforms. This is important for accurately capturing the viscoelastic behavior of PEI under dynamic and cyclic loading conditions, ensuring a more realistic analysis of their mechanical properties.

The mechanical responses of PEI can be marked by four distinctive mechanical regimes before rupture: (i) linear elastic, (ii) nonlinear elastic, (iii) strain softening, and (iv) strain hardening [49]. At the initial phase, PEI exhibits a linear elastic response behaving in a Hookean manner. The slope of the linear curve may be approximated as Young's Modulus of the material. As deformation continues, localization starts to increase the level of stress nonlinearly until it reaches the local maximum in stress, which is considered the yield strength. This process tends to happen with 1% of the strain. Upon reaching the yield stress, PEI exhibits a softening regime due to volume expansion as a result of reduction of mobility and increase of free volume while PEI shifts to equilibrium. Then the material starts to experience strain hardening because the polymer chain aligns in the direction of the force until reaching the critical stress and raptures.

C. Digital Image Correlation (DIC)

Digital image correlation (DIC) is a non-contact technique used in mechanical testing to measure the displacement and strains on the surface during deformation. It has been seen a wide use in mechanical testings due to its ability to capture detailed deformation on specific regions of interest [66, 67, 68, 69]. In DIC of PEI samples, a high-contrast and random pattern is applied on the surface prior to testing. During the testing, images are taken by a camera to capture the surface under loading condition. Then, the acquired pictures are divided into small subsets using correlation software and are analyzed to determine the displacements and strain for further calculation. The flow can be seen in the below flowchart. In the modeling of PEI using DMA, DIC can enable the detailed analysis of micro-mechanical behavior by showing the full-field strain mapping. It reveals how strain is localized different in the polymer and interface zones [52, 27].

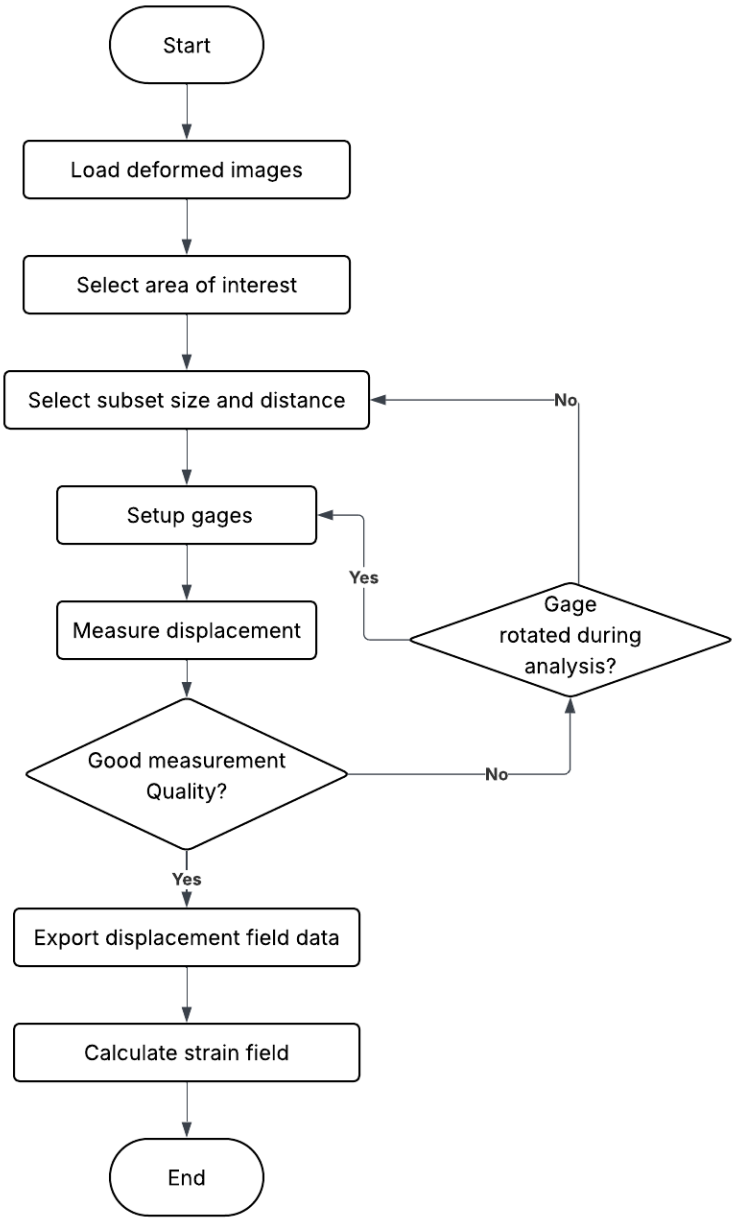

Fig. 23 Flow Chart of DIC on PEI Samples.

D. Polymer Deformation and Modeling Theory

The deviation of the constitutive model of PEI can be referred to the process of the deviation of PMMA. According to Can Loock et al. (2018) [49], the constitutive model of PMMA may be derived from kinematics from DMA.

It is assumed that the effective stress of PEI-CO_2 system at a given strain rate under a certain temperature is same as PEI solid without CO_2 saturation. At the same time, perfect circle is assumed for all the bubbles and deformation of cell wall only occurs when true strain is equal to the failure strain. The deviation of constitutive equation of PEI can be divided into three parts: stress and heat relationship, deformation mapping and bubble foaming.

1. Stress and Heat Relationships

The true tensile strain is given by:

$$\epsilon = \ln\left(\frac{L}{L_0}\right) \tag{23}$$

where L_0 is the original length of the sample, and L is the measured length during testing. Assuming the bubbles before and after foaming are perfect circle, the effective strain can be calculated as: The effective strain rate is:

$$\epsilon' = \left|\frac{\delta v_r}{\delta r}\right| = 2a^2R^{-3}\left(\frac{r}{R}\right)^{-3}a' \tag{24}$$

where v_r is the radial velocity of a material element at r.

The Von-Mises effective strain is given by:

$$\epsilon_e = 2\ln\left(\frac{r}{R}\right) = 2\epsilon \tag{25}$$

With LCFS exported from the machine, together with measured size of the sample, the deformation of the sample and the strain can be calculated using basic definition of strain:

$$w = w_0\left(1 - \left|\frac{\epsilon_y}{100}\right|\right) \tag{26}$$

$$t = t_0\left(1 - \left|\frac{\epsilon_y}{100}\right|\right) \tag{27}$$

$$\epsilon_t = \left|\ln\left(1 + \frac{\epsilon_y}{100}\right)\right| \tag{28}$$

$$\sigma = \frac{LCFS}{wt} \tag{29}$$

where ϵ_y is the measured strain in the y-direction, w_0 and t_0 are the original width and thickness, and $LCFS$ is the measured force.

On the heat size, Henry Gas Law is used to calculate the concentration of CO_2 after the saturation and the amount of CO_2 dissolved in PEI after the foaming, which directly influences the size of the cell after foaming as well as the porosity.

$$K_{H2} = K_H\frac{M_w}{\rho} \tag{30}$$

where K_H and K_{H2} are Henry's law constants, M_w is the molecular weight of CO_2, and ρ is the density of CO_2.

When performing DMA, a uniaxial dynamic load is applied on the sample which causes deformation under a given temperature. The temperature profile in DMA testing is:

$$T = T_0 + (T_f - T_0)(1 - e^{-t/\tau}) \tag{31}$$

where τ is a time constant associated with heat conduction.

When reaching the equilibrium after foaming, DMA will continue testing until reaching desired strain or structural failure occurs. In this process, stress reaches equilibrium when:

$$y = (P - P_{amb}) - \text{int} \tag{32}$$

where P_{amb} is the ambient pressure, and int refers to integral results.

where ϵ_s is true hoop strain, and f_0 is the original porosity.

2. Deformation Mapping

When the temperature is below glass transition temperature, PEI tends to display a relatively glassy behavior. In this period, foaming has not yet started and Young's Modulus follows a relatively linear pattern with change due to vibrational energy of chain segments. [49].

$$E_g = E_0 \left(1 - \alpha_m \frac{T}{T_g}\right) \tag{33}$$

where α_m refers to a tuning coefficient. In large strain response, the stress-strain response is alomost linear and brittle.

When temperature approaches glass transition temperature ($0.8<T/T_g<0.95$), foaming starts to take place and shear yielding starts to follow an elastic behavior. Necking starts to happen due to load drop from yield and increase in strain sensitivity which will result in drop in load displaying softening-like behavior. After the neck finishes the propagation, load can continue to increase until ultimate strength when the whole structure fails. As temperature continues to increase close to glass transition temperature ($0.95<T/T_g<1$), with Van der Waals bond melting, PEI becomes so strain-sensitive that the neck growth becomes less significant which may lead to the absence of load drop at yield and eventually neck will not form when reaching T_g [49]

Ree-Eyring equation can relate the stress in glassy and transition regimes as a function of T/T_g and strain rate.

$$\epsilon_e' = \sinh\left(\frac{\sigma_e v}{kT}\right) \exp\left(-\frac{q}{kT}\right) \tag{34}$$

where q is activation energy, k is Boltzmann's constant, and v is activation volume.

In the rubbery regime, stress is given by:

$$\sigma_e = E_0(1 - \alpha_R \frac{T}{T_g}) \left(\frac{\epsilon_e'}{\epsilon_R'}\right)^n \tag{35}$$

where α_R is a temperature sensitivity constant, ϵ_e is the strain in the rubbery regime, and n is a strain rate sensitivity constant.

With relatively low molecular weight, similar to PMMA with low molecular weight, a linear, viscous flow model can be used to describe the behavior of PEI in the glass transition regime.

$$\sigma_e = 3\eta\dot{\varepsilon}_e, \tag{36}$$

where η refers to viscosity which is independent from temperature and pressure.

$$\eta = \eta_0 \exp\left(\frac{-C_1\left(\frac{T}{T_g} - 1\right)}{C_2/T_g + \frac{T}{T_g} - 1}\right), \tag{37}$$

where η_0 is reference viscosity and C_1, C_2 are tuning parameters used later in linear curve fitting.

3. Bubble Foaming

With the deformation mapping, bubble growth model can be established by solving equilibrium equations including conservation of mass, volume of bubble and heat equations. The void growth can be calculated using integration. The initial porosity is calculated as:

$$f_0 = \left(\frac{a_0}{b_0}\right)^3 \tag{38}$$

and is estimated to equal 0.6-0.9 for PEI nanofoams. The initial void radius a_0 is estimated by

$$a_0 \approx \left(\frac{3f_0}{4\pi N_d}\right)^{1/3} \tag{39}$$

where the cell nucleation density $N_0 = 1\times10^{21}$ m^{-3} for PEI nanofoams under 1 MPa saturation and $N_0 = 2\times10^{23}$ m^{-3} for PEI nanofoams under 5 MPa saturation.

Assuming the cell are perfect circle and deformation of cell wall only occurs when true strain is equal to the failure strain. Given solids around the expanding bubbles are incompressible, the displaced radius can be calculated as:

$$r^3 - a_0^3 = R^3 - a_0^3 \tag{40}$$

where R and a_0 are the initial outer and inner radii.

By plugging it into the equation above porosity calculation can be updated as

$$f^{-1} = 1 + \exp(-3\varepsilon_s)(f_0^{-1} - 1). \tag{41}$$

where, when the cell wall occurs:

$$\epsilon_f = \epsilon_s = \ln\left(\frac{a}{a_0}\right) \tag{42}$$

IV. Experiment

A. Material and Equipments Used

1. Material Used

DMA testing was consucted on PEI ULTEM 1000 grade with a average repeat unit molecular weight M_w=59200 g/mol and sheets with average thickness of 0.5mm. It hasthe density ρ=1270 kg/m^3 and glass transition temperature of T_g=217 ℃. Without saturation, it has a Young's Modulus E=3.3 GPa under room temperature. Carbon dioxide (CO_2) is used for blowing agent

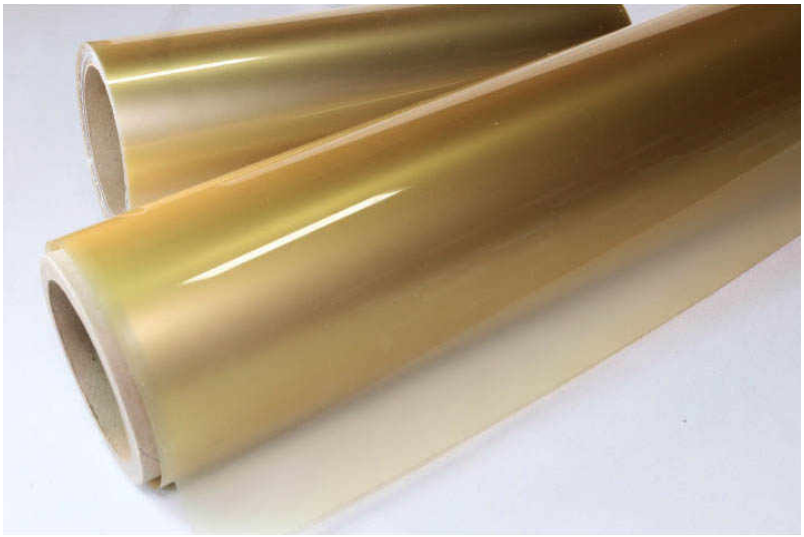

Fig. 24 ULTEM 1000 PEI Sheet Used for DMA Testing.

2. Equipment Used

The equipment utilized in the testing procedure includes pressure vessel, universal testing machine TA Instrument ElectroForce DMA3200 and digital camera FujiFilm-X-A7 with FujiFilm 16mm Micro Lens. These instruments were chosen based on their ability to meet the criteria specified in both papers to saturate and apply temperature and pressure in different specimens under various conditions, as well as easing the difficulty of post-processing on image processing. The equipment used are shown in the figure below.

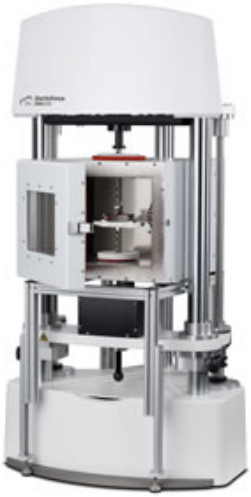

Fig. 25 DMA Machine Used.

B. DMA Procedure

The steps outlined in both papers have been carefully reviewed and applied in the DMA of the nanofoams. The process and equipment used are listed below.

1. Testing Parameters

Under pre-selected temperature and pressure, by setting up strain rate at 0.00625%/s, DMA can be executed with samples under various initial conditions. The measured parameters from the DMA include:
LCFS: Measured displacement in the *y* direction from the DIC machine.
t: Testing time which can be used for future plotting.
T: Temperature inside the chamber during testing.
L: Load applied on the specimen

2. Test Execution

The testing parameters, including load, temperature, pressure, saturation of CO_2, etc., were meticulously noted and replicated as closely as possible to adhere to the standards set by both papers and can be applied for future curve-fitting purposes.

i Sample design
Instead of a rectangular shape sample that causes slip during testing, a dog-bone shape based on the design of Oddone et al. [70], as shown in the figure below.

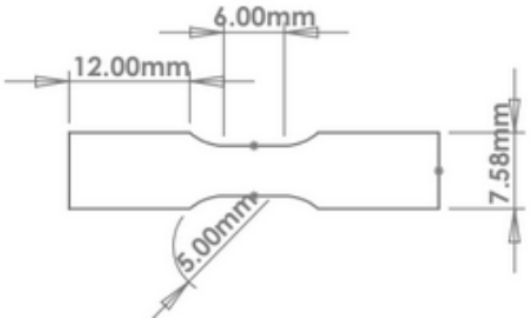

Fig. 26 CAD Design of Dog-bone PEI sample.

In the tests on the aforementioned sample, necking is discovered in the majority of samples (picture is shown below). One possible explanation is the difficulty of sanding on the sharp edge on the specimen. Because of that, a fillet is added on the CAD of the specimen as shown below, which is made by waterjet.

(a) Necking Discovered in DMA.

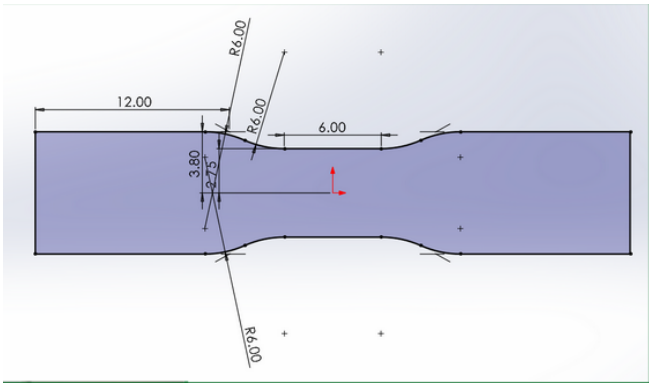

(b) Updated Design to Avoid Necking.

Fig. 27 Necking and Prevention by Changing Sample Shape.

ii Sample Manufacture

As mentioned above the updated samples are made through waterjet to achieve higher accuracy and efficiency compared to machining. Then, 2000 grit sandpaper was used to clean the surface of the sample surface to remove sharp edges, enhance grip and avoid unexpected failure during testing under a microscope.

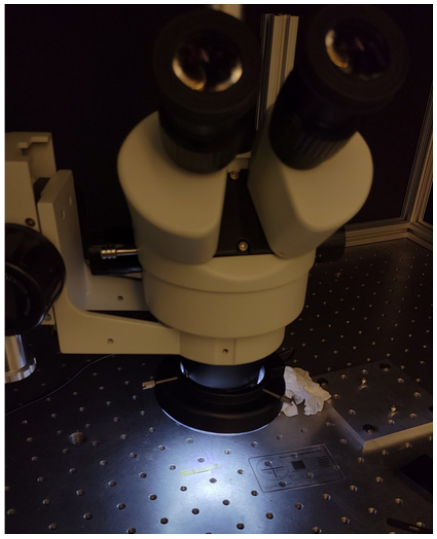

Fig. 28 Preparation of the samples by filing and quality check under a microscope.

After polishing, the edge of the samples displays a relatively shiny and transparent surface with white particles being removed. Then, the size of the samples is measured again, numbered, marked and grouped to prepare for the later steps. Tattoo paper is attached in the middle section to make it easy for photo capture and analysis. Finally, all the samples went through drying process to remove the moisture on the surface.

iii CO_2 Saturation

Grouped samples were treated with saturation under various gases in the pressure vessel under 5MPa for 24 hours. Before saturation, samples were distributed in paper coverings to ensure the effectiveness of the saturation process.

Half of the samples were saturated by air and another half were saturated by CO_2. Saturation is performed in a pressure chamber with pressure and temperature controller. High purity CO_2 served as blowing agent which helps nucleation and absorption of PEI. During saturation, the samples were held in the pressure chamber with 1 MPa or 5 MPa pressure under room temperature for 24 hours to ensure adequate absorption of CO_2 into PEI. Then, the pressure was released to room pressure with high rate around 100 MPa/s to allow nucleation. Before the start of DMA, samples were bathed under selected foaming temperatures with 10 ℃temperature gradient for each sample (175℃to 205 ℃for samples saturated under 1 MPa and 135 ℃to 175 ℃for samples saturated under 5 MPa.) The heating rate in this process needs to be controlled low to prevent heat shock which may harm the stability of the cell structures. This allows the void to grow. After bathing for 1 minutes after reaching target temperature, DMA can start.

iv Testing

After setting up the testing machine and camera in front of the testing machine, tensile tests are performed ranging from room temperature to 250°C with a heating rate of 10°C/min until the specimen fails or maximum displacement is reached. The ramp rate can be calculated using the formula below

$$RampRate = StrainRate * GageLength; \tag{43}$$

where gage length is set at 5mm to reserve adequate grip length to minimize slipping. The camera was set to capture one picture per second to record the deformation process for post-processing on GoM. Camera needs to be placed perpendicular to the object in both horizontal and vertical directions to avoid residue strain due to out-of-plane movement of the object. Also, scaling is needed to capture the full image of the specimen. During the process, time, load and displacement are recorded by the machine for future analysis. During testing, some specimens failed away from the maximum displacement possible. Analysis was made on them with several possible explanations: i). There were defects or dust on the specimen surface which led to slip during testing; ii). The alignment of the specimen and vertical axis may have some errors during clamping which led to undesired shear on the specimen. After the testing, let the machine cooled down to room temperature and remove the specimen.

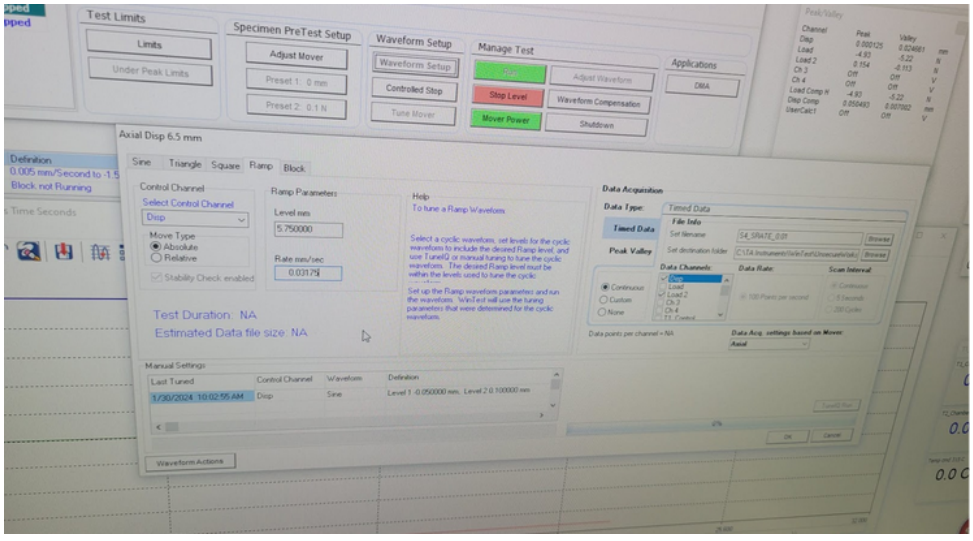

Fig. 29 Setup of the universal testing machine with temperature gradient and strain rate.

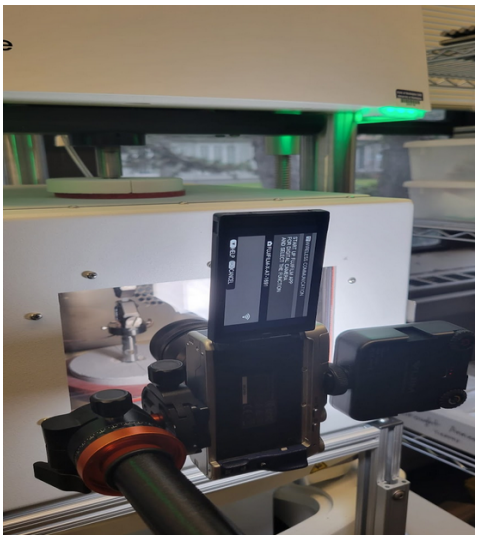

Fig. 30 Setup of all the equipment before testing.

C. DIC Procedure

i Image/Video Analysis

The displacement can be visualized from the images and videos obtained during testing through 2D GoM software. GoM can apply an optical method to measure 2D or 3D coordinates based on stochastic patterns, in which the software can calculate coordinates on the deformed pattern in each image with full process of strain and deformation visualized. The tattoo paper mentioned above can provide contrast on the specimen.

The steps can be shown as follows

Step i). Start a new project, import the images in the inspection section. Choose "Deformation" images and the system will automatically create a measurement series.

Step ii). Create surface component: first, select the desired region of selection by drawing a polygon around the image. Then, set the parameters with facet size and point distances. Pattern quality function can be applied to check the quality of the selection, with which it's needed to change the pixels of fact size and distances until most part of the specimen needed is marked green to achieve better analysis quality.

Step iii) Set up coordinate system: under "create alignment" menu, "3-2-1" alignment may be applied by setting up three points for a plane, two points for a line and one point for y. For 2D case, default coordination system can also be chosen as the coordinate system. Make y direction aligns with the tension in the machine during testing to avoid components in x direction which may affect the accuracy of the plotting.

Step iv) Check and set up strain parameters: in the "Check" menu, select epsilon y strain to compute the strain in the y/tension direction. Select the desired strain representation, in the current DMA case "Technical Strain" was chosen.

Step v) Plot visualization: select epsilon and distance in the respective direction (x or y) and the start "Diagram" to plot the strain relationship based on the given extensometer. To plot strain relationship, parameters including length change, strain and distance in both x and y direction may need to be selected.

The initial display on GoM with 0 strain should look like figure below.

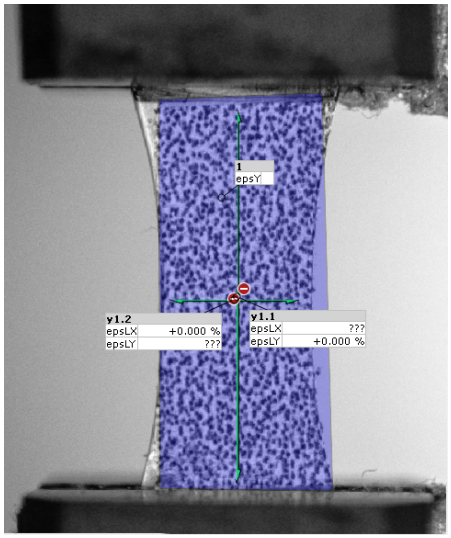

Fig. 31 Initial Setup of GoM Before Deformation.

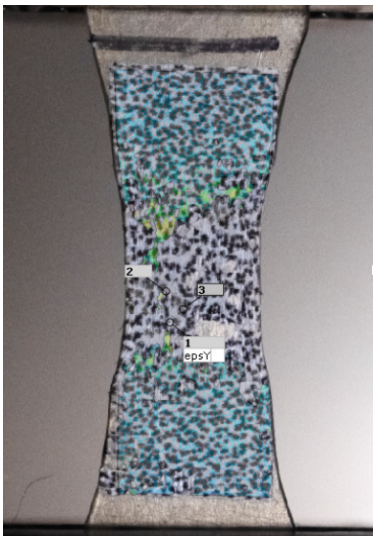

Fig. 32 DIC picture of deformed nanofoam under uniaxial strain on y direction at 390s in the test with marked deformation in x and y direction.

Step vi) Create report page and document findings: Turn the software into "Report" workspace, select the desired report type including graph, 3D image, videos, etc. Adjust the zooming of the images when needed.
The strain curve looks as follows:

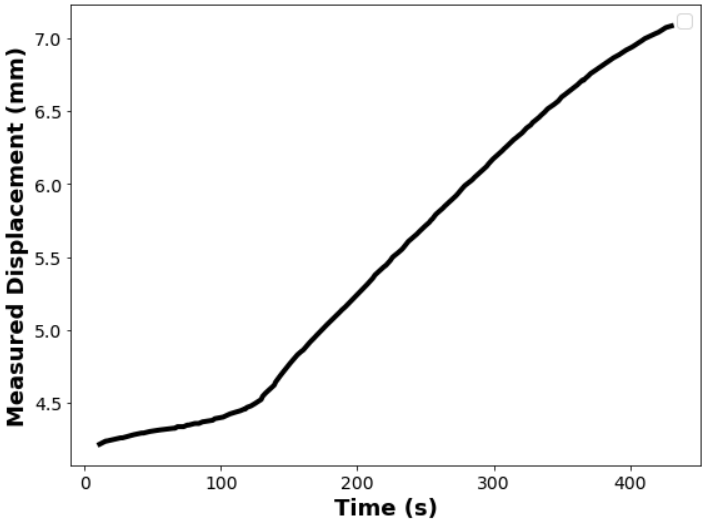

Fig. 33 Tensile Strain in y Direction with Respect to y Coordinates.

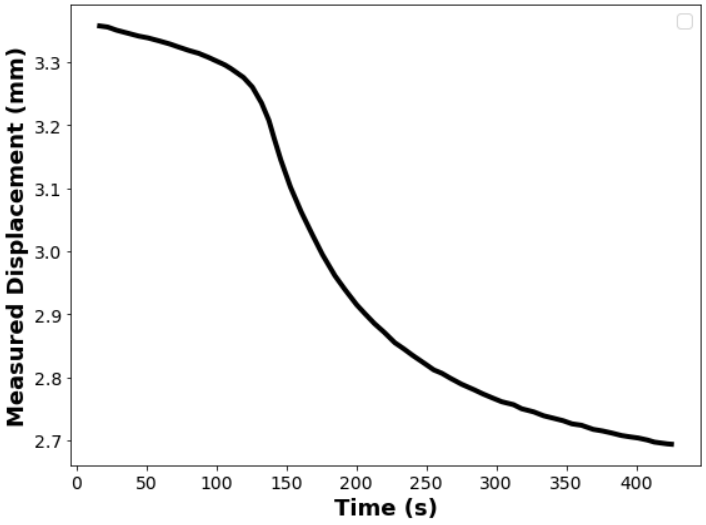

Fig. 34 Tensile Strain in y Direction with Respect to x Coordinates.

ii Plots Interpretation

Strain plots obtained from the testing phase will be analyzed to understand the material's deformation characteristics. Any discrepancies or similarities between the findings of both papers will be discussed.

From the output file of the testing machine, the load can be derived from the .csv file by following steps.

Step i. convert the .csv file into .txt file using online tools or code on MATLAB.

Step ii: ii. Using Excel's Data From Text/CSV function, input the data in .txt file into excel. At this point the original data will be stored in a single column. If directly importing the .csv file into Excel, the converting function on Excel may lead to unexpected change on the laid data, making it hard to interpret.

Step iii: By using the "Text of Columns" feature under the Data tab, single column data can be divided into the desired data where one column contains one parameter. In the popup menu, choose the option "Delim-

ited". As the data is separated by space, select the space as the appropriate option. Preview the data in the "Data Preview" window to ensure it looks correct. Click "Next." Then the table is separated into the desired format.

Step iv: After splitting the data, as there's a dot after each load data, additional processing is needed to remove the dot. The following formula may be used.

$$= SUBSTITUTE(A1, ".", "", LEN(A1) - LEN(SUBSTITUTE(A1, ".", ""))) \tag{44}$$

Step v: Filter the data with only time with integers to be used in the further processing. Click on the drop-down arrow in the header of Column B. Unselect all options, then select "Number Filters" > "Equals..." In the "Custom AutoFilter" dialog that appears, enter 0000 as the criteria. After that, the required data can be filtered and ready for interpretation.

From the report page on GoM, the strain on x and y direction can be plotted with respect to time as .csv file. Copy the load data from the above-mentioned output table from testing machine into the GoM output file and rename as "LCFS (N)". By the code below, the time needed for photo capturing time(0.005s in this case) can be added to the time, aligning the timeline from the testing machine and GoM processing results. The code is shown in the appendix

iii Plot Interpolation
Interpolate the data from the machine to match the timeline with the DIC results. As it takes time for the camera to take every picture, to match the timeline, the time for the camera to take pictures needs to be added on the timeline using the code in the appendix. Then stress-strain curve of PEI under various temperatures can be visualized.

iv Deformation Visualization
DIC can also visualize the deformation process during DMA through video. By tracking the speckle patterns applied on the surface of the PEI samples, DIC can calculate the displacement and strain maps frame by frame. It enables the visualization of the deformation process with local strain concentration and viscoelastic behavior. After analyzing the images frame by frame, video visualization can be conducted using GoM software. By creating a report page using 3D video format with step settings, the whole deforming process can be seen in the video format giving a more intuitive approach for observing the results of DMA.

D. DMA Results

GoM successfully captured the deformation progress of the PEI specimen under temperature between 150 and 205 °C with 10 °C interval below 195 °C and 5 °C interval between 195 and 205 °C. Figure below shows one example of the deformation in both x and y direction captured by GoM. (DIC under other temperatures is shown in the appendix)

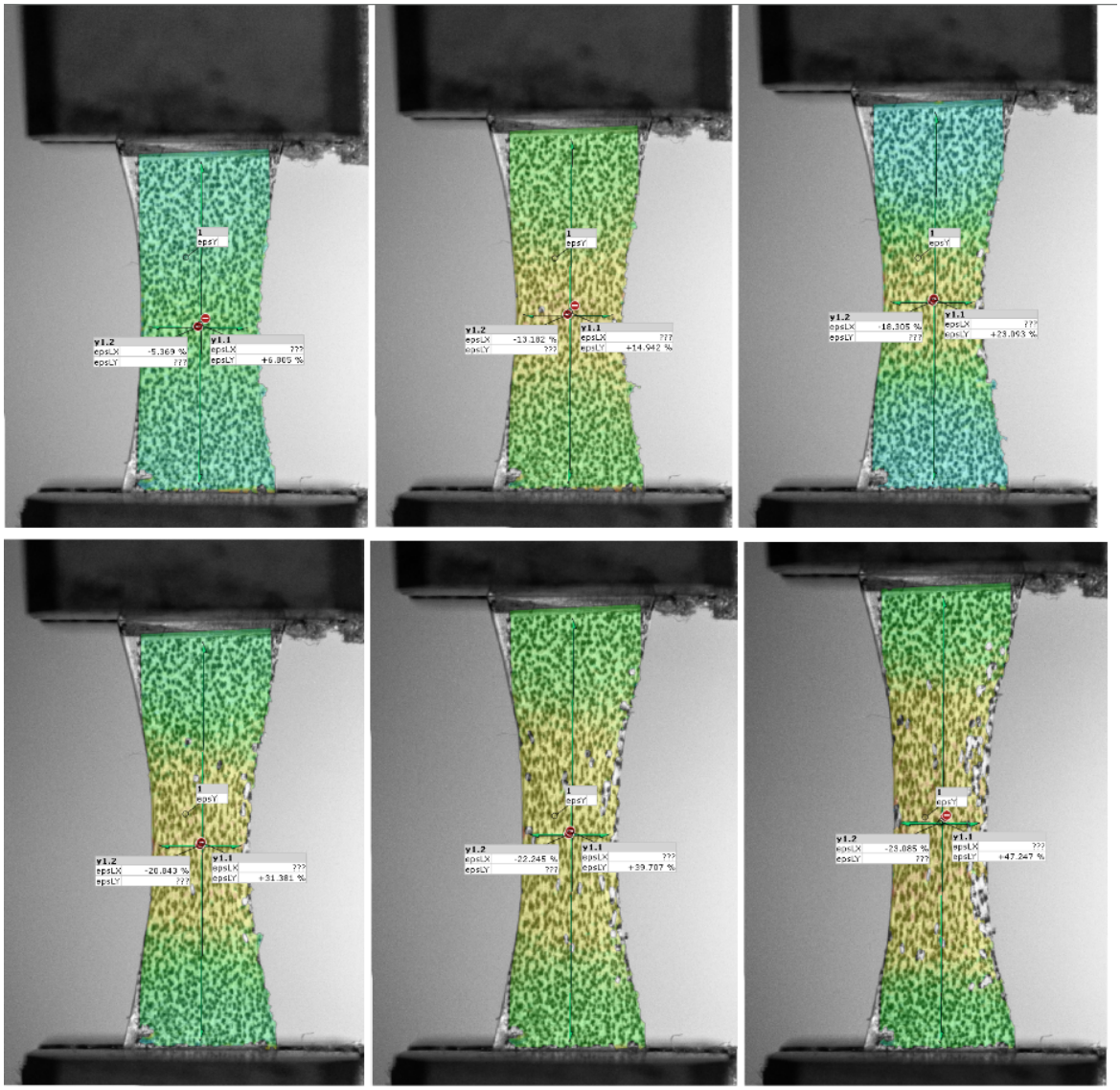

Fig. 35 DIC Results under 195 °C **with 6.25% strain difference between each other.**

The measured deformation in horizontal, vertical direction, stress, displacement and true strain in vertical direction under maximum temperature of 150 °C are reported in the table below, where t1 is the time, LCFS is the tensile force on the sample, epsLY is the extensometer in vertical direction from GoM, y is the true strain in the vertical direction, t is the measured thickness of the sample, w is the measured width of the sample, A is the area of cross-section of the sample, σ is the stress exerted on the sample.

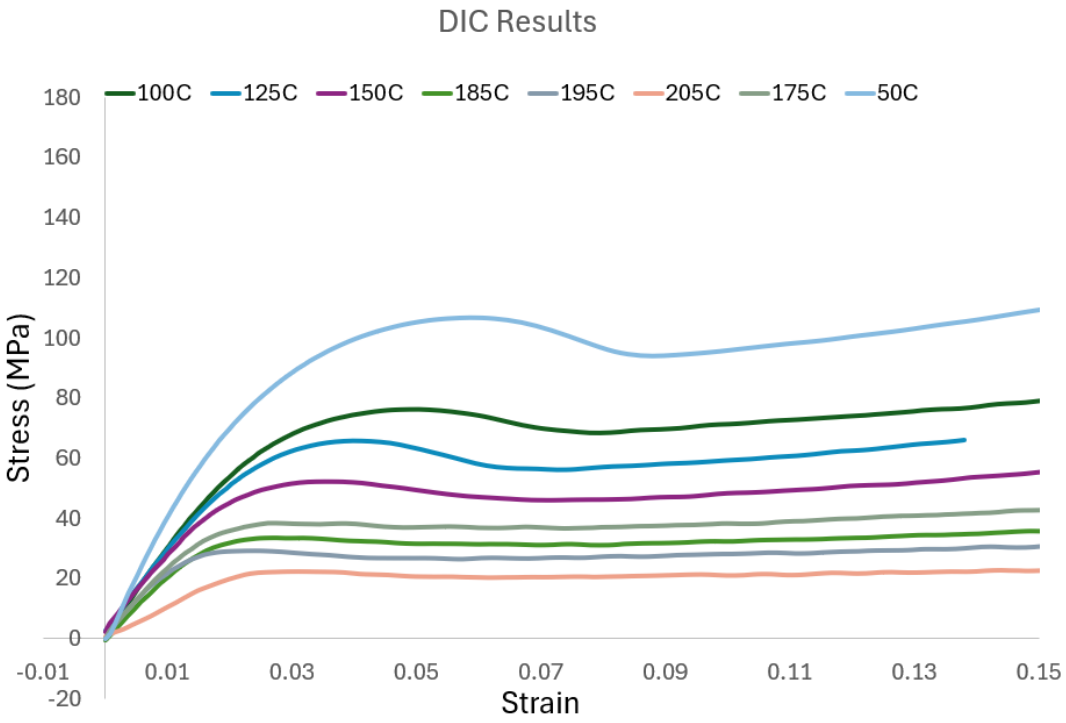

Fig. 36 Interpolated DIC Results.

t1 is the time, LCFS is the tensile force on the sample,epsLY is the extensometer in vertical direction from GoM, ϵ_y is the true strain in the vertical direction, t is the measured thickness of the sample, w is the measured width of the sample, A is the area of cross-section of the sample, σ is the stress exerted on the sample.

It can be found that at the beginning of the test, the nanofoam sample experience a primary creep where relatively high creep rate and linear behavior are observed. Then a relatively constant and steady-state deformation rate are observed when the strain accumulates more consistently with time with lower creep rate discovered, entering secondary creep. The sample experiences strain hardening in this process. With the stress provided in the test, tertiary creep was not observed.

To compare Young's modulus, the slope of the stress-strain curve under 1% of strain is considered. The relationship between Young's Modulus and time is shown in the figure below. It can be seen that Young's modulus experiences a relatively stable descent before foaming. However, Young's Modulus drops considerably faster during the forming process as the temperature approaches glass transition temperature..

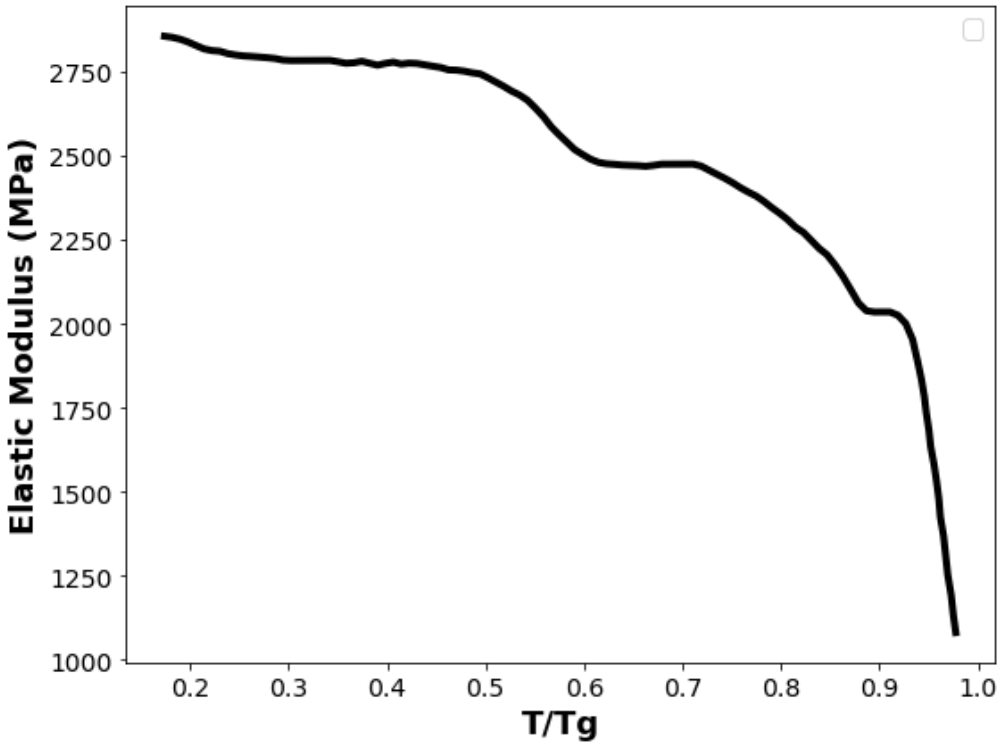

Fig. 37 Relationship between Young's Modulus and Temperature.

V. Modeling

The part illustrates the analysis of the testing results based on the DMA report and testing results, with attempt of curve fitting using the above-mentioned equations.

A. Ree-Eyring Fitting

The temperature dependence of molecular dynamics in polymers can be described by Eyring's flow theory at high temperatures as discussed in the literature review. As temperature decreases toward the glass transition, polymer behavior shifts to involve cooperative molecular motions. An intermediate regime involves simultaneous jumps of molecular units, bridging Eyring flow and glassy dynamics.[71]. In the simulation, as only temperature below glass transition is captured, the Young's Modulus-T/Tg relationship follows in fig 13. A simplified model using linear fitting is used as the relationship is considered linear around glass transition temperature between 175 C and 205 C. In the code, by adjusting values of exact activation energy and volume, initial strain rate and final strain rate, the predicted curve can be fitted with the experimental result of DMA with relatively high accuracy, as shown in the figure below. With calibrated Ree-Eyring values, modeling of the constitutive relationship can be executed more effectively and accurately.

The Results of the fitting are shown in the table below.

Table 2 Values of Variables after Fitting

Variable	Value
k_b	1.38×10^{-23}
v	5×10^{-27}
T_g	217
q	7.3×10^{-19}
$\dot{\varepsilon}_0$	1.5×10^{56}
$\dot{\varepsilon}_e$	0.006 25

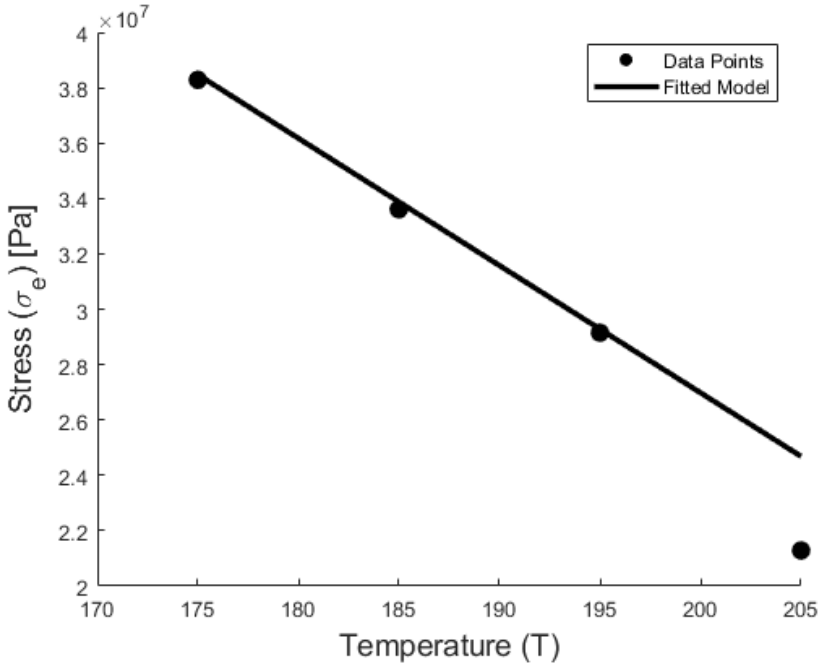

Fig. 38 Ree-Eyring Fitting Results.

B. Variable Flow

1. Temperature and Conservation Function

Heating is the primary reason causing subsequent behavior in stress, strain and cell growth. It starts and ends with given temperatures, but during the heating process it follows below calculations.

$$T(t) = T_{\text{low}} + \Delta T[r(t)] = T_{\text{low}} + (T_{\text{up}} - T_{\text{low}}) \left(1 - e^{-t/\tau}\right) \tag{45}$$

Starting from t=0, the rate at which it increases is set by the time constant τ. As time increases, the rise term also increases in exponential speed. This allows more simulation steps at temperature around the foaming temperature but save computational power at temperature prior to foaming. The larger the difference from the target, the faster the initial rate of change, but as it gets closer the rate slows down, giving the classic exponential approach to the new temperature.

The conservation of CO_2 serves as the fundamental for bubble expansion as it's closely related to how bubbles absorbs or dissipates gas molecules. Starting from conservation of internal bubble sizes, below formula are used for the dissolved-phase concentrations.

Let

$$a = x(1), \quad b_3 = a^3 - R_0^3 + b_0^3.$$

Then the internal bubble pressure $p(t)$ is computed by solving

$$(b_0^3 - R_0^3)C_0 + \frac{R_0^3 p_{g0}}{R_g T_{\text{low}}} = \frac{a^3}{R_g T(t)} p(t) + (b_3 - a^3)C(t),$$

with Henry's law $C(t) = K_H p(t)$. Rearranging gives:

$$p(t) = \frac{(b_0^3 - R_0^3)C_0 + \frac{R_0^3 p_{g0}}{R_g T_{\text{low}}}}{\frac{a^3}{R_g T(t)} + (b_3 - a^3)K_H}.$$

Finally, the dissolved-phase concentration is updated as

$$C(t) = K_H p(t).$$

2. Stress and Deformation Mapping

The calculation of stress involves using glass transition temperate, local temperature, strain rate and local strain. For each spatial mesh, the stretch in the radical direction can be calculated as

$$r_R = \left(1 + \frac{a^3 - R_0^3}{R_s^3}\right)^{1/3}, \tag{46}$$

where a refers to the bubble radius prior to foaming.

Stress and strain comes from the temperature and initial cell size. Then, logarithmic strain and strain rate can be calculated using mechanics of material formula before applying Ree-Eyring model.

$$\epsilon = 2\ln(r_R). \tag{47}$$

$$\dot{\epsilon} = \frac{2a^2\dot{a}}{R_s^3} r_R^{-3}, \tag{48}$$

where $\dot{(a)}$ is the current cell growth rate.

In Ree-Eyring model, temperature is normalized first like below.

$$\theta = \frac{T}{T_g} \tag{49}$$

Ree-Eyring stress and viscous stress can be derived from the constitutive equation. Plastic Stress:

$$\sigma_{\text{plastic}} = \frac{k_B \theta T_{g0}}{v} \, asinh\left(\frac{\dot{\varepsilon}}{\dot{\varepsilon}_0} \exp\left(\frac{Q}{k_B \theta T_{g0}}\right)\right) \tag{50}$$

Viscous Stress:

$$\sigma_{\text{viscous}} = 3\dot{\varepsilon}\eta_0 \exp\left(\frac{-\ln(10)C_1(\theta - 1)}{C_2/T_{g0} + (\theta - 1)}\right) \tag{51}$$

With the stress calculated, local force density can be found to allow cell expansion calculation.

$$f_{\text{int}}(s) = \frac{R_s^2}{r_R^3} \sigma(s) \tag{52}$$

3. Cell Growth

With conservation equation and stress equations, cell growth and its changing rate can be found. To compute $\dot{a}$, the code solves the equation:

$$(p - P_{\text{amb}}) - \int_{R_0}^{b_0} f_{\text{int}}(r)\, dr = 0 \tag{53}$$

where:

- p is the internal gas pressure,
- P_{amb} is ambient pressure,
- f_{int} is the internal force density as a function of radial position.

Internal Force Density:

$$f_{\text{int}}(r) = \frac{2}{r}\left(\left(1 + \frac{a^3 - R_0^3}{r^3}\right)^{1/3}\right)^{-3} \cdot \sigma \tag{54}$$

4. Pressure, Concentration and Porosity

Cell growth model is the main objective of the study, but pressure, concentration and porosity can also be found using this model to further validate the stress model and understanding the mechanism behind cell growth, allowing explanation from pressure perspective and study in macrosacles.

Concentration can be derived using Henry's gas law

$$c = K_H \cdot p \tag{55}$$

Where:

- K_H: Henry's law constant $[\text{mol}/(\text{m}^3 \cdot \text{Pa})]$
- p: pressure of gas inside the cell

The internal pressuere is calculated using gas mass balance and ideal gas law, which can be written as:

$$p = \frac{(b_0^3 - R_0^3)C_0 + \dfrac{R_0^3 p_{g0}}{R_g T_{\text{low}}}}{\dfrac{a^3}{R_g T} + (b^3 - a^3)K_H} \tag{56}$$

Where:

- $b^3 = a^3 - R_0^3 + b_0^3$ (volume of the outer shell)
- a: current cell radius
- R_g: universal gas constant
- T: current temperature
- C_0: initial concentration
- p_{g0}: initial pressure
- T_{low}: initial temperature (before heating)

Porosity refers to the volume fracture of gas inside the cell volume. It can be calculated as:

$$f = a^3/b^3 \tag{57}$$

To conclude, the logic flow of the simulation can be described in the following flow diagram.
The dependency of each variable can be seen from table below.

Variable	Computed by / Formula	Depends on	Feeds into
Simulation time	ODE Solver	—	Temperature Function
Temperature (Temp)	$T_{\text{low}} + (T_{\text{up}} - T_{\text{low}})\left(1 - e^{-\text{time}/\tau}\right)$	time, $T_{\text{low}}, T_{\text{up}}, \tau$	mass-balance for p, stress model
Pressure (p)	Initial and Final gas pressure	$a, R_0, b_0, C_0, p_{g0}, R_g, T_{\text{low}}, T$	c
Concentration (c)	$K_H\, p$	p	T_g Function
Glass Transition Temperature (Tg)	Tg_Function(T_{g0}, c, ρ_L)	T_{g0}, c, ρ_L	Stress Function
Cell Radius (a)	ODE Solver	initial a_0	Strains: $\epsilon, \dot{\epsilon}$
Cell Growth Rate ($\dot{a}$)	$(p - P_{\text{amb}}) - \int f_{\text{int}}\, dR = 0$	Stress Function, Pressure	N/A
Bubble Radius (r_R)	$\left(1 + (a^3 - R_0^3)/R_s^3\right)^{1/3}$	a, R_0, R_s	$\epsilon, \dot{\epsilon}, f_{\text{int}}$
Strain (ϵ)	$2\ln(r_R)$	r_R	Stress Function
Strain Rate ($\dot{\epsilon}$)	$2\,a^2\,\dot{a}/R_s^3\;\; r_R^{-3}$	$a, \dot{a}, R_s, r_R$	Stress Function
Plastic Stress (σ_{plastic})	Ree–Eyring formula	$k_B, T, T_{g0}, v, \dot{\epsilon}, Q$	Stress Function
Viscous Stress (σ_{viscous})	Viscous-flow formula	$\dot{\epsilon}, \eta_0, C_1, C_2, T, Tg$	stress Function
Stress (σ)	Min plastic or viscous Stress	$\sigma_{\text{plastic}}, \sigma_{\text{viscous}}, T, Tg$	f_{int}

The flow can be simplified as below.

$$\text{Time} \xrightarrow{\text{Temperature Function}} \text{Temperature} \xrightarrow{\text{Mass Conservation}} p \xrightarrow{c=K_H p} c \xrightarrow{\text{Glass Transition}} Tg \xrightarrow{\text{Stress Function}} \sigma$$

$$(a, \dot{a}, R_s) \;\rightarrow\; r_R \;\rightarrow\; (\epsilon, \dot{\epsilon}) \;\rightarrow\; \text{Stress Function} \;\rightarrow\; \sigma \;\rightarrow\; f_{\text{int}}(s) \;\rightarrow\; \text{Porosity}$$

C. Modeling using MATLAB

The mesh set discretizes the spatial domain for solving the equations governing the foaming process of a PEI with CO_2. It allows the program to compute physical properties such as cell radius, stress, and gas concentration at discrete points. In this simulation, 1000 mesh points is considered as a balance between calculation accuracy and calculation difficulty.

In Matlab, ode45 uses Runge-Kutta Method to solve the non-stiff ODEs, which suits the need of PEI samples in DMA testing. It is designed to provide a good balance between accuracy and computational efficiency for non-stiff ODEs. It automatically adjusts the step size to meet the specified error tolerances by RelTol and AbsTol, which can be set depending on various temperatures. This helps maintain high accuracy in the simulation results. At the same time, ode45 uses an adaptive step size to efficiently handle regions where the solution changes rapidly or slowly. This feature is particularly useful in this simulation by automatically altering the steps size based on the changing rate of the parameters.

D. Code Structure

The MATLAB code for the constitutive model can be constructed to describe the evolution of PEI system where nucleation, bubble growth and expansion, stress, glass transition behave under given strain rate and initial temperature. It involves a set of ODE to represent the dynamics of gas bubble growing in viscoelastic cases. It incorporates a series

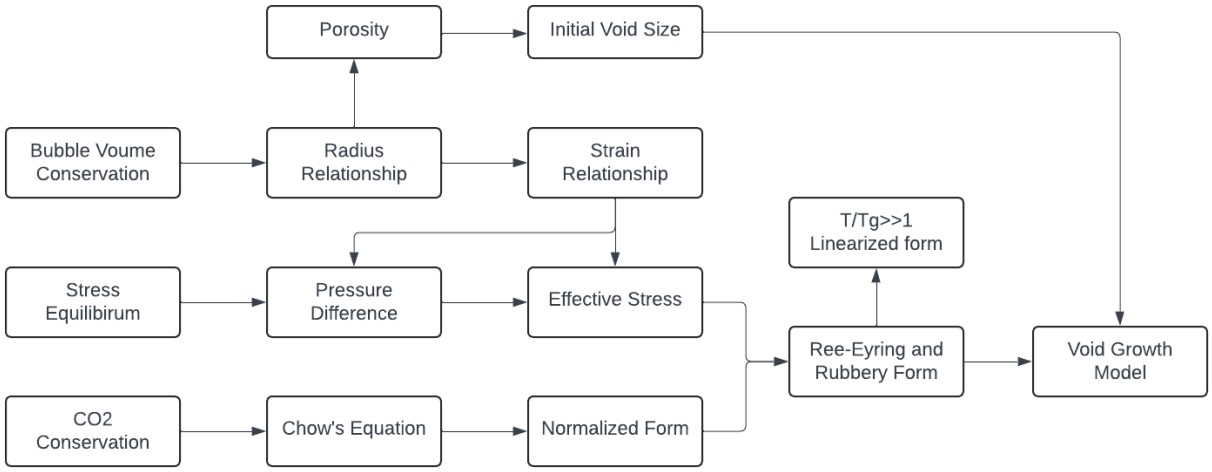

Fig. 39 Flow of PEI Modeling on MATLAB.

of thermodynamics parameters, pressure and concentration changes which influence the glass transition behavior of PEI samples, and this part will give a detailed breakdown of the code.

First, global variables including material properties, thermodynamic properties, simulation time and accuracy are declared. These global variables facilitate sharing data among different functions (including ODE solvers and auxiliary functions) without having to pass numerous parameters explicitly. Then physical parameters including nucleation density, pressure and surface tension are set to construct the initial foaming conditions. Some of the parameters tend to influence the bubble growth which will be covered in later parametric study sections. Time discretization is performed by defining span (using a linear space) over a total duration with a fine resolution (1000). In parallel, a logarithmically spaced spatial mesh is created between the initial bubble radius and the spacing parameter b0. Finer mesh may lead to higher accuracy with similar time steps, but it will make the calculation of each step longer. While higher tolerance can increase the accuracy by controlling better time steps, if it goes too high, it may get stuck at some noise point by repeatedly calculating the values under very small time intervals which will harm simulation efficiency.

The ODE solver function governs the temporal evolution of key system variables. The primary variable x(1) represents the bubble radius a. The function computes auxiliary parameters such as pressure, gas concentration, and temperature, which influence the system dynamics using the constitutive equation and strain relationship discussed earlier to formulate the concentration model. To solve the ODE, ode15s solver is used, which is considered as an optimal choice for better stiffness handling using variable-step, variable-order solver. High precision of 1e-16 is used to ensure computational accuracy.

Besides the main ODE solver function, a few helping functions are also created using given stress-strain relationships. First, a temperature profile is established to model the transition of temperature over time accounting for variations in the glass transition temperature (Tg) due to gas concentration changes. Then, Ree-Eyring relationship is used for plastic and viscous components for the relationship between stress and temperature effects under a given time step making it possible to establish stress equilibrium cases. With stress equilibrium cases, local stress can be integrated. For bubble radius calculations, integral over the mesh is executed using local strain and strain rate based on the current bubble radius and a reference radius. With these information cell growth model of PEI. After calculation, plots are made to visualize the relationship between stress, cell growth, porosity, concentration against time and temperature profile.

E. Simulation Results

Using the previously described code, both stress evolution and cell growth behavior can be accurately captured under pressures of 1 MPa and 5 MPa. The plotted results indicate that as temperature increases, the foaming rate accelerates, leading to faster cell growth and a reduced time to reach equilibrium. In terms of stress response, higher temperatures result in a more rapid increase in stress and a shorter time for both stress and the glass transition temperature to stabilize. When the pressure is reduced from 5 MPa to 1 MPa, the reduced constraints on the cells lead to significantly larger cell sizes, with growth rates increasing from approximately 50 nm to 45 μm . Additionally, the lower pressure slows heat absorption, which in turn leads to a slower decrease in concentration and a more gradual increase in stress before reaching equilibrium. The figures below illustrate the influence of temperature and pressure on the constitutive behavior of PEI.

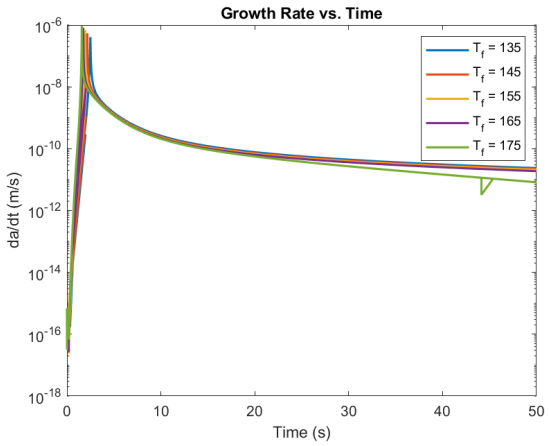

(a) Growth Rate vs Time

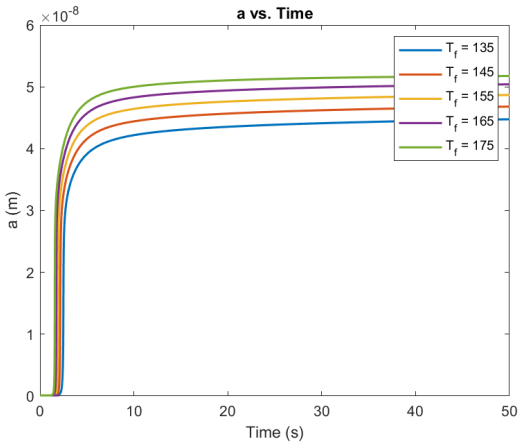

(b) Cell Radius vs Time

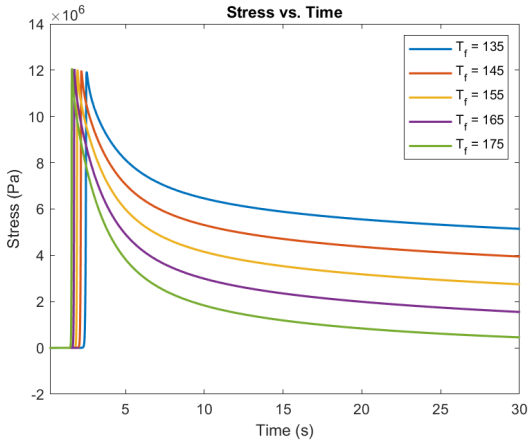

(c) Stress vs Time

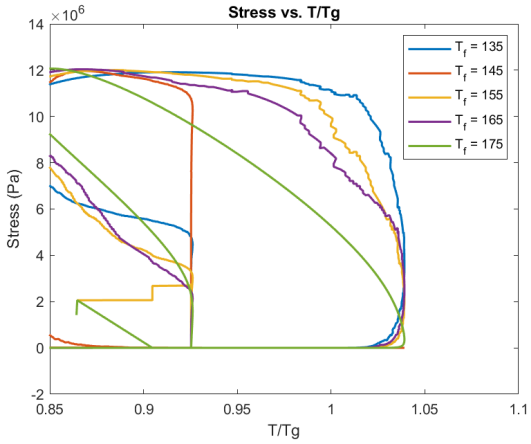

(d) Stress vs T/T_g

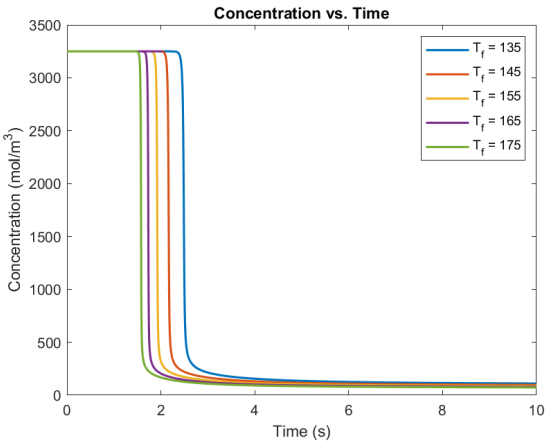

(e) Concentration vs Time

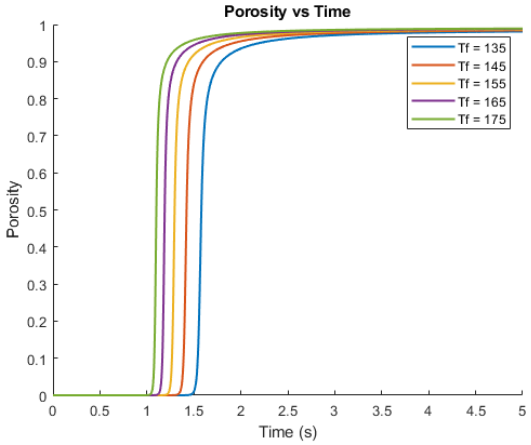

(f) Porosity vs Time

Fig. 40 Response of the Constitutive Model under 5 MPa

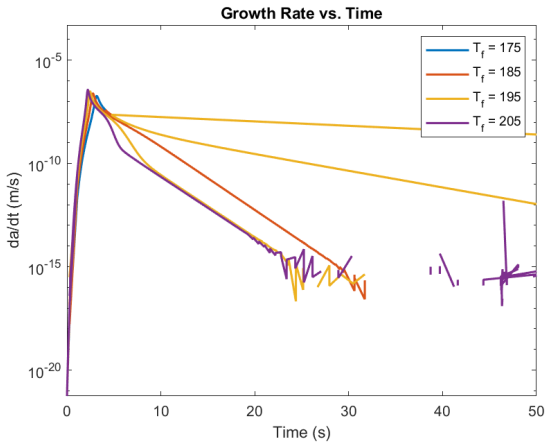

(a) Growth Rate vs Time

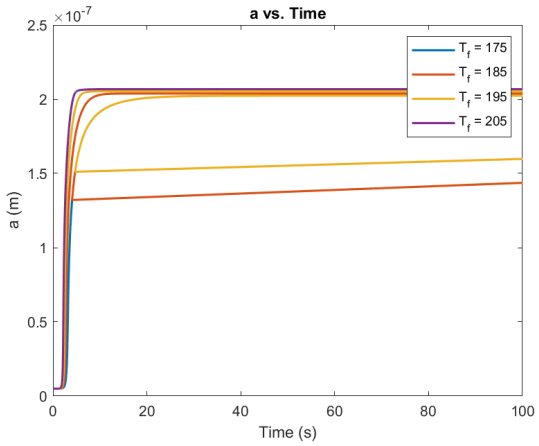

(b) Cell Radius vs Time

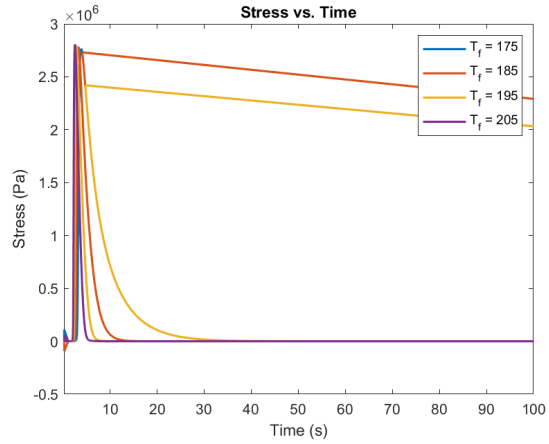

(c) Stress vs Time

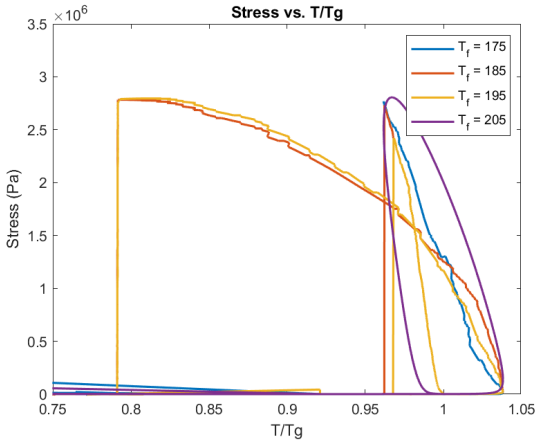

(d) Stress vs T/T_g

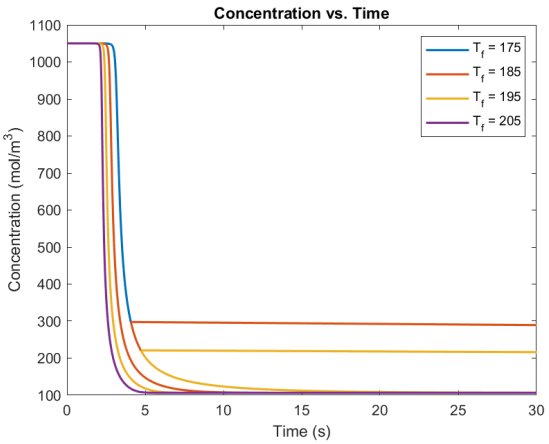

(e) Concentration vs Time

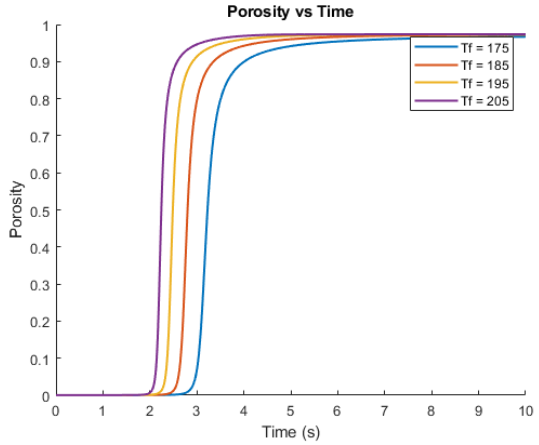

(f) Porosity vs Time

Fig. 41 Response of the Constitutive Model under 1 MPa

With the simulation results, the relationship between foaming temperature and cell radius can be plotted as shown below, which follows a relatively linear pattern in each regime.

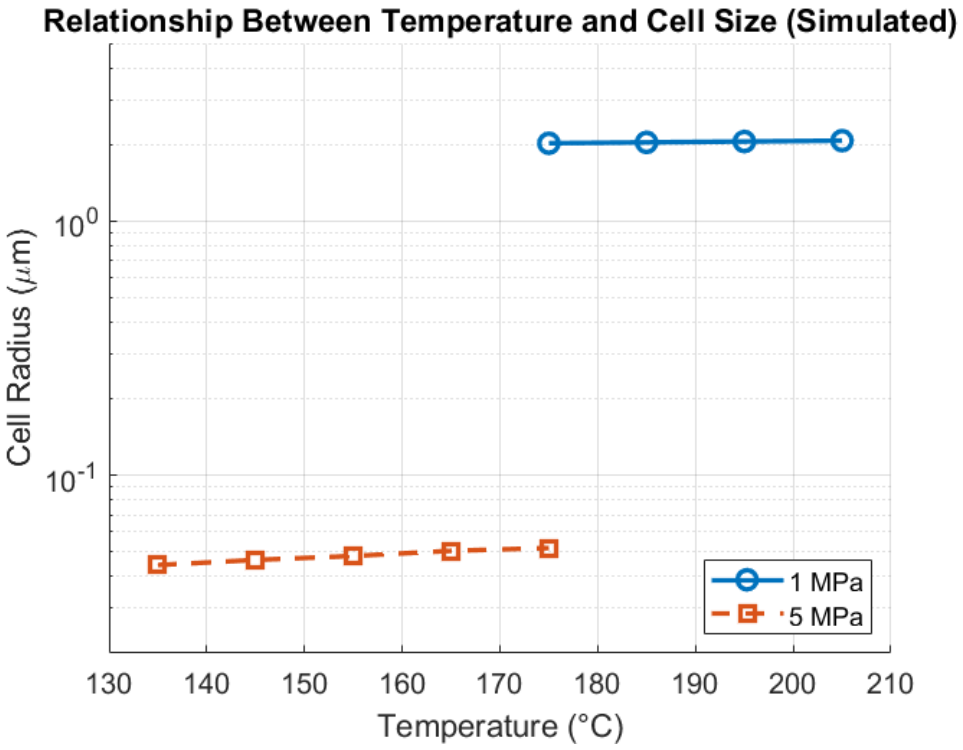

Fig. 42 Relationship between Cell Radius and Foaming Temperature under 1MPa and 5MPa

F. Parametric Study

The effects of some of the parameters can be concluded as follows by conducting parametric study. By studying the effect of how variables affect the cell growth model, tailored made material can be developed with best suit of design requirements and cost goals by optimizing saturation process, tailoring nucleation and forging processes.

1. Nucleation number (N_0):

Nucleation number refers to the number of gas nucleation sites per unit volume in the foaming process. It tends to influence cell density, cell size and foam cell distribution. Manufacture process of PEI samples can influence the nucleation number by stress, both in elongation and shear.[71] Higher N_0 slightly reduces the temperature possibly due to increased energy absorption, but it also consumes more gas, leading to earlier drop of concentration. At the same time, higher N_0 produces smaller but more homogeneous cell size which may results in lower cell growth rate and eventually leads to smaller cell sizes. The effect of N_0 is shown in the figures below

2. Initial strain rate ($\dot{\varepsilon}_0$)

Initial strain rate tends to affect the viscoelastic behavior during foaming which affects temperature. It also influences nucleation of bubbles, with higher initial strain rate leading to faster gas diffusion and lower stability. Lower initial strain rate can allow PEI to release stress over time reducing likelihood of defects. As a result, when initial strain rate increases, peak stress tends to decrease and takes a shorter time to reach equilibrium, while T/Tg decreases at the same time, shifting stress vs T/Tg curve to the left. The effect of $\dot{\varepsilon}_0$ is shown in the figures below

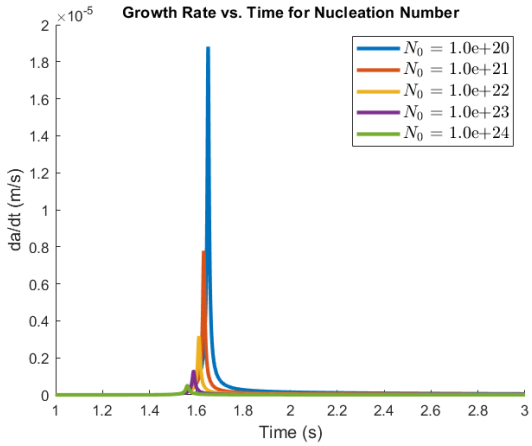

(a) Growth Rate vs Time

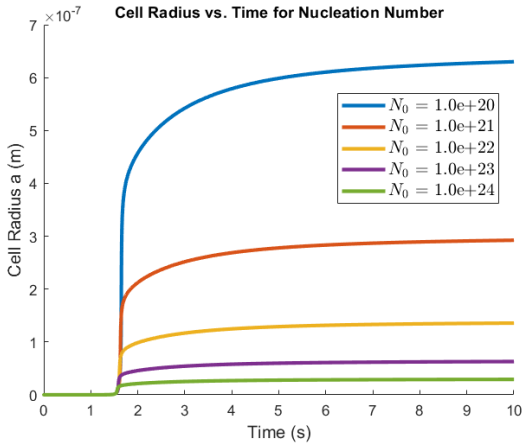

(b) Cell Radius vs Time

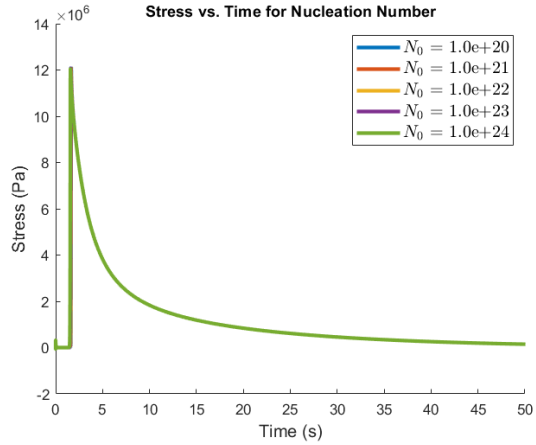

(c) Stress vs Time

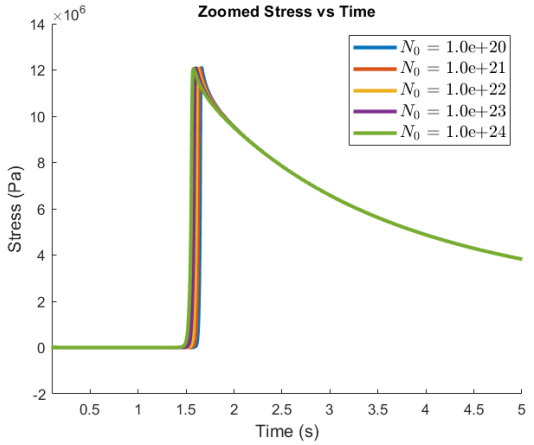

(d) Zoomed Stress vs Time

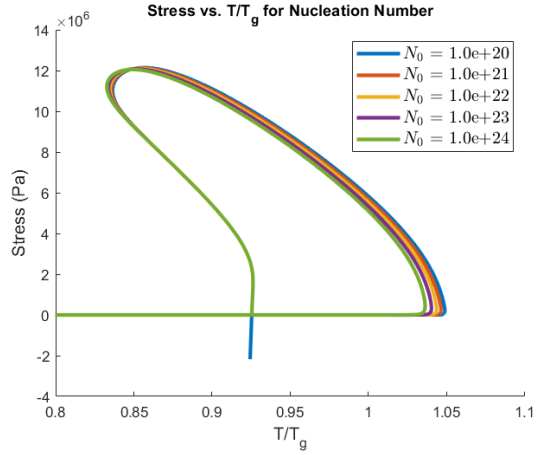

(e) Stress vs T/Tg

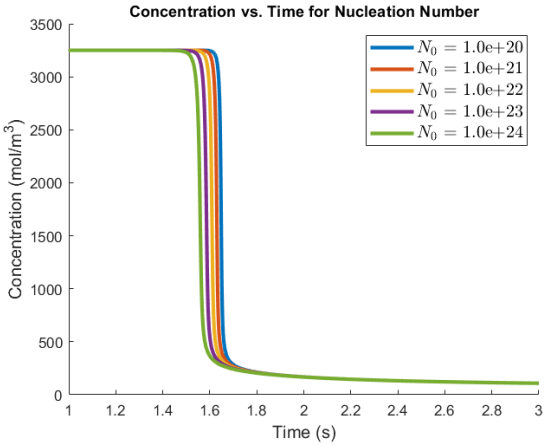

(f) Concentration vs Time

Fig. 43 Effect of Nucleation Number on the Model under 195C and 5MPa

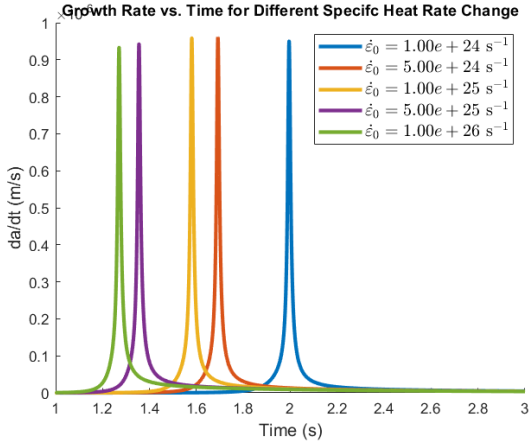

(a) Growth Rate vs Time

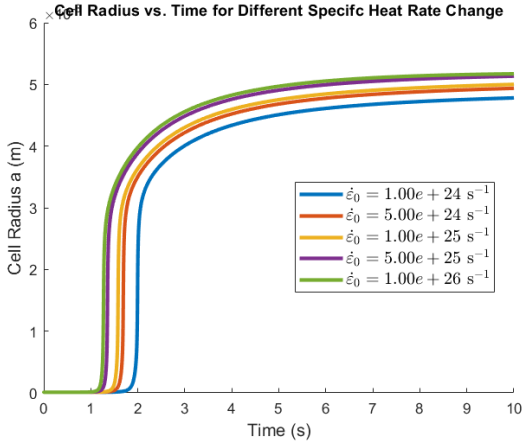

(b) Cell Radius vs Time

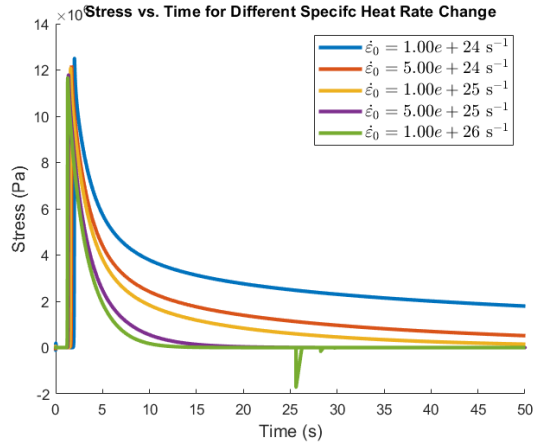

(c) Stress vs Time

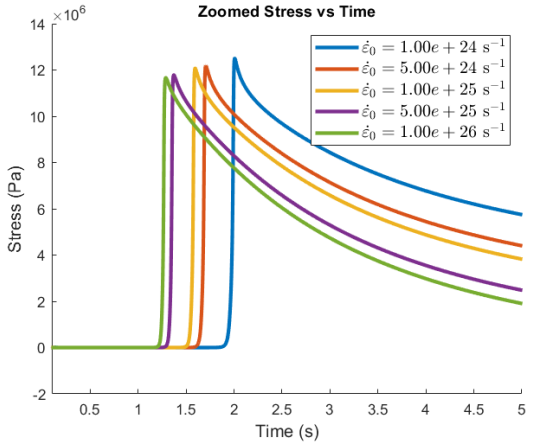

(d) Zoomed Stress vs Time

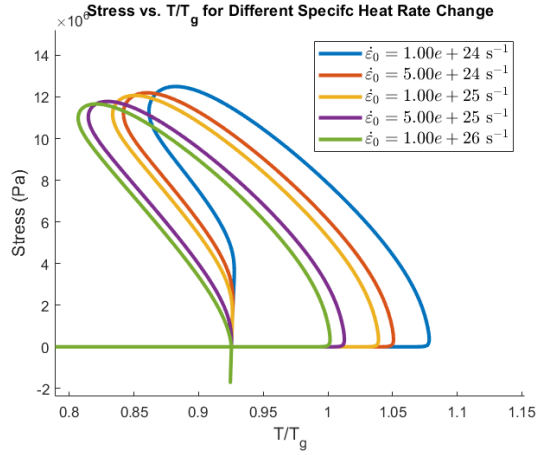

(e) Stress vs T/Tg

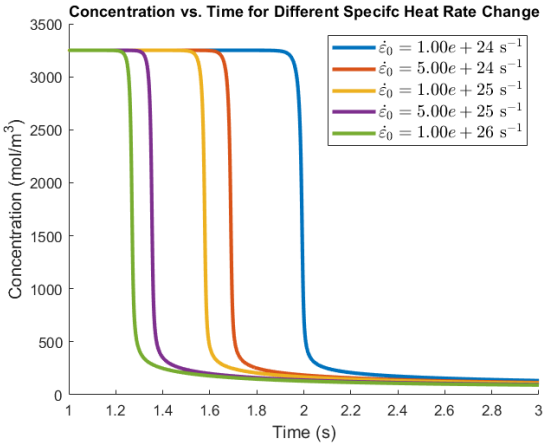

(f) Concentration vs Time

Fig. 44 Effect of Initial Strain Rate on the Model under 195C and 5MPa

3. Specific Heat Change (ΔC_p)

ΔC_p is used to describe the change in Cp between the rubbery and glassy states, which will have direct effects on T/Tg and influence concentration indirectly by changing gas dissolve during foaming. The higher specific heat change is, the slower the temperature increases during foaming leading to delay of foaming. This also leads to delay in drop of concentration when PEI has higher change in specific heat capacity. Due to the shorter time to absorb heat, PEI with lower change of specific heat also displays lower but earlier growth rate during bubble growth as shown in the graph below. The effect of ΔC_p is shown in the figures below

4. Lattice Coordination Number

z describe the number of nerighboring cells in the polymer structure, thus giving a considerable effect on the bubble growth process during foaming. When lattice coordination number is high, local restraints grow and introduce a high nucleation energy barrier, making it harder for bubble formation. At the early stage of cell growth, a higher z the entropy cost for forming a cavity due to the loss of configurational freedom of surrounding lattice sites which is not favoured by cell growth. As a result, z mainly affects the cell growth process with the effect on stress can be neglected.

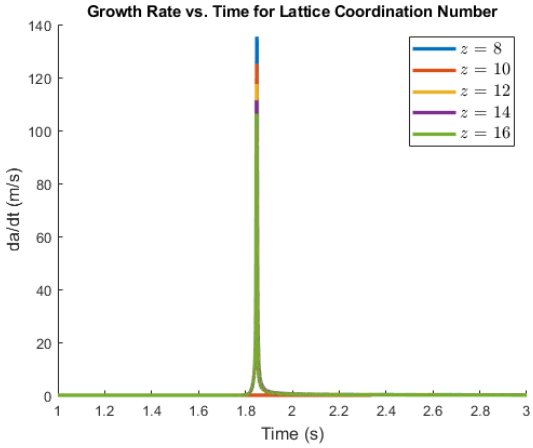

(a) Growth Rate vs Time

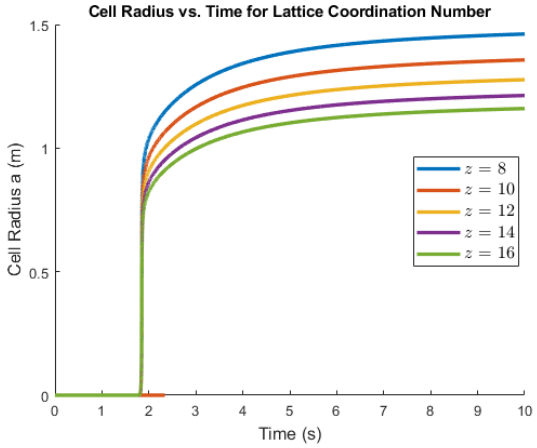

(b) Cell Radius vs Time

5. Viscosity and other Tuning Parameters (η_0, C_1, C_2)

Viscosity is highly dependent on temperature and shear rate rather than just the initial viscosity value during foaming. As the polymer heats up, viscosity decreases exponentially, meaning that any small difference and viscosity becomes negligible.

Although $C_1 and C_2$ may contribute to fine tuning of the PMMA model, PEI model shows they are more likely to be overshadowed by other parameters which makes their effect relatively minor.

To conclude, glass transition temperature depends highly on heat absorption which is related to change in heat capacity and initial strain rate closely, change in specific heat capacity in particular. Stress is more related on the strain initial conditions which is reflected on initial strain rate, although other factors may also have minor contributions. Similar behavior is also observed when PEI samples are treated under 1 MPa saturation with the figures shown in the appendix.

VI. Model Validation

The constitutive model of PEI under CO_2 saturation can be validated in both DIC and cell growth model. The way of validation is shown in this section.

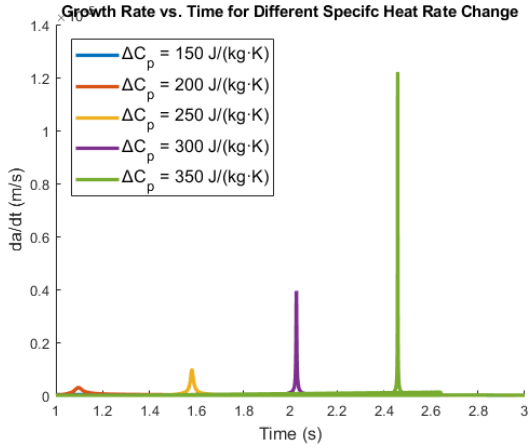

(a) Growth Rate vs Time

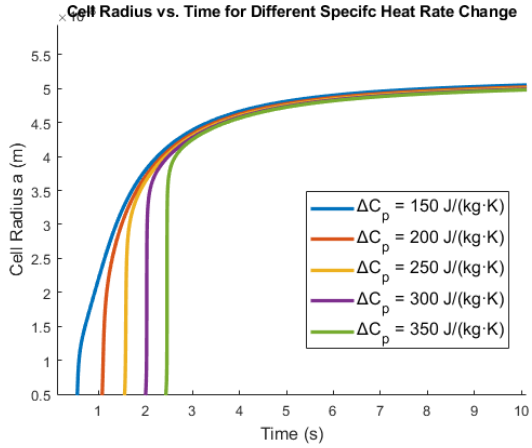

(b) Cell Radius vs Time

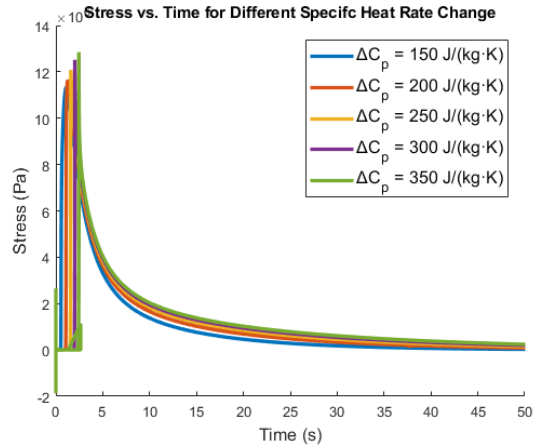

(c) Stress vs Time

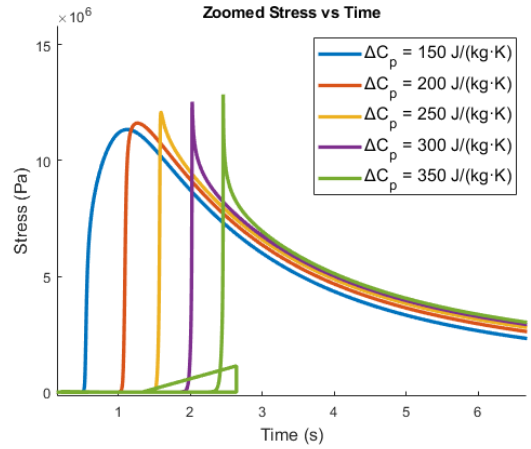

(d) Zoomed Stress vs Time

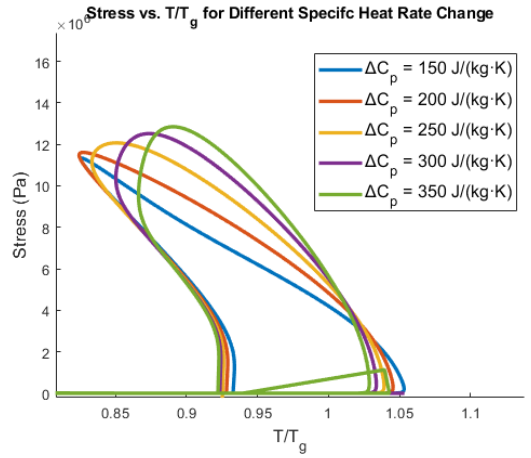

(e) Stress vs T/Tg

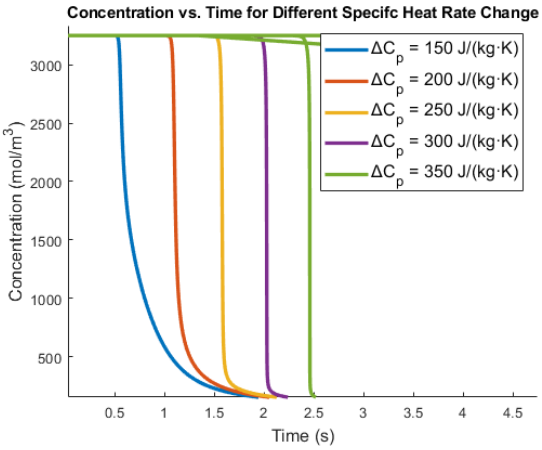

(f) Concentration vs Time

Fig. 45 Effect of Change of Specific Heat on the Model under 195C and 5MPa

A. DIC Results

In DMA, the machine recorded the load and displacement of the mount which can be used to calculate the true stress and strain of the sample. By comparing DIC results and data from DMA machine, the results of the DIC can be validated which inclines with the DMA results.

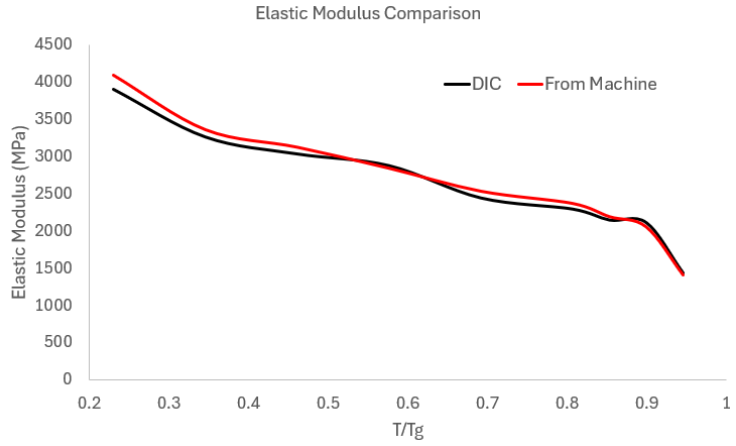

Fig. 47 Validation of Elastic Modulus

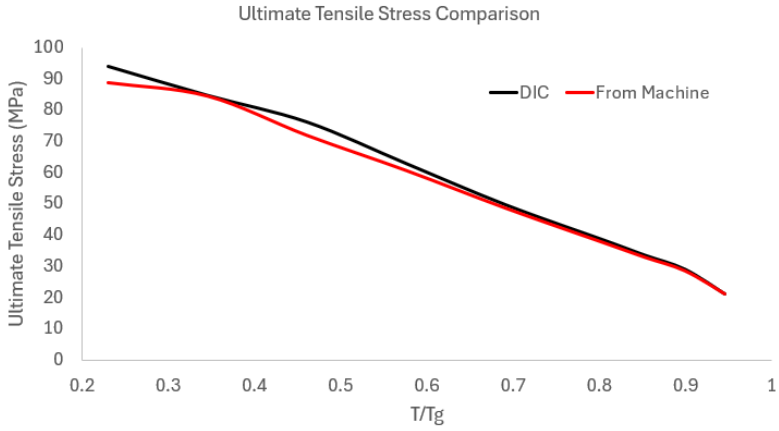

Fig. 48 Validation of Ultimate Stress

B. Cell Size

Scanning Electron Microscopy (SEM) is an imaging technique which applies electron beams to scan a surface of specimen to produce images of sample's surface topography and composition. SEM can provide magnification of 1,000,000x and resolutions in nanoscale, making it a powerful tool in examining the cell structures of PEI after foaming. The level of resolution is critical for capturing cell growth to validate the computational cell growth model.

To quantitatively analyze SEM images for cell size validation, proper measurement software is needed. ImageJ is a open-source image-processing software. It begins by importing SEM images into ImageJ and converting to greyscale with enhanced contrast to improve the measurement accuracy. Then, calibration is made to ensure the scale using scale bar from SEM image. Then, thresholding is used to distinguish the cells from the background converting the images to binary format. To avoid confusion of overlapping cells, algorithm is used to distinguish specific cell boundaries. Finally, "Analyze Particles" function is used to meaure the cell parameters. The flow diagram is shown in the figure below.

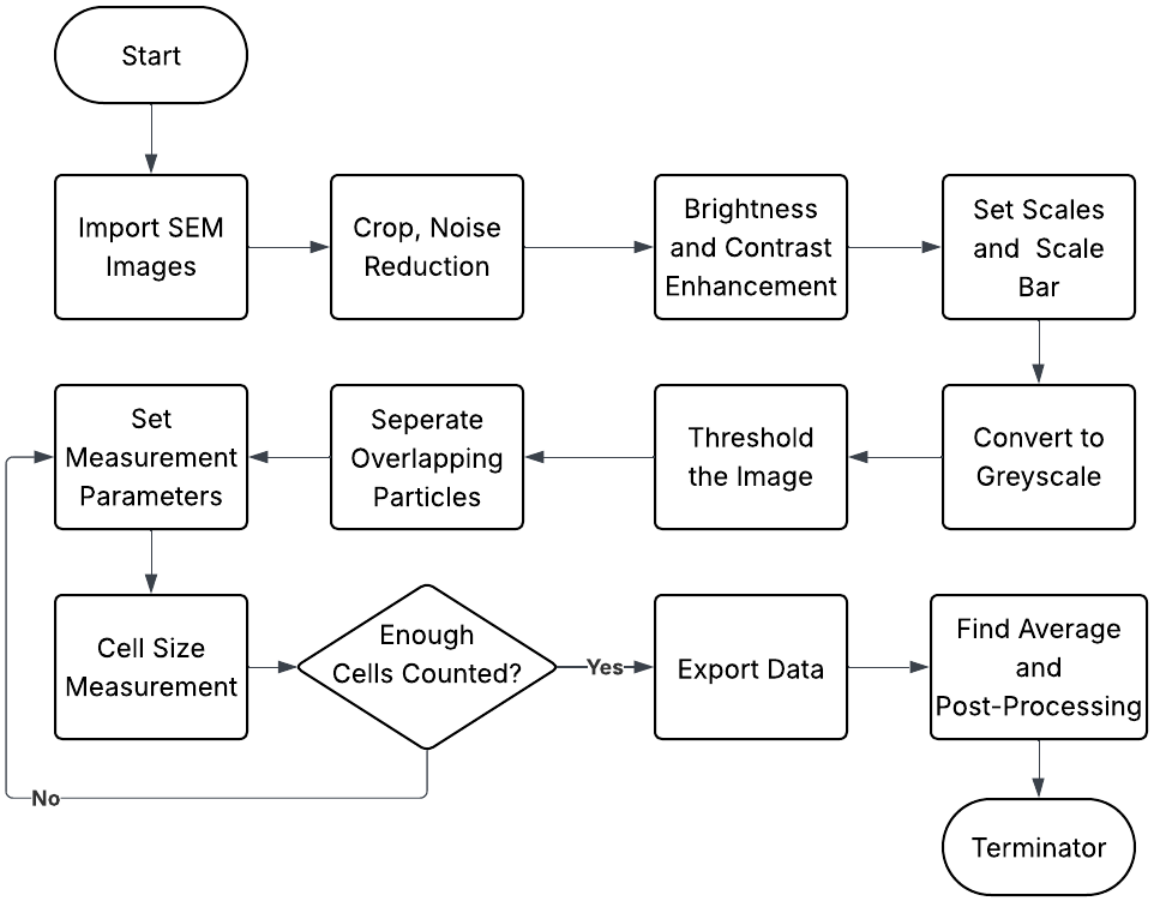

Fig. 49 Flow Diagram of Using ImageJ to Analyze Cell Sizes

By using SEM on the samples after DMA to measure the size of the cells, the cell growth model can be fine-tuned and validated. Below pictures shows the SEM results of the samples.

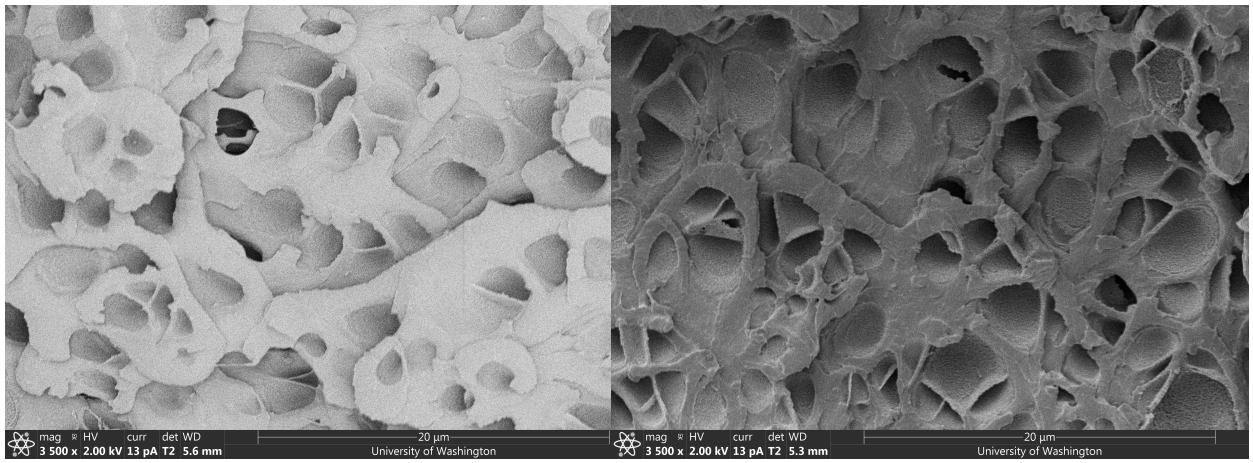

(a) 175°**C** **(b)** 185°**C**

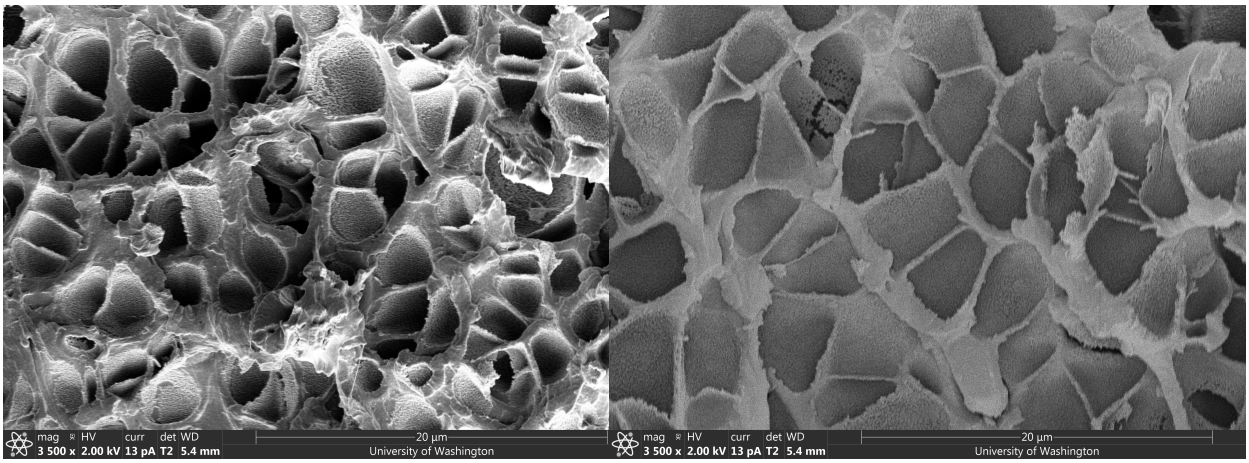

(c) 195°**C** **(d)** 205°**C**

Fig. 50 SEM of Samples under Temperatures between 175 and 205 °C under 1 MPa

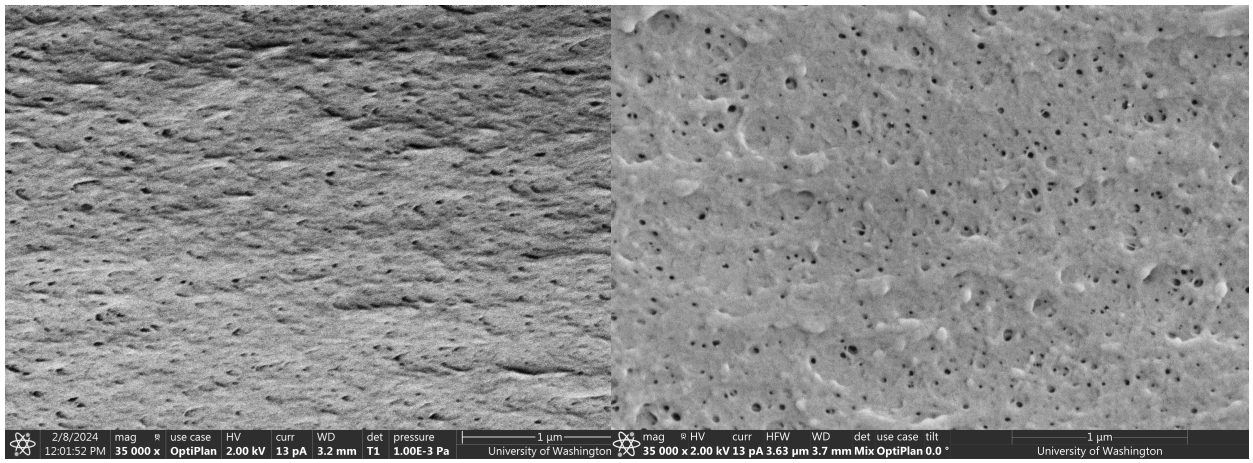

(a) 135°**C** **(b)** 145°**C**

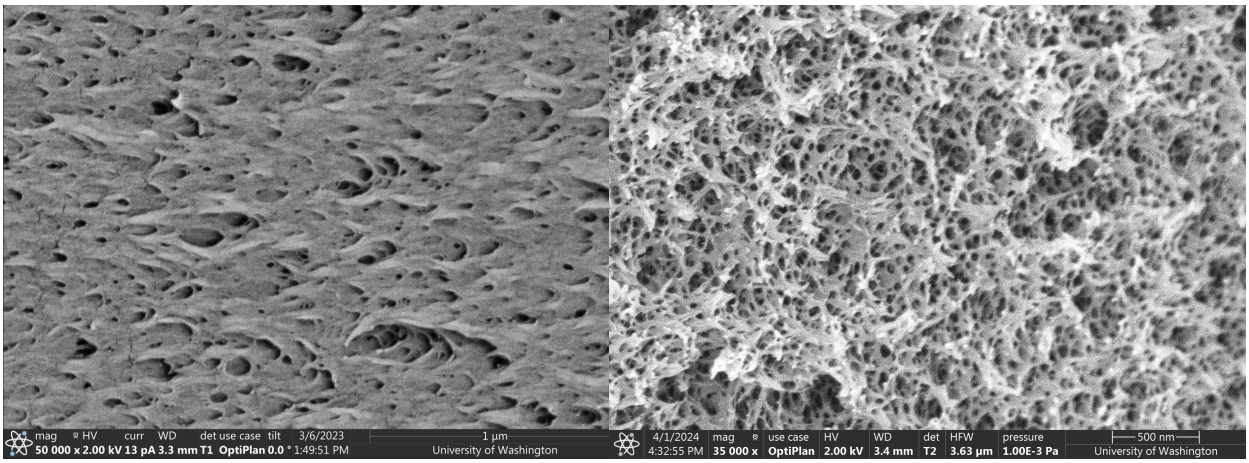

(c) 165°**C** **(d)** 175°**C (unit length: 500nm)**

Fig. 51 SEM of Samples under Temperatures between 135 and 175 °C under 5 MPa (unit length: 1 μm unless specified)

By taking the average of these cell sizes, the relationship between foaming temperature and average cell size of PEI samples can be plotted in the figure below, which inclines with the output from the constitutive equation derived in the MATLAB model.

After increasing contrast and removing overlapped cells, the processed SEM image before measuring looks like below.

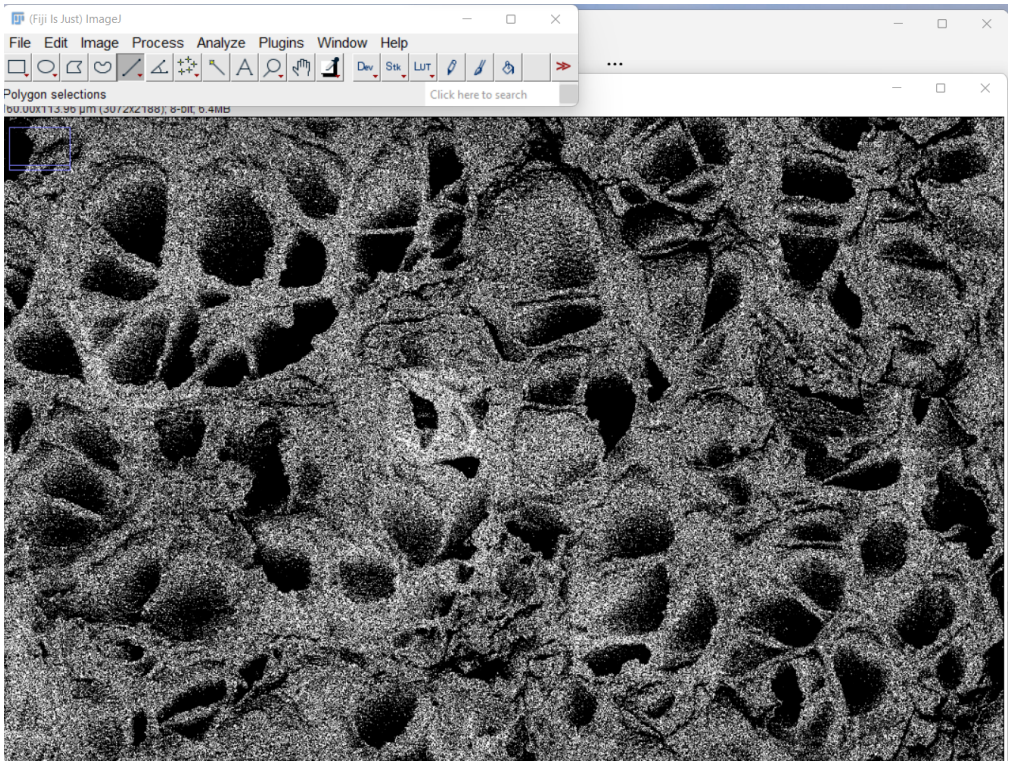

Fig. 52 Processed SEM Image before Measurement

The measured cell results from the SEM are as follows. It can be seen when compared to simulated results, the simulated cell radius aligns with the measured results, proving relatively high accuracy of the growth model under various foaming temperature and CO_2 saturation pressure.

Table 3 Predicted vs Measured Values at 1 MPa and 5 MPa

1 MPa			5 MPa		
Temperature (°C)	Predicted (μm)	Measured (μm)	Temperature (°C)	Predicted (nm)	Measured (nm)
175	2.022	2.0	135	44.4	25.0
185	2.038	2.1	145	46.5	46.5
195	2.054	2.5	165	50.5	48.0
205	2.070	3.0	175	51.8	51.0

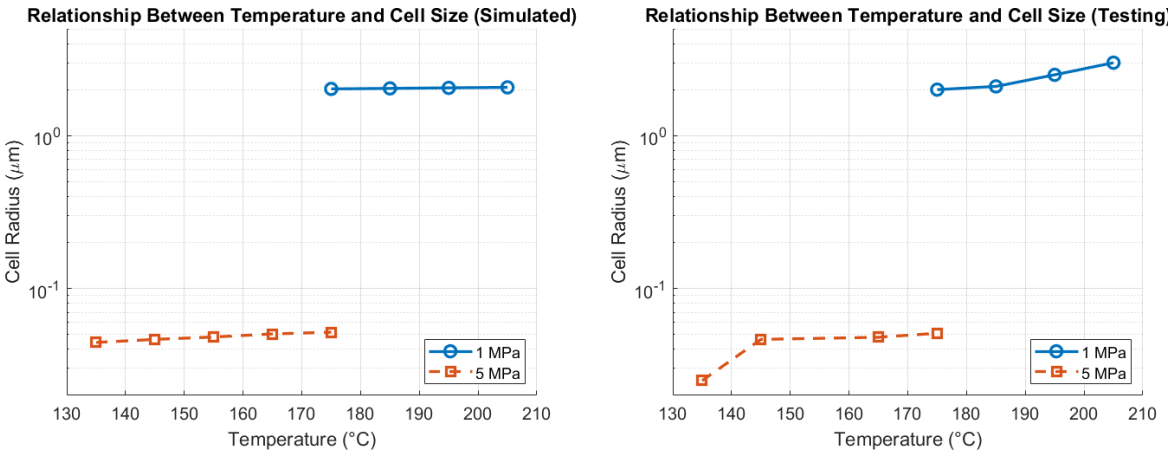

(a) Radius from Simulation **(b) Radius from Testing**

Fig. 53 Comparison between Simulated and Measured Radius

VII. Discussion

A. DMA Discussion

From the experiment to the data interpretation, there might be some point which needs extra attention to ensure the quality of the data and minimize testing errors as follows.

1. During polishing, two possible ways to determine if the surface is smooth enough ready for testing. (i). Examine the specimen under the microscope, a relatively good sample displays very few or no white dots on the surface while the relatively rough ones display some white dots or lines on the surface. (ii). The relatively smooth surface tends to be transparent, while rough ones may look blurred.

2. The camera needs to be mounted firmly by appropriate supporting structures to avoid shaking, which may affect the surface component creation quality on GoM, which tends to plot discontinuous curves. To minimize it, manually focus the camera by enlarging the testing sample to make sure the picture is clear.

3. Slipping of the specimen may contribute to measurement errors or possible backing of the specimen,as shown in the figure below. Slipping can be observed visually by the slipping lines on the sample surface during the testing or after testing.

   To minimize it, avoid dust and rough surfaces on the specimen's surface and double check the clamping before starting the machine before start testing. Before the testing, longer samples may provide longer grip length which may also contribute to less slipping. During the test, filing the sample clamping surface with 400 sandpaper or slightly increase the ramp length may minimize the slipping as well and makes it easier for slipping to be observed at an relatively earlier stage of the test.

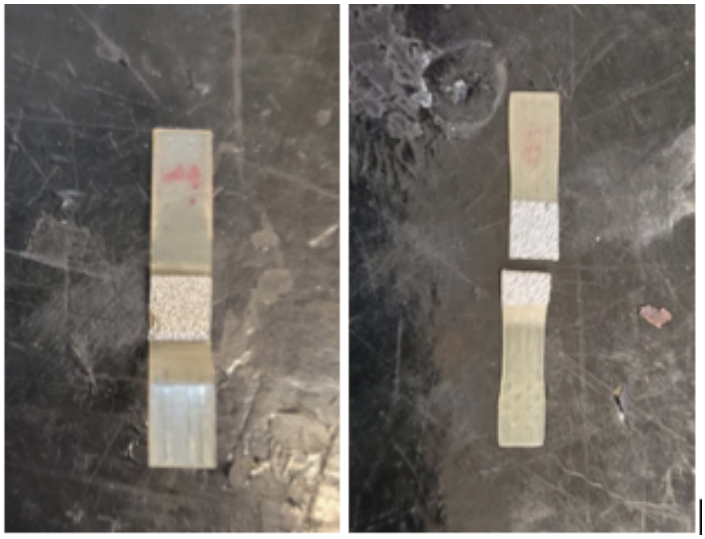

Fig. 54 Two possible failure patterns due to slipping

4. Failure modes of the samples. The cracks on sample 3, 4, 5, 6 a located in the middle region of the specimen, which indicates the validity of the testing. Sample 2 experienced slipping during the testing.

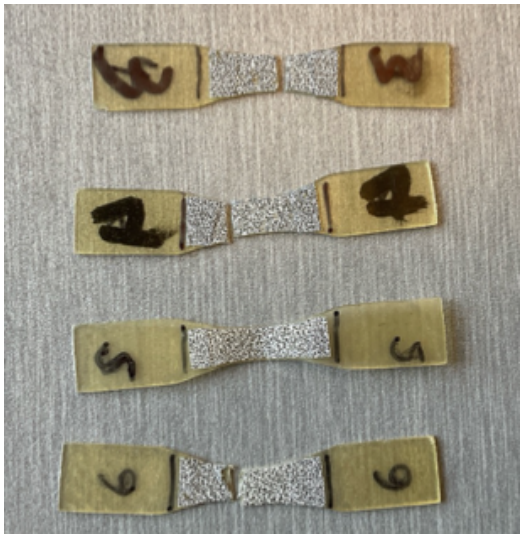

Fig. 55 Failure Mode of Successful Samples

B. DIC Considerations

1. Facet Size Settings

Facet size refers to the dimension of the square areas analyzed during DIC. Larger facets enhance the stability of tracking during deformation but may reduce the ability to detect fine material behaviors. Conversely, smaller facets improve spatial resolution but might be less stable in tracking. Point distance refers to the spacing between two adjacent facets. A smaller distance distance allows facet points with higher density which benefits the accuracy of the deformation calculation. However, it also leads to higher computational requirement and lower tolerance. Lower torlerance may lead to incomplete coverage of the whole sample body. The effect of different facet setting and point distance are shown in the below figures. Finally, the software starts automatically calculate the image data throughout the timeline.

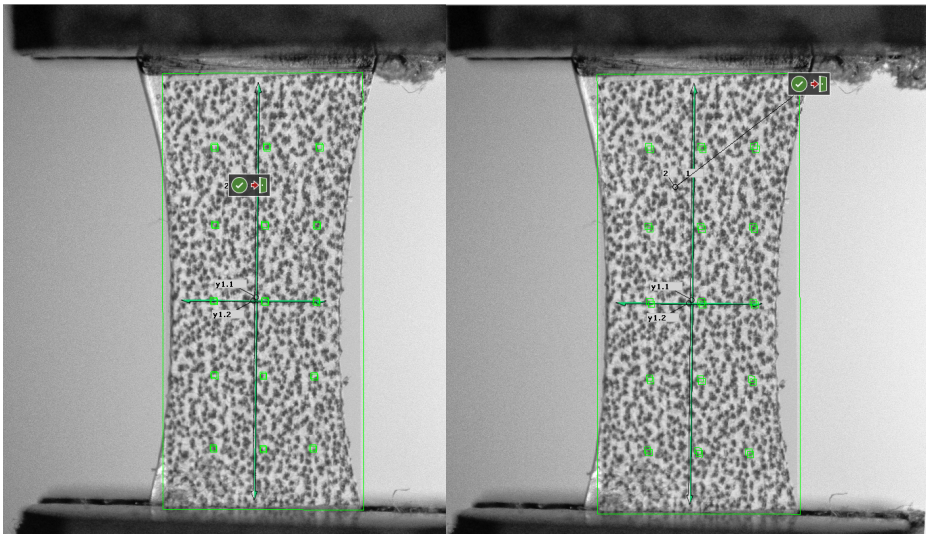

(a) Facet size=20, Point distance=5. **(b) Facet size=20, Point distance=10**

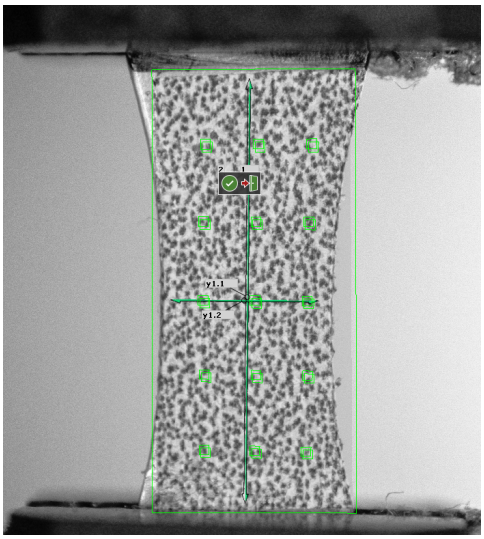

(c) Facet size=30, Point distance=10

Fig. 56 Different Facet and Distance Settings (in pixels).

Also, the difference in quality of different facet size and distance is shown in below figure, where relatively high facet size may harm quality and relatively low distance may not cover the whole sample in the DIC. As a result, a setting with facet size of 20 pixels and distance of 10 pixels is adopted for the analysis.

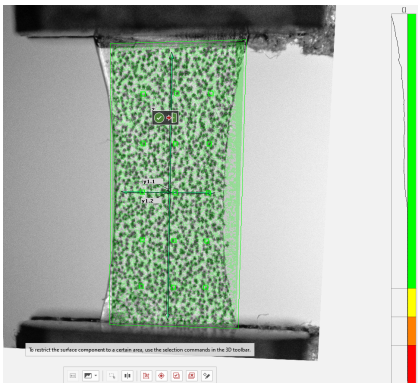

(a) Facet size=20, Point distance=5.

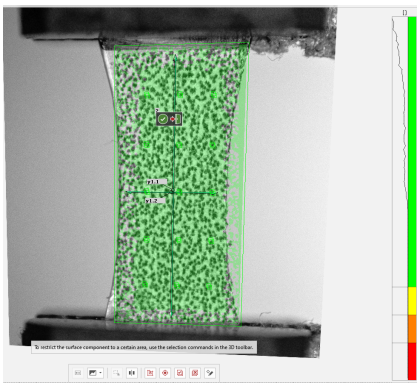

(b) Facet size=20, Point distance=10

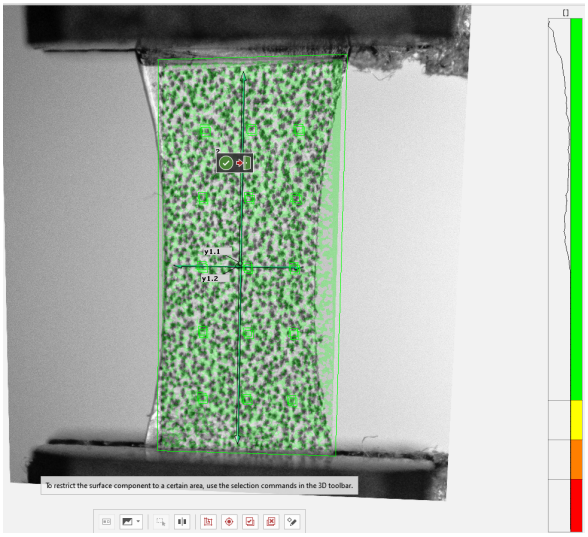

(c) Facet size=30, Point distance=10

Fig. 57 Quality of the points by different Facet and Distance Settings (in pixels).

C. Modeling

From the experiment to the modeling, there might be some point that needs extra work to ensure the quality of the data and improve the code quality when transferring from PMMA to PEI.

1. Choice of ODE solver: ODE15s, ODE45 and ODE113 may be considered in the modeling of polymer cell growth model. Among these method, ODE45 and ODE113 suits better for the stiff problems and ODE15s suits better for non-stiff problems. More detailed comparison can be seen from the table below.

Solver	Type	Best Suited For	Characteristics
`ode45`	Non-stiff, single-step	General non-stiff problems	Based on explicit Runge-Kutta (4,5) method; good for smooth problems
`ode113`	Non-stiff, multi-step	Smooth problems requiring high precision	Variable-order Adams-Bashforth-Moulton PECE solver; efficient for smooth solutions
`ode15s`	Stiff, multi-step	Stiff problems and differential-algebraic equations (DAEs)	Variable-order solver based on numerical differentiation formulas (NDFs); handles stiffness effectively

Table 4 Comparison of MATLAB ODE Solvers Commonly Used in Polymer Modeling

Stiffness in differential equations often arises in systems where certain components exhibit rapid changes while others vary slowly, a common scenario in polymer modeling due to the interplay of fast chemical reactions and slower transport processes. To determine whether a polymer system is stiff or not, one possible method is ease of maintaining numerical stability over a time period. If the system requires an impractically small time step to keep stable, it is likely to be stiff. Similar behavior was not observed in the PEI cell growth model where no significant longer time is observed to keep the stability, so the system is considered to be non-stiff and ODE15s is considered as a optimal choice.

D. Cell Size Measurement

It can be seen from the previous part that the overall fitting of the measured and predicted model is accurate except 135 °C. Given the mechanics of cell growth with releasing CO_2 in the foaming process, slight error may exist at the temperature around 135 °C. Such underestimation can be result of either sample preparation or SEM process. During sample preparation like sanding, small crack may form which can't be clearly captured resulting in collapse of pore structures leading to underestimation. [72]. In the SEM process, nanoscale polymer particle may suffer from increase adhesion to the substrate due to electron beam exposure leading to flattened particle or distortion. Electron beam may induce charging or thermal effects leading to softening or plastic deformation of surfaces of polymer. This process may lead to underestimation of cell sizes. [73] Image distortions or significant charging can also effects during secondary electron SEM analysis—evident as bright areas encircled by dark halos, which makes it hard for ImageJ to capture the accurate cells which leads to errors in cell size measurement. [74]

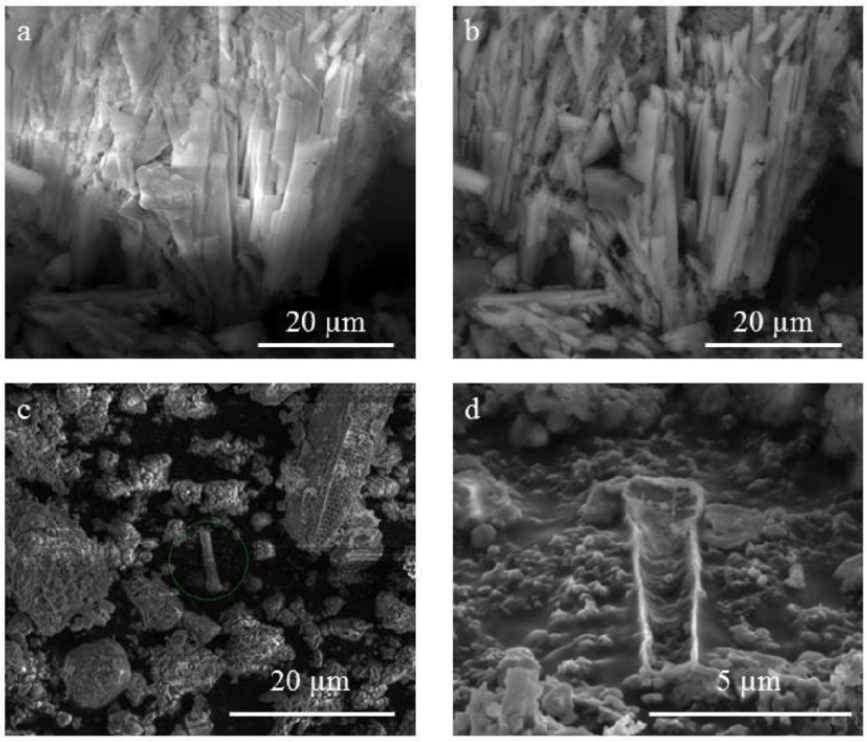

Fig. 58 Distorted SEM Images Examples [74]

References

[1] Muhammad Muqeet, Rasool Bux Mahar, and N. B. Halima. "Insight into cellulose-based-nanomaterials – A pursuit of environmental remedies". In: *International Journal of Biological Macromolecules* 163 (2020), pp. 1649–1665. DOI: 10.1016/j.ijbiomac.2020.08.050. URL: https://doi.org/10.1016/j.ijbiomac.2020.08.050.

[2] A. Ravve. "Naturally Occurring Polymers". In: *Principles of Polymer Chemistry*. 3rd. Springer, 2012, pp. 537–565. DOI: 10.1007/978-1-4614-2212-9. URL: https://doi.org/10.1007/978-1-4614-2212-9.

[3] Shraddha R. Patil, Shubhangi S. Salunkhe, and Ravindra B. Saudagar. "Extraction, Modification, and Characterization of Natural Polymers Used in Transdermal Drug Delivery System: An Updated Review". In: *Asian Journal of Pharmaceutical Research and Development* 11.2 (2023), pp. 46–53. DOI: 10.22270/ajprd.v11i2.1172.

[4] Samanta Castañeda-Rodríguez et al. "Recent Advances in Modified Poly (Lactic Acid) as Tissue Engineering Materials". In: *Journal of Biological Engineering* 17.1 (2023), p. 21. DOI: 10.1186/s13036-023-00338-8. URL: https://jbioleng.biomedcentral.com/articles/10.1186/s13036-023-00338-8.

[5] Xin Wang et al. "3D Printing of Polymer Matrix Composites: A Review and Prospective". In: *Composites Part B: Engineering* 110 (2017), pp. 442–458. DOI: 10.1016/j.compositesb.2016.11.034.

[6] Raphael Kudela. *Ask the Naturalist: Sea Foam – How Much is Too Much?* 2015. URL: https://baynature.org/article/ask-the-naturalist-seafoam-how-much-is-too-much/.

[7] Christopher Hill and J. Eastoe. "Foams: From nature to industry". In: *Advances in Colloid and Interface Science* 247 (2017), pp. 496–513. DOI: 10.1016/j.cis.2017.05.013.

[8] Robert Frouin, Myriam Schwindling, and Pierre-Yves Deschamps. "Spectral Reflectance of Sea Foam in the Visible and Near-Infrared: In Situ Measurements and Remote Sensing Implications". In: *Journal of Geophysical Research: Oceans* 101.C6 (1996), pp. 14361–14371. DOI: 10.1029/96JC00629. URL: https://agupubs.onlinelibrary.wiley.com/doi/10.1029/96JC00629.

[9] Rachel I.L. Fleming et al. "Building a Home from Foam—Túngara Frog Foam Nest Architecture and Three-Phase Construction Process". In: *Philosophical Transactions of the Royal Society B: Biological Sciences* 376.1839 (2021), p. 20200190. DOI: 10.1098/rstb.2020.0190.

[10] Xiaoyan Wang et al. "Preparation of Foam Concrete from Solid Wastes: Physical Properties and Foam Stability". In: *Journal of Cleaner Production* 278 (2021), p. 123888. DOI: 10.1016/j.jclepro.2020.123888.

[11] E. Archer and D. Bergstrom. "Structural Plastic Foams: Current Status". In: *Polymer Engineering & Science* 14.11 (Nov. 1974), pp. 803–808. DOI: 10.1002/pen.760141104.

[12] J. Throne. "The Newer Structural Foam Techniques". In: *Polymer Engineering & Science* 16.9 (Sept. 1976), pp. 660–662. DOI: 10.1002/pen.760160910.

[13] Swapnil Morankar et al. "Structural Features of Biobased Composite Foams Revealed by X-ray Tomography". In: *RSC Advances* 14 (2024), pp. 19528–19538. DOI: 10.1039/D4RA02461C.

[14] M. Mccoy. "To sleep, perchance on foam". In: *Chemical & Engineering News* (2017).

[15] Kirsten Dreggors. "Alternative Foam Treatments For The Space Shuttle's External Tank". Accessed: 2025-05-13. Master's thesis. Orlando, FL: University of Central Florida, 2005. URL: https://stars.library.ucf.edu/etd/548/.

[16] K.C. Frisch. "History of Science and Technology of Polymeric Foams". In: *Journal of Macromolecular Science, Part A: Chemistry* 15.4 (1981), pp. 729–752. DOI: 10.1080/00222338108066455. URL: https://www.tandfonline.com/doi/abs/10.1080/00222338108066455.

[17] Vipin Kurma Dustin Miller. "Microcellular and nanocellular solid-state polyetherimide (PEI) foams using sub-critical carbon dioxide II. tensile and impact properties". In: *Polymer* 52 (2011).

[18] Mohammad Harun-Ur-Rashid et al. "Bio-Inspired Nanomaterials for Micro/Nanodevices: A New Era in Biomedical Applications". In: *Micromachines* 14.9 (2023), p. 1786. DOI: 10.3390/mi14091786. URL: https://www.mdpi.com/2072-666X/14/9/1786.

[19] Fan-Long Jin et al. "Recent Trends of Foaming in Polymer Processing: A Review". In: *Polymers* 11.6 (2019), p. 953. DOI: 10.3390/polym11060953. URL: https://www.mdpi.com/2073-4360/11/6/953.

[20] Aurelio Salerno and Concepción Domingo Pascual. "A clean and sustainable route towards the design and fabrication of biodegradable foams by means of supercritical CO_2/ethyl lactate solid-state foaming". In: *RSC Advances* 3.38 (2013), pp. 17355–17363. DOI: 10.1039/C3RA42345J. URL: https://pubs.rsc.org/en/content/articlelanding/2013/ra/c3ra42345j.

[21] Ronan M. O'Higgins John W. McLaughlin Emma Tobin. "An investigation of Polyether Imide (PEI) toughening of carbon fibre-reinforced Polyether Ether Ketone (PEEK) laminates". In: *Materials & Design* 212 (2021).

[22] M. Stegelmann, P. Lucas, and N. Modler. "Design and Extrusion of High-Performance Polyetherimide Pipes with Variable Wall Thickness for Aircrafts". In: *AIP Conference Proceedings*. Vol. 2055. 2019, p. 070008. DOI: 10.1063/1.5084852. URL: https://pubs.aip.org/aip/acp/article/2055/1/070008/617597/Design-and-extrusion-of-high-performance.

[23] Yanan Li, Enno Ruijters, and Mariëlle Stoelinga. "Data-driven safety assessment of dynamic fault trees using Bayesian networks and importance measures". In: *Reliability Engineering & System Safety* 210 (2021), p. 107514. DOI: 10.1016/j.ress.2021.107514. URL: https://www.sciencedirect.com/science/article/abs/pii/S0951833921000812.

[24] Ved S. Vakharia et al. "Multi-Material Additive Manufacturing of High Temperature Polyetherimide (PEI)–Based Polymer Systems for Lightweight Aerospace Applications". In: *Polymers* 15.3 (2023), p. 561. DOI: 10.3390/polym15030561. URL: https://www.mdpi.com/2073-4360/15/3/561.

[25] Dong Feng, Li Li, and Qi Wang. "Fabrication of three-dimensional polyetherimide bead foams via supercritical CO_2/ethanol co-foaming technology". In: *RSC Advances* 9.7 (2019). Accessed: 2025-05-08, pp. 4072–4081. DOI: 10.1039/C8RA09706B. URL: https://doi.org/10.1039/C8RA09706B.

[26] D. Miller, Pavee Chatchaisucha, and Vipin Kumar. "Microcellular and Nanocellular Solid-State Polyetherimide (PEI) Foams Using Sub-Critical Carbon Dioxide I. Processing and Structure". In: *Polymer* 50.24 (2009), pp. 5576–5584. DOI: 10.1016/j.polymer.2009.09.020. URL: https://doi.org/10.1016/j.polymer.2009.09.020.

[27] Kush Dwiwedi et al. "Breaking Down the Exceptional Size-Dependent Toughness of Nanocellular Foams". In: *SSRN* (). DOI: http://dx.doi.org/10.2139/ssrn.5208612.

[28] Santhosh Sridhar et al. "Experimental validation of effective glass transition temperature-based model for predicting skin thickness in solid-state microcellular foams". In: *Polymer Engineering & Science* 65.1 (2025), pp. 100–107. DOI: https://doi.org/10.1002/pen.26994.

[29] Alaa Al-Fatlawi, Károly Jármai, and György Kovács. "Optimization of a Totally Fiber-Reinforced Plastic Composite Sandwich Construction of Helicopter Floor for Weight Saving, Fuel Saving and Higher Safety". In: *Polymers* 13.16 (2021), p. 2735. DOI: 10.3390/polym13162735. URL: https://www.mdpi.com/2073-4360/13/16/2735.

[30] "Nature article on bioinspired materials and foam mechanics". In: *Scientific Reports* 14 (2024), p. 51719. URL: https://www.nature.com/articles/s41598-024-51719-y.

[31] Louis Laberge Lebel and Daniel Therriault. "Multiscale Manufacturing of Three-Dimensional Polymer-Based Nanocomposite Structures". In: *Advances in Diverse Industrial Applications of Nanocomposites*. Ed. by Boreddy Reddy. InTechOpen, 2011, pp. 409–428. DOI: 10.5772/15231. URL: https://doi.org/10.5772/15231.

[32] Louis Laberge Lebel and Daniel Therriault. "Multiscale Manufacturing of Three-Dimensional Polymer-Based Nanocomposite Structures". In: *Advances in Diverse Industrial Applications of Nanocomposites*. Ed. by Boreddy Reddy. IntechOpen, 2011, pp. 409–428. DOI: 10.5772/15231. URL: https://doi.org/10.5772/15231.

[33] Friederike Schmid. "Understanding and Modeling Polymers: The Challenge of Multiple Scales". In: *ACS Polymers Au* 3.1 (2023), pp. 28–44. DOI: 10.1021/acspolymersau.2c00049. URL: https://doi.org/10.1021/acspolymersau.2c00049.

[34] L. Dai, Y. Wang, and H. Zhang. "Effect of microstructure of nano- and micro-particle filled polymer composites on their tribo-mechanical performance". In: *Journal of Physics: Conference Series* 126.1 (2008), p. 012057. DOI: 10.1088/1742-6596/126/1/012057.

[35] Takashi Miyamoto et al. "Bioabsorbable polymers for medical devices". In: *Current Pharmaceutical Design* 20.28 (2014), pp. 5601–5607. DOI: 10.2174/1381612820666140821120518. URL: https://pubmed.ncbi.nlm.nih.gov/25319179/.

[36] Jiaqi Yu et al. "Preparation of polymer foams with a gradient of cell size: Further exploring the nucleation effect of porous inorganic materials in polymer foaming". In: *Materials Today Communications* 9 (2016), pp. 1–6. DOI: 10.1016/j.mtcomm.2016.08.006. URL: https://doi.org/10.1016/j.mtcomm.2016.08.006.

[37] Sergio Estravis et al. "Thermodynamic limits on cell size in the production of stable polymeric nanocellular materials". In: *Polymer* 186 (2020), p. 122036. DOI: 10.1016/j.polymer.2019.122036. URL: https://www.sciencedirect.com/science/article/pii/S0032386119310420.

[38] Yongyan Pang et al. "A Comprehensive Review of Cell Structure Variation and General Rules for Polymer Microcellular Foams". In: *Chemical Engineering Journal* 430 (2022), p. 132662. DOI: 10.1016/j.cej.2021.132662. URL: https://doi.org/10.1016/j.cej.2021.132662.

[39] D. Hossain et al. "Molecular Dynamics Simulations of Deformation Mechanisms of Amorphous Polyethylene". In: *Polymer* 51.24 (2010), pp. 6071–6083. DOI: 10.1016/j.polymer.2010.10.009. URL: https://www.sciencedirect.com/science/article/pii/S0032386110008839.

[40] Frederik Van Loock et al. "The mechanics of solid-state nanofoaming". In: *Proceedings of the Royal Society A: Mathematical, Physical and Engineering Sciences* 475.2230 (2019).

[41] Michele Zappalorto, Marco Salviato, and Marino Quaresimin. “Influence of the interphase zone on the nanoparticle debonding stress”. In: *Composites Science and Technology* 72.1 (2011), pp. 49–55. DOI: https://doi.org/10.1016/j.compscitech.2011.09.016.

[42] Michele Zappalorto, Marco Salviato, and Marino Quaresimin. “A multiscale model to describe nanocomposite fracture toughness enhancement by the plastic yielding of nanovoids”. In: *Composites Science and Technology* 72.14 (2012), pp. 1683–1691. DOI: https://doi.org/10.1016/j.compscitech.2012.07.010.

[43] Marino Quaresimin, Marco Salviato, and Michele Zappalorto. “A multi-scale and multi-mechanism approach for the fracture toughness assessment of polymer nanocomposites”. In: *Composites Science and Technology* 91 (2014), pp. 16–21. DOI: https://doi.org/10.1016/j.compscitech.2013.11.015.

[44] Michele Zappalorto, Marco Salviato, and Marino Quaresimin. “Stress distributions around rigid nanoparticles”. In: *International Journal of Fracture* 176 (2012), pp. 105–112. DOI: https://doi.org/10.1007/s10704-012-9714-2.

[45] Marco Salviato, Michele Zappalorto, and Marino Quaresimin. “Plastic yielding around nanovoids”. In: *Procedia Engineering* 10 (2011), pp. 3316–3321.

[46] Eichinger B.E Rigby David. “Polymer modeling: where has it been and where is it going?” In: *Macromolecular Symposia* 201 (1 2003).

[47] Thomas E. Gartner III and Arthi Jayaraman. “Modeling and Simulations of Polymers: A Roadmap”. In: *Macromolecules* 52 (3 2019).

[48] Yutaka Oya et al. “Molecular dynamics simulation of cross-linking processes and material properties for epoxy resins using first-principle calculation combined with global reaction route mapping algorithms”. In: *Chemical Physics Letters* 762 (2021), p. 138104. DOI: https://doi.org/10.1016/j.cplett.2020.138104.

[49] Norman A. Fleck Frederik Van Loock. “Deformation and failure maps for PMMA in uniaxial tension”. In: *Polymer* 148 (2018).

[50] Mark R. Holl et al. “A steady-state mass balance model of the polycarbonate–CO_2 system reveals a self-regulating cell growth mechanism in the solid-state microcellular process”. In: *Journal of Polymer Science Part B: Polymer Physics* 39.8 (2001), pp. 868–880. DOI: 10.1002/polb.1061. URL: https://doi.org/10.1002/polb.1061.

[51] Luigi Sorrentino Livia Cafiero Salvatore Iannace. “Microcellular foams from high performance miscible blends based on PEEK and PEI”. In: *European Polymer Journal* 78 (1 2016).

[52] Anna Makuch et al. *Initial Research of Changes in Mechanical Properties of Polymer-Graphene Composite with Use of Digital Image Correlation*. https://www.researchgate.net/publication/340414989_Initial_research_of_changes_in_mechanical_properties_of_polymer-graphene_composite_with_use_of_Digital_Image_Correlation. Accessed: 2025-04-11. 2020.

[53] Li Li et al. “Progress in preparation of high-performance and multi-functional polymer foams”. In: *Journal of Polymer Science* 62 (14 2024).

[54] J. -P. Crine. “Influence of temperature and elastic properties on some polymer relaxations”. In: *2016 IEEE International Conference on Dielectrics (ICD)* (2016).

[55] Nicholas . Young and Nitash P. Balsara. *Flory Huggins Equation*. Springer Reference, 2014.

[56] A.P.C. Duarte et al. “Determination of the temperature-dependent thermophysical properties of polymeric foams using numerical inverse analysis”. In: *Construction and Building Materials* 394 (2023).

[57] Wenbin Zhang et al. “Parametric study on the regeneration heat requirement of an amine-based solid adsorbent process for post-combustion carbon capture”. In: *Applied Energy* 168 (2016).

[58] Adam Katunin and Adam Gnatowski. “Influence of heating rate on evolution of dynamic properties of polymeric laminates”. In: *Plastics, Rubber and Composites* 41.6 (2012), pp. 233–239. DOI: 10.1179/1743289811Y.0000000037.

[59] NETZSCH-Gerätebau GmbH. *PEI: Polyetherimide*. Accessed: 2025-04-09. 2025. URL: https://polymers.netzsch.com/Materials/Details/41.

[60] Gong-shun Guan, Shao-heng Wang, and Fang-yuan Cheng. “Compression Failure and Mechanics Behavior of PMMA under Different Loading Strain Rates”. In: *Journal of Aeronautical Materials* 32.6 (2012), pp. 96–101. DOI: 10.3969/j.issn.1005-5053.2012.6.015.

[61] Ismail Hadriche et al. “Influence of Strain Rate on the Yielding Behavior and on the Self Heating of Thermoplastic Polymers Loaded under Tension”. In: *Key Engineering Materials* 446 (2010), pp. 63–72. DOI: 10.4028/www.scientific.net/KEM.446.63.

[62] Ana García Ramón Artiaga. *Fundamentals of DMA*. Universidade da Coruña, 2005.

[63] Gleb Vaganov et al. “Comparison of properties of carbon reinforced plastic obtained on the basis of semicrystalline polyimide R-BAPB and other high-temperature-resistant thermoplastic matrices”. In: *Journal of Applied Polymer Science* 140.33 (2023), e54283. DOI: 10.1002/app.54283. URL: https://doi.org/10.1002/app.54283.

[64] Kristen T. Kern, Wynford L. Harries, and Sheila Ann T. Long. “Dynamic Mechanical Analysis of Polymeric Materials”. In: *National Educators’ Workshop: Update 1989 Standard Experiments in Engineering Materials Science and Technology*. NASA Technical Reports Server, 1990, pp. 13–16. URL: https://ntrs.nasa.gov/citations/19900015037.

[65] Kevin P. Menard and Noah Menard. *Dynamic Mechanical Analysis*. 3rd. Boca Raton: CRC Press, 2020. DOI: 10.1201/9780429190308. URL: https://doi.org/10.1201/9780429190308.

[66] Weixin Li et al. “Elastic and fracture behavior of three-dimensional ply-to-ply angle interlock woven composites: Through-thickness, size effect, and multiaxial tests”. In: *Composites Part C: Open Access* 4 (2021), p. 100098. DOI: https://doi.org/10.1016/j.jcomc.2020.100098.

[67] Seunghyun Ko et al. “Effect of the thickness on the fracturing behavior of discontinuous fiber composite structures”. In: *Composites Part A: Applied Science and Manufacturing* 125 (2019), p. 105520. DOI: https://doi.org/10.1016/j.compositesa.2019.105520.

[68] Seunghyun Ko et al. “Effect of the platelet size on the fracturing behavior and size effect of discontinuous fiber composite structures”. In: *Composite Structures* 227 (2019), p. 111245. DOI: https://doi.org/10.1016/j.compstruct.2019.111245.

[69] Jeremy Brockmann and Marco Salviato. “The gap test–effects of crack parallel compression on fracture in carbon fiber composites”. In: *Composites Part A: Applied Science and Manufacturing* 164 (2023), p. 107252. DOI: https://doi.org/10.1016/j.compositesa.2022.107252.

[70] Benji Boerner Valerio Oddone and Stephanie Reich. “Composites of aluminum alloy and magnesium alloy with graphite showing low thermal expansion and high specific thermal conductivity”. In: *Science and Technology of Advanced Materials* 18 (1 2017).

[71] J Perez and J.Y Cavaillé. “Temperature dependence of the molecular dynamics in amorphous polymers through the rubber-glass transition”. In: *Journal of Non-Crystalline Solids* 172-174 (2 1994).

[72] Douglas Faith, Colin J. Horsfield, and Wigen Nazarov. “Characterization of pore size of trimethylol propane triacrylate (TMPTA) polymer foam by pulsed sputter coating and SEM analysis”. In: *Journal of Materials Science* 41.13 (2006), pp. 3973–3977. DOI: 10.1007/s10853-006-7572-x.

[73] Hideki T. Miyazaki et al. “Adhesion of micrometer-sized polymer particles under a scanning electron microscope”. In: *Journal of Applied Physics* 88.6 (2000), pp. 3330–3340. DOI: 10.1063/1.1289499.

[74] José Juan Francisco Castillo et al. “Identification of diagenetic calcium arsenates using synchrotron-based micro X-ray diffraction”. In: *Boletín de la Sociedad Geológica Mexicana* 67.3 (2015), pp. 479–491. DOI: 10.18268/BSGM2015v67n3a11.

VIII. Appendix

A. DMA Testing Parameters

Parameter	Unit	Value
Starting Temperature	°C	25
Ending Temperature	°C	125–205
Temperature Gap	°C/sample	10
Heat Rate	°C/min	10
Strain Rate	%/s	0.3175
Sample Thickness	mm	0.5
Waveform	/	Sine Wave

Table 5 DMA Testing Parameters

B. Time Step Filtering before DIC

```
import pandas as pd

# Load the .ods file
file_path = '.ods'
data = pd.read_excel(file_path, engine='openpyxl')

# Convert 'Elapsed Time' to numeric (if necessary)
data['Elapsed Time'] = pd.to_numeric(data['Elapsed Time'], errors='coerce'
    )

# Filter the rows where 'Elapsed Time' is even
filtered_data = data[data['Elapsed Time'] % 2 == 0]

# Extract data from 'Load' column
load_column_data = filtered_data['Load']

# Save the filtered data to a new CSV file
output_file_path = 'name.csv'
load_column_data.to_csv(output_file_path, index=False)

print(f"Filtered data saved to {output_file_path}")
```

C. More DIC Results

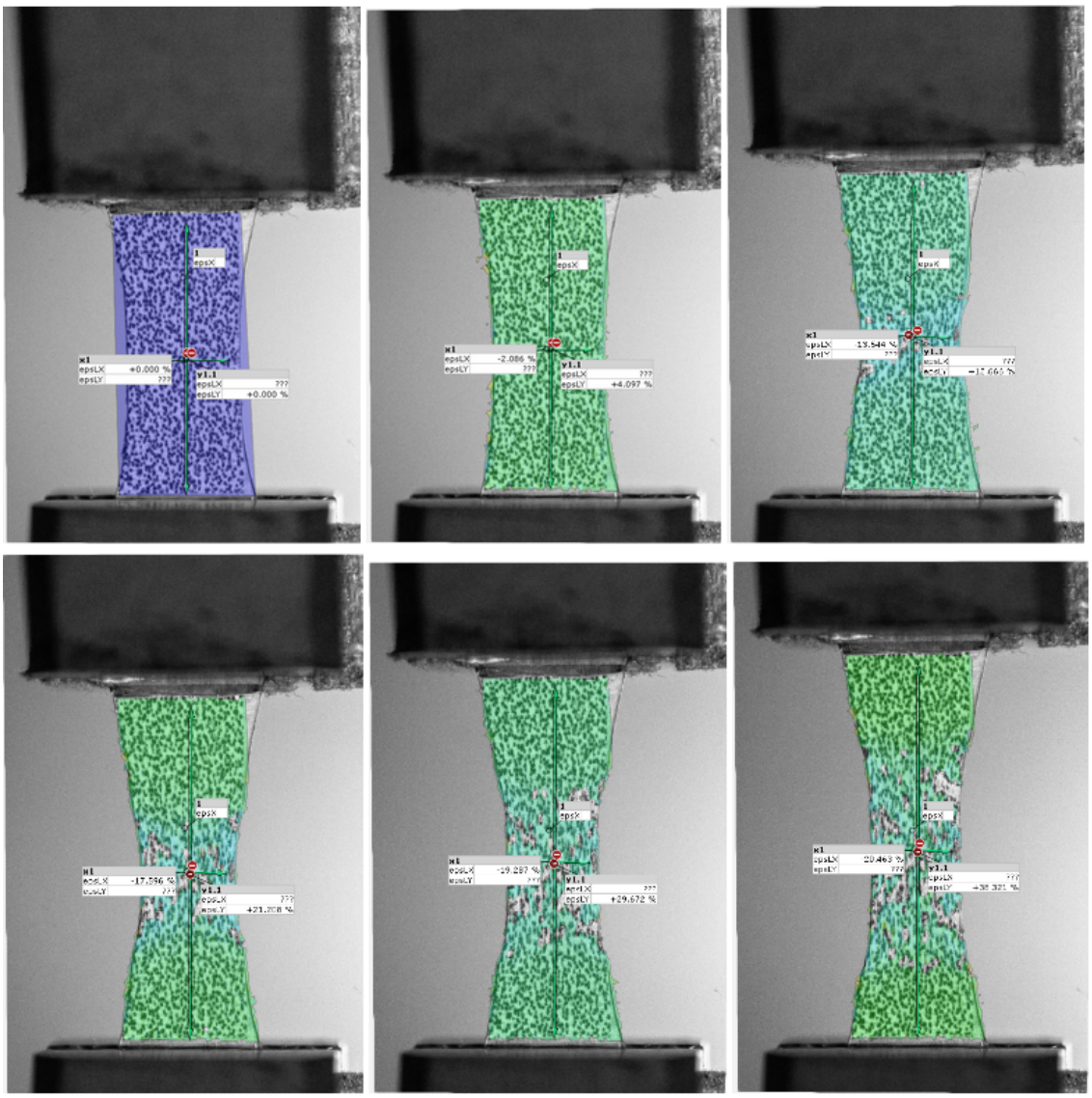

Fig. 59 DIC Results under 50 °C **with 6.25% strain difference between each other (Foaming hasn't yet started at** 50 °C**.**

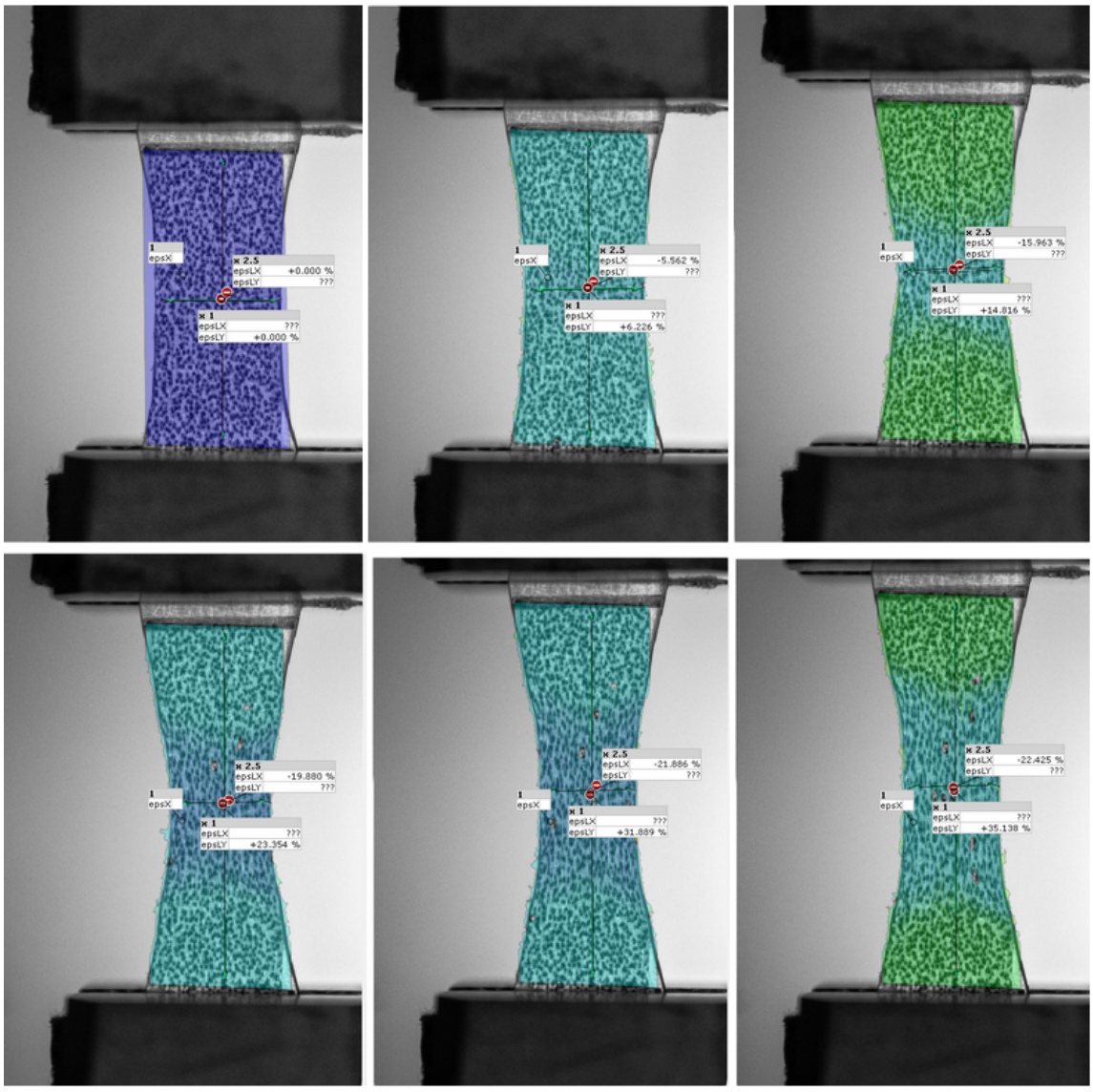

Fig. 60 DIC Results under 150 °C **with 6.25% strain difference between each other.**

And the raw data of DIC is shown below.

t1 (s)	LCFS (N)	epsLY(%)	t(mm)	w(mm)	A(mm^2)	σ(Mpa)	εy	εx
0.00	1.11	0.00	0.50	5.00	2.50	0.44	0.040819	0.000000
20.10	28.63	1.88	0.48	4.79	2.29	12.49	0.041569	0.018588
40.20	61.70	2.85	0.48	4.79	2.29	26.94	0.041958	0.028089
60.30	83.70	3.66	0.48	4.78	2.29	36.57	0.042282	0.035959
80.40	89.16	4.53	0.48	4.78	2.29	38.98	0.042630	0.044318
100.50	86.04	5.61	0.48	4.78	2.28	37.65	0.043059	0.054561
120.60	83.83	7.32	0.48	4.78	2.28	36.75	0.043742	0.070648
140.70	82.94	11.29	0.48	4.77	2.27	36.48	0.045323	0.106939
160.80	81.28	16.75	0.48	4.76	2.26	35.92	0.047494	0.154833
180.90	80.17	21.39	0.47	4.75	2.25	35.57	0.049339	0.193871
201.00	75.67	25.97	0.47	4.74	2.24	33.71	0.051154	0.230906
221.10	71.91	30.48	0.47	4.73	2.24	32.17	0.052936	0.266043
241.20	68.70	34.99	0.47	4.72	2.23	30.85	0.054717	0.300038
261.30	66.58	39.40	0.47	4.71	2.22	30.02	0.056456	0.332205
281.40	64.31	43.84	0.47	4.70	2.21	29.11	0.058202	0.363538
301.50	60.64	48.21	0.47	4.69	2.20	27.55	0.059916	0.393436
321.60	57.14	52.34	0.47	4.68	2.19	26.06	0.061537	0.420938
342.71	52.73	56.58	0.47	4.67	2.18	24.14	0.063196	0.448386
362.81	50.73	60.31	0.47	4.67	2.18	23.30	0.064656	0.471963
382.91	48.07	63.73	0.47	4.66	2.17	22.15	0.065990	0.493060
403.01	31.11	66.58	0.47	4.65	2.17	14.37	0.067101	0.510310
423.11	29.54	69.09	0.46	4.65	2.16	13.67	0.068077	0.525256

Fig. 61 Raw Result after DIC.

D. Main MATLAB Code for 1 MPa Case Study

1. Initialization

```
clear all
close all
clc

global T_g_0 C1 C2 eps_ref R_g gamma C_0 c_0 R_0 b_0 x_mesh counter pg_0
   Pamb pressure_vec ...
      counter_smooth rho_L t_end temp_up temp_low c_vec eta_g tau t_vec ...

      rho_0 M_w rho_vec temp_vec tg_vec stress_profile_vec f_int_vec
         a_rate time a_vec K_H ...
      stress_vec sigma_plastic_vec sigma_rubber mechanism_vec
```

Listing 1 Clear environment and declare global variables

2. Simulation Parameters and Initial Conditions

```
filename = '1MPa.xlsx';
tic

N_0 = 1E21;
```

```
pg_0 = 1*10^6;
Pamb = 0.1013*10^6;
M_w = 44*10^-3;
R_g = 8.31441;
gamma = 0.046;
rho_L = 1270;

R_0 = 5*10^-9;
K_H = 1.05*10^-3;
K_H2 = K_H * M_w / rho_L;
c_0 = pg_0 * K_H2;

por_0 = (3/(R_0^3 * 4 * 3.1415 * N_0) + 1)^-1;
b_0 = (R_0^3 / por_0)^(1/3);
C_0 = pg_0 * K_H;

T_g_0 = 217 + 273;

t_0 = 0;
t_end = 600;
t_n = 1e3;
t_span = linspace(t_0, t_end, t_n);

x_0 = R_0;
x_end = b_0;
x_n = 1e2;
x_mesh = logspace(log10(x_0), log10(x_end), x_n);

a_0 = R_0;

t_par_vec = [175, 185, 195, 205];
tau_vec = ones(1, length(t_par_vec)) * 1.45;
t_par_vec = (t_par_vec + 273) ./ (T_g_0);

data_all = [];
legend_entries = cell(1, length(t_par_vec));
```

Listing 2 Define simulation and material parameters

3. ODE Simulation and Data Export

```
for i = 1:length(t_par_vec)
    tau = tau_vec(i);
    temp_low = 273;
    temp_up = t_par_vec(i) * T_g_0;

    opts = odeset('RelTol', 1e-16, 'AbsTol', 1e-16, 'Stats', 'on');
```

```
    counter = 0;
    [t, x] = ode15s(@odesolver_uniformconcentration_new, t_span, [a_0],
        opts);

    T_Tg_vec = temp_vec' ./ tg_vec';
    log_T_Tg_vec = log(T_Tg_vec);

    a_vec = x(:, 1);
    b_vec = (a_vec.^3 + b_0^3 - a_0^3).^(1/3);
    porosity = a_vec.^3 ./ b_vec.^3;

    porosity_vs_time(x, b_0, a_0, t, temp_up);

    maxlen = max([length(time'), length(a_rate'), length(pressure_vec'),
        ...
        length(stress_vec'), length(c_vec'), length(T_Tg_vec), length(
            log_T_Tg_vec)]);

    data = NaN(maxlen, 8);
    data(1:length(time'), 1) = time';
    data(1:length(a_rate'), 2) = a_rate';
    data(1:length(pressure_vec'), 3) = pressure_vec';
    data(1:length(stress_vec'), 4) = stress_vec';
    data(1:length(c_vec'), 5) = c_vec';
    data(1:length(T_Tg_vec), 6) = T_Tg_vec;
    data(1:length(log_T_Tg_vec), 7) = log_T_Tg_vec;
    data(1:length(porosity), 8) = porosity';

    sheetname = num2str(175 + (i-1) * 10);
    xlswrite(filename, data, sheetname);
end
```

Listing 3 ODE integration and Excel export

4. Plotting: Growth Rate and Stress Responses

```
counter = 0;
a_rate = [];
time = [];
a_vec = [];
pressure_vec = [];
temp_vec = [];
tg_vec = [];
stress_profile_vec = [];
f_int_vec = [];
rho_vec = [];
c_vec = [];
```

```
stress_vec = [];
sigma_plastic_vec = [];
sigma_rubber = [];
mechanism_vec = [];
t_vec = [];

for i = 1:length(t_par_vec)
    tau = tau_vec(i);
    temp_low = 273;
    temp_up = t_par_vec(i) * T_g_0;

    opts = odeset('RelTol', 1e-16, 'AbsTol', 1e-16, 'Stats', 'on');
    counter = 0;
    [t, x] = ode15s(@odesolver_uniformconcentration_new, t_span, [a_0],
       opts);

    figure(1)
    semilogy(time, a_rate, 'LineWidth', 1.5)
    hold on
    xlim([0 50])
    ylim([0 5e-4])

    legend_entries{i} = sprintf('T_f = %.0f', t_par_vec(i) * T_g_0 - 273);
end

legend(legend_entries)
xlabel('Time (s)')
ylabel('da/dt (m/s)')
title('Growth Rate vs. Time')

\subsection{ODE Solver Function}
\begin{lstlisting}[caption={Uniform concentration ODE solver}]
function [dxdt] = odesolver_uniformconcentration_new(t, x)
    global T_g_0 C1 C2 eps_ref R_g gamma C_0 c_0 R_0 b_0 x_mesh counter
       pg_0 Pamb pressure_vec ...
          a_rate a_vec counter_smooth rho_L t_end temp_up temp_low c_vec
             eta_g tau t_vec ...
          rho_0 M_w rho_vec temp_vec tg_vec stress_profile_vec f_int_vec
             time K_H

    counter = counter + 1;
    t_vec(counter) = t;
    disp(t)

    b_3 = (x(1)^3 - R_0^3 + b_0^3);
    temp = temp_function_exp(t, temp_low, temp_up, tau);
```

```
    if counter == 1
        p = pg_0;
        c = C_0;
    else
        p = ((b_0^3 - R_0^3) * C_0 + R_0^3 * pg_0 / (R_g * temp_low)) / ...
            (x(1)^3 / (R_g * temp) + (b_3 - x(1)^3) * K_H);
        c = K_H * p;
    end

    c_vec(counter) = c;
    tg = tg_function(T_g_0, c, rho_L);
    a = x(1);
    a_vec(counter) = a;

    if counter == 1
        a_dot_0 = 0;
    else
        a_dot_0 = a_rate(counter - 1);
    end

    fun = @(a_dot_var) function_root_adot(a_dot_var, a, p, temp, tg);
    a_dot = fzero(fun, a_dot_0);

    a_rate(counter) = a_dot;
    time(counter) = t;
    pressure_vec(counter) = p;
    temp_vec(counter) = temp;
    tg_vec(counter) = tg;

    dxdt = [a_dot];
end
```

Listing 4 Plot growth rate and other figures

5. Root-Finding Function for Growth Rate

```
function [y] = function_root_adot(x, a, p, temp, T_g)
    global T_g_0 R_0 x_mesh counter Pamb stress_profile_vec f_int_vec ...
           stress_vec sigma_plastic_vec sigma_rubber mechanism_vec

    for s = 1:length(x_mesh)
        R(s) = x_mesh(s);
        r_R(s) = (1 + (a^3 - R_0^3) / R(s)^3)^(1/3);
        eps(s) = 2 * log(r_R(s));
        eps_dot(s) = (2 * a^2 * x) / (R(s)^3) * r_R(s)^(-3);
```

```
        [stress, sigma_plastic, sigma_rubber1, mechanism] = ...
            stress_function_lowmw(T_g_0, temp, T_g, eps_dot(s), eps(s));

        f_int(s) = 2 / R(s) * (r_R(s))^(-3) * stress;
        stress_profile_vec(s) = stress;
    end

    int_value = trapz(x_mesh, f_int);

    stress_vec(counter) = stress(1);
    sigma_plastic_vec(counter) = sigma_plastic(1);
    sigma_rubber(counter) = sigma_rubber1(1);
    mechanism_vec(counter) = mechanism(1);

    y = (p - Pamb) - int_value;
end
```

Listing 5 Force balance root-finding equation

6. Stress Function (Plastic and Viscous)

```
function [stress, sigma_plastic, sigma_viscous, mechanism] = ...
        stress_function_lowmw(Tg_0, T, Tg, eps_dot, eps)

    k_b = 1.38064852E-23;
    v = 7.5E-27;
    Q = 4E-19;
    eps_dot_0 = 5E25;
    eta_0 = 5E6;
    C1 = 1.4;
    C2 = 17.3;

    T_Tg = T / Tg;

    sigma_plastic = k_b * T_Tg * Tg_0 / v * ...
                asinh(eps_dot / eps_dot_0 * exp(Q / (k_b * T_Tg * Tg_0)))
                    ;

    sigma_viscous = 3 * eps_dot * eta_0 * ...
        exp((-log(10) * C1 * (T_Tg - 1) / (C2 / Tg_0 + T_Tg - 1)));

    if T_Tg < 1
        stress = sigma_plastic;
        mechanism = 1;
    elseif sigma_plastic <= sigma_viscous
        stress = sigma_plastic;
        mechanism = 1;
```

```
    else
        stress = sigma_viscous;
        mechanism = 2;
    end
end
```

Listing 6 Plastic and viscous stress calculation

7. Exponential Temperature Profile

```
function temp = temp_function_exp(time, temp_low, temp_up, tau)
    temp = temp_low + (temp_up - temp_low) * (1 - exp(-time / tau));
end
```

Listing 7 Temperature as exponential function of time

8. Glass Transition Temperature Function

```
function tg = tg_function(Tg_0, c, rho_L)
    R = 8.31;
    z = 12;
    M_p = 592e-3;
    M_d = 44.01e-3;
    delta_Cp = 175;

    c_weight = c * M_d / rho_L;
    theta = M_p * c_weight / (z * M_d * (1 - c_weight));
    beta = z * R / (M_p * delta_Cp);

    tg = Tg_0 * exp(beta * ((1 - theta) * log(1 - theta) + theta * log(
        theta)));
end
```

Listing 8 Glass transition temperature from Chow model

9. Porosity Plot Function

```
function porosity_vs_time(x, b_0, a_0, time, temp_up)
    % Ensure x has at least one column
    if size(x, 2) < 1
        error('Input x must have at least one column.');
    end

    % Create figure with white background
    figure(7)
    set(gcf,'Color','w') % White background
    hold on
```

```
    % Predefined legend labels (forcefully set)
    legend_labels = {'Tf = 175', 'Tf = 185', 'Tf = 195', 'Tf = 205'};

    % Plot each temperature curve
    for i = 1:size(x, 2)
        % Calculate porosity
        a_vec = x(:, i);
        b_vec = (a_vec.^3 + b_0^3 - a_0^3).^(1/3);
        f_vec = a_vec.^3 ./ b_vec.^3;

        % Plot with distinct color and forced legend
        plot(time, f_vec, 'LineWidth', 1.5)
    end

    % Format plot
    xlabel('Time (s)')
    ylabel('Porosity')
    title('Porosity vs Time')
    grid off
    xlim([0 10])
    ylim([0 1])

    % Add forced legend labels
    legend(legend_labels, 'Location', 'northeast', 'NumColumns', 1)

    hold off
end
```

Listing 9 Porosity vs. time plot

E. Ree-Eyring Fitting Code

```
% Given properties
k_b = 1.38E-23;
v = 7.5E-27;
T_g = 217;
q = 4E-19;
eps_dot_0 = 5E25;
eps_e_dot = 0.00625;

% Data points
T_Tg = [0.80645, 0.8525, 0.8986, 0.9447];
sigma_e_data = [38.285e6, 33.607e6, 29.15e6, 21.284e6];

% Convert T/Tg to absolute temperature
T_data = T_Tg * T_g;
```

```
% Define the Ree-Eyring model function
model_fun = @(sigma, T) asinh((eps_e_dot / eps_dot_0) * exp(q ./ (k_b * T)
    )) .* k_b .* T ./ v;

% Define the objective (error) function to minimize
error_fun = @(sigma) sum((model_fun(sigma, T_data) - sigma_e_data).^2);

% Initial guess for sigma
initial_sigma = 40e6;

% Perform nonlinear optimization
fitted_sigma = fminsearch(error_fun, initial_sigma);

% Evaluate the model at fitted parameters
sigma_fitted = model_fun(fitted_sigma, T_data);

% Plotting the data and fitted curve
figure;
scatter(T_data, sigma_e_data, 75, 'k', 'filled'); % Data points
hold on;
plot(T_data, sigma_fitted, 'k', 'LineWidth', 2.5); % Model curve
xlabel('Temperature (T)', 'FontSize', 14);
ylabel('Stress (\sigma_e) [Pa]', 'FontSize', 14);
legend('Data Points', 'Fitted Model', 'Location', 'best');
grid off;

% Display the fitted result
disp(['Fitted sigma value: ', num2str(fitted_sigma), ' Pa']);
```

Listing 10 Fitting stress model using Ree-Eyring relation and fminsearch

F. Parametric Study under 1 MPa Cases

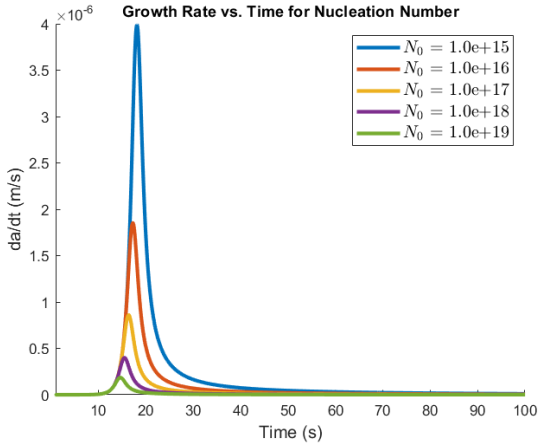

(a) Growth Rate vs Time

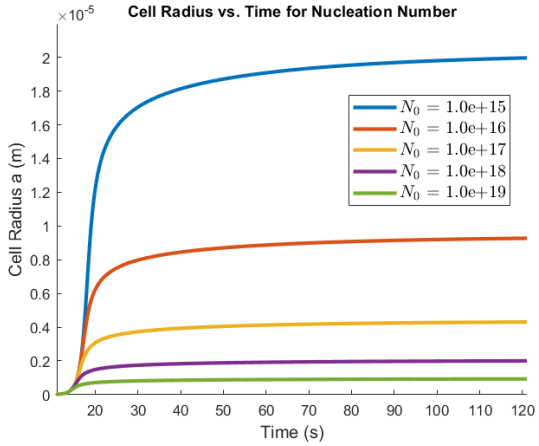

(b) Cell Radius vs Time

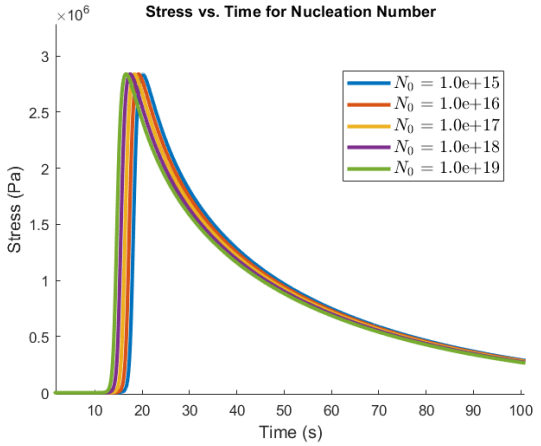

(c) Stress vs Time

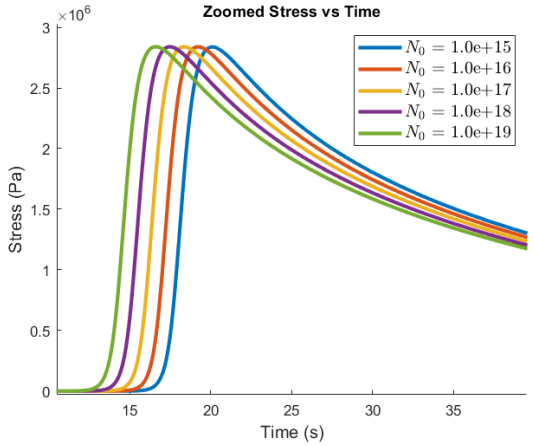

(d) Zoomed Stress vs Time

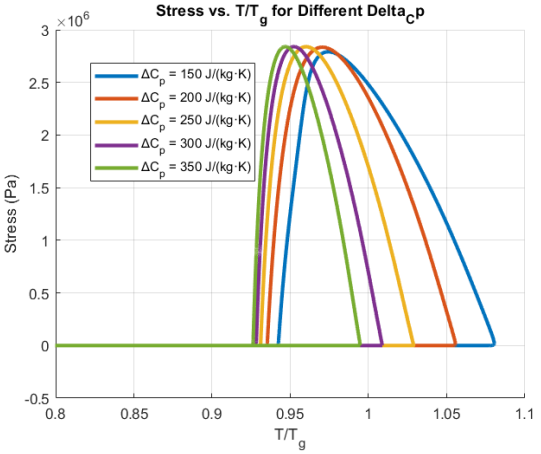

(e) Stress vs T/Tg

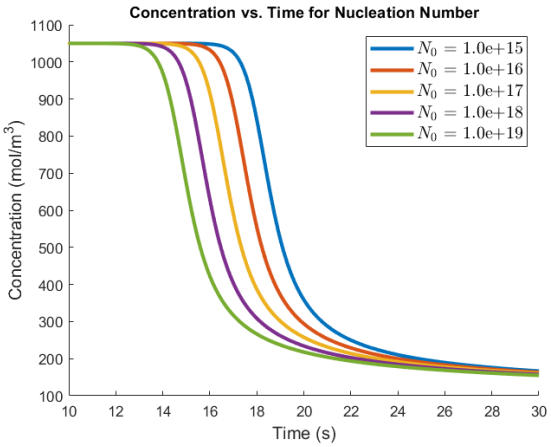

(f) Concentration vs Time

Fig. 62 Effect of Nucleation Number on the Model under 175C and 1MPa

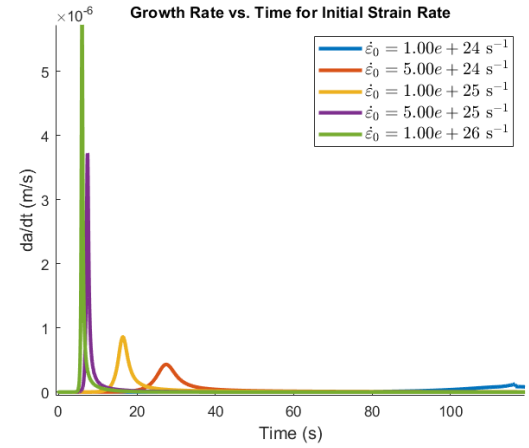

(a) Growth Rate vs Time

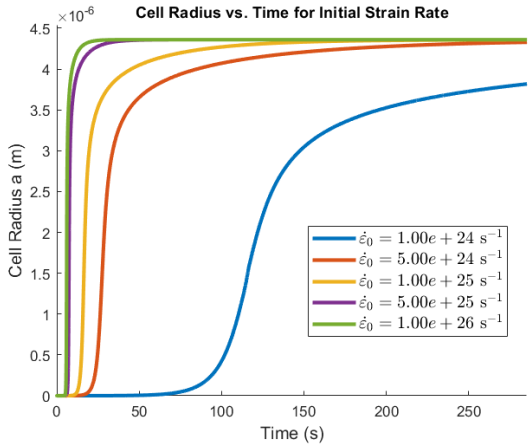

(b) Cell Radius vs Time

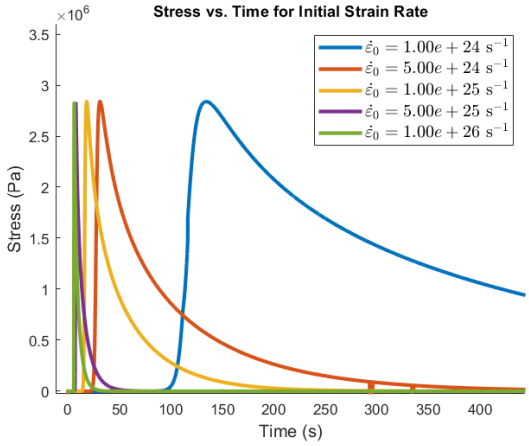

(c) Stress vs Time

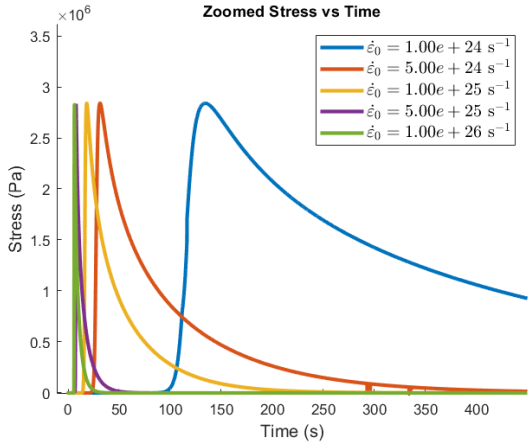

(d) Zoomed Stress vs Time

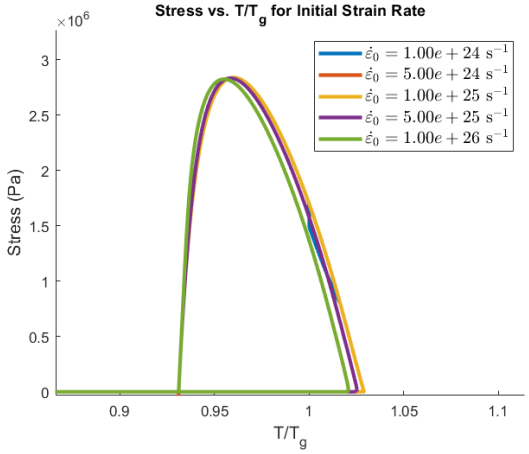

(e) Stress vs T/Tg

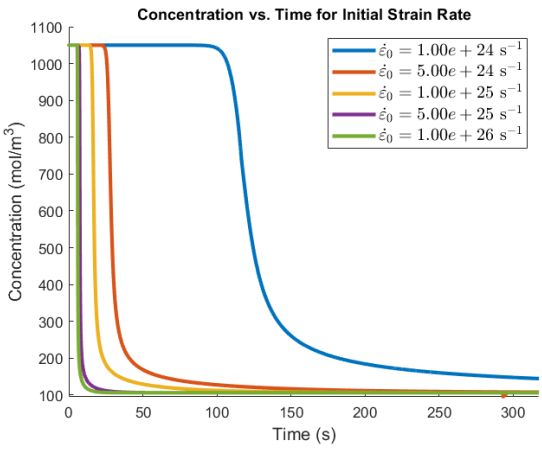

(f) Concentration vs Time

Fig. 63 Effect of Initial Strain Rate on the Model under 175C and 1MPa

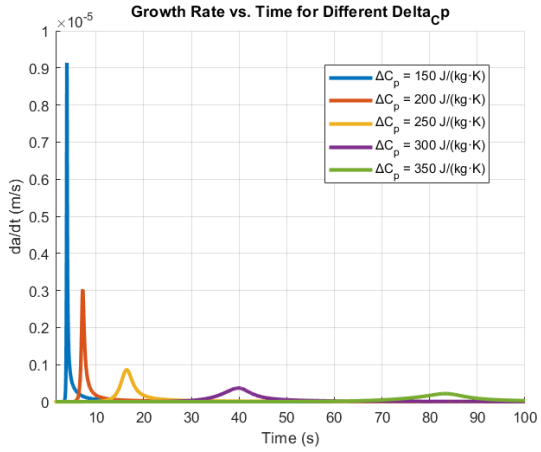

(a) Growth Rate vs Time

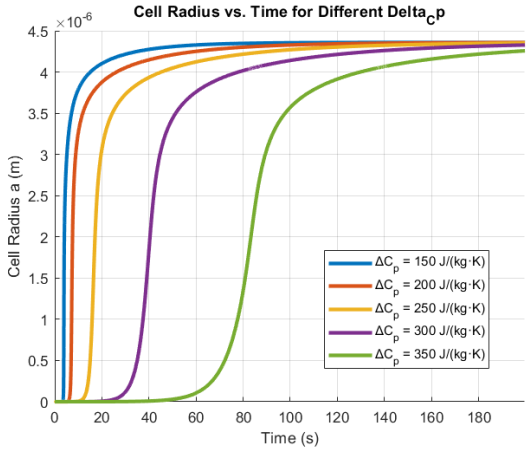

(b) Cell Radius vs Time

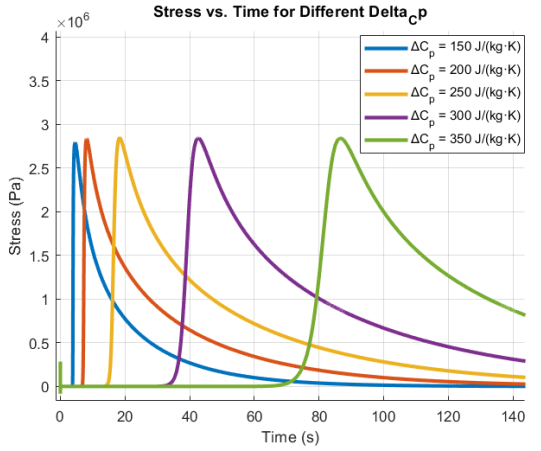

(c) Stress vs Time

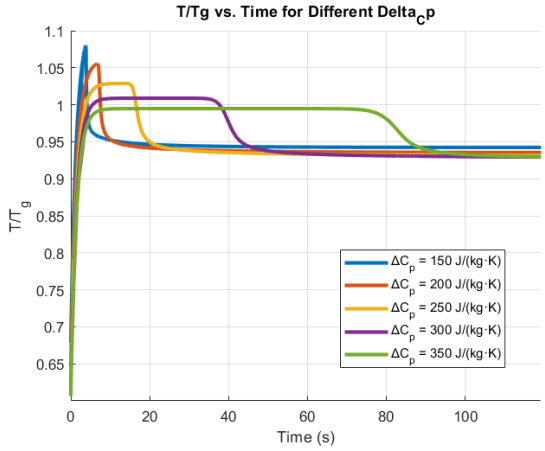

(d) T/Tg vs Time

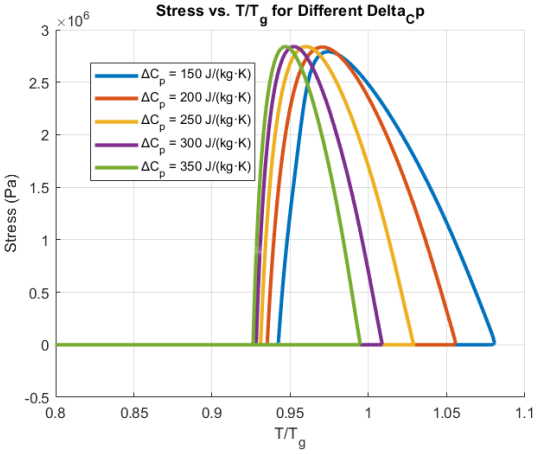

(e) Stress vs T/Tg

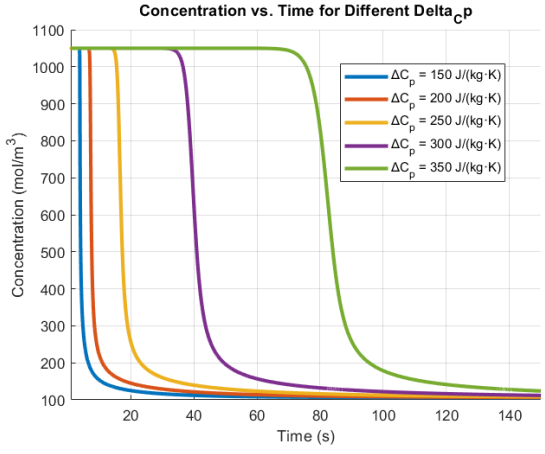

(f) Concentration vs Time

Fig. 64 Effect of Change of Specific Heat on the Model under 175C and 1MPa

IX. Acknowledgments

It has been an incredible journey and what an experience. Starting from polishing samples to staring at SEM images, to fitting the model with measured results, if I were me a few years ago, I wouldn't believe I could make this into reality. Yet here I am, at the end of the project, I wouldn't trade the experience for anything.

First, I would like to express my most sincere gratitude to my advisor, Prof. Marco Salviato, whose guidance, courses and support have been the key throughout my research journey on polymer modeling. Your expertise in FEA, solid mechanics and fracture mechanics has been the pivotal elements in shaping my understanding and approach in the thesis. Also, the insight you have to the industry and high standards you gave to me have benefited me greatly as both research and engineer, which deeply rooted in my future career development.

I am sincerely thankful to all the members of Multiscale Analysis of Materials and Structures (MAMS) Lab, for creating a helpful and friendly atmosphere in research. Whether we are arguing about mathematical method to be used, complaining about failures in DMA, sharing MATLAB bugs, or just enjoying the meeting and bowling, I'm grateful for the encouraging and collaborative environment. I extend my special thanks to Kush Dwivedi, whose insightful feedback in polymer growth model and testing aspect when working on cell growth model, especially during the development of the equations and computational model, significantly improved my working quality and efficiency. Even when I made some dumb mistakes like messing up with units, your patience never fades.

My heartfelt appreciation also goes to the colleagues in the machine shop and testing lab - Sean Krewson and Bill Kuykendall - for the hours spent in sample preparation and instruction on DMA testing. Your professional experience made the testing go smoothly and kept me on the right track by strictly following the standards and procedures. I am particular thankful for the support the support from Santhosh Sridhar on SEM imaging and post-processing of the nanoscale data, which plays a critical role in the validation of constitutive model.

On the personal side, I would like to express my deepest appreciation to my family for their long lasting encouragement and belief. You probably had no idea what I was talking about (like how can stretching a piece of plastic so difficult?) But you listened, nodded and you patience in me has been the reliable source of motivation during testing failures and exhaustion. Your willingness to hear and belief powered me forward.

I am honored to have this opportunity to work with UW Department of Aeronautics & Astronautics and many incredible people helping me on this two year journey. Thank you again. This work is as much as your as it is mine.